UNIVERSITY OF OKLAHOMA

GRADUATE COLLEGE

MODELING MULTICOMPONENT GAS FLOW IN LIQUIDS RICH SHALES

A THESIS

SUBMITTED TO THE GRADUATE FACULTY

in partial fulfillment of the requirements for the

Degree of

MASTER OF SCIENCE

By

JIHYUK KIM
Norman, Oklahoma
2016

MODELING MULTICOMPONENT GAS FLOW IN LIQUIDS RICH SHALES

A THESIS APPROVED FOR THE
MEWBOURNE SCHOOL OF PETROLEUM AND GEOLOGICAL ENGINEERING

BY

_____
Dr. Deepak Devegowda, Chair

_____
Dr. Chandra S.Rai

_____
Dr. Siddharth Misra

Dedication

To my parents,

My wife, Lanyi,

My daughter, Minjung,

And my son, Rowan

Acknowledgements

I would like to give my sincere gratitude to Dr. Deepak Devegowda, my advisor. Especially for his high passion, insightful advises and warm encouragements throughout the course of this thesis. It has been such a great experience working with him. I could learn a lot from him not only for the thesis but also how to give trust to others.

I also like to thank my committee members, Dr. Chandra S.Rai, and Dr. Siddharth Misra for valuable comments and encourages.

Table of Contents

List of Tables

List of Figures

Abstract

Production data acquired from liquids-rich shale reservoirs show a few very interesting trends:

1. A relatively constant gas-oil ratio (GOR) or condensate-gas ratio (CGR) although flowing bottomhole pressures may be below the fluid saturation pressures.
2. Produced fluid compositions are generally different from in-situ fluid compositions even though the GOR/CGR may be constant.

These observations are unique to liquids-rich shale wells and are not seen in conventional reservoirs. In this work, I investigate a few theories that explain these phenomena, develop the corresponding mathematical formulations and employ these in a numerical reservoir simulator to demonstrate their impact on flowing fluid compositions and GOR/CGR trends. My work in this thesis is centered around investigating the role of multicomponent Knudsen diffusion and multicomponent adsorption as well as Fick's diffusion, surface diffusion and molecular diffusion effects.

With these transport mechanisms, I show that a constant CGR/GOR trend may be achieved with varying produced fluid compositions by allowing more rapid transport of lighter hydrocarbon components compared to those of a higher carbon number. I demonstrate this effect with a synthetic case study as well as with a field-scale case study.

Although this work is the first such effort to quantify multicomponent flows in liquids-rich shales, the discussion in this thesis does not include experimental verification of the results. To that end, I also provide a few recommendations for experimental work to be performed to confirm the observations provided in this thesis.

Chapter 1. Introduction

Exploration and development activity in unconventional shale reservoirs has rapidly grown in the past two decades since the commercial success of the Barnett shale in the early 2000s. The driving force behind this success and the accompanying growth can be attributed to technology advances such as multistage hydraulic fracturing and horizontal well drilling, both of which provide greater access to large reservoir volumes economically.

Figure 1 shows the gas production from various shale plays from 2000 until February 2016 as provided by the U.S. Energy Information Administration (EIA, 2016) showing a 20-fold increase in gas production over the last decade and a half. The initial growth was largely due to activity in the Barnett followed by more recent increases from the Haynesville and the Marcellus play.

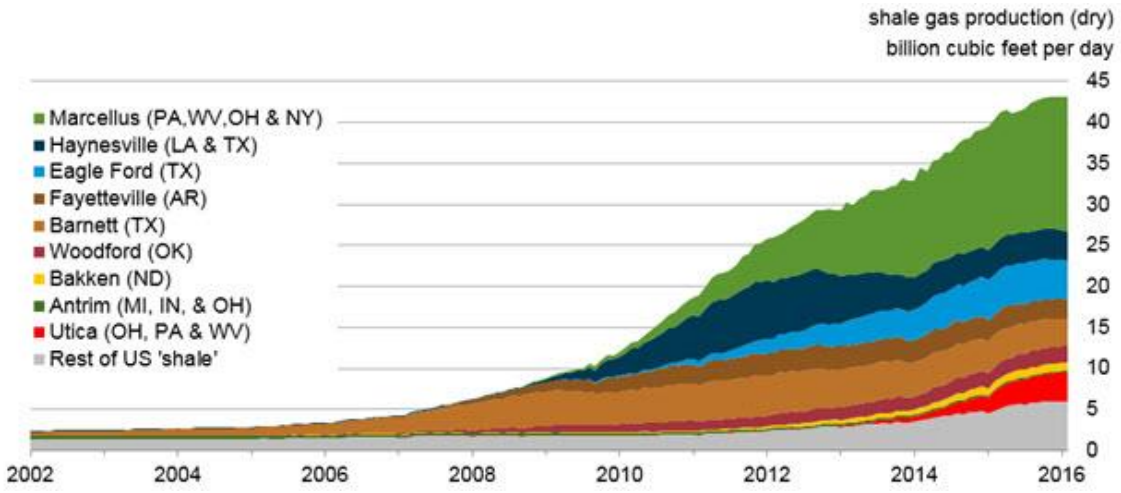

Figure 1. U.S. dry shale gas production until Feb. 2016, (EIA, 2016)

Figure 2 is the corresponding plot for tight oil production that has seen a 12-fold increase from 2000 to 2016.

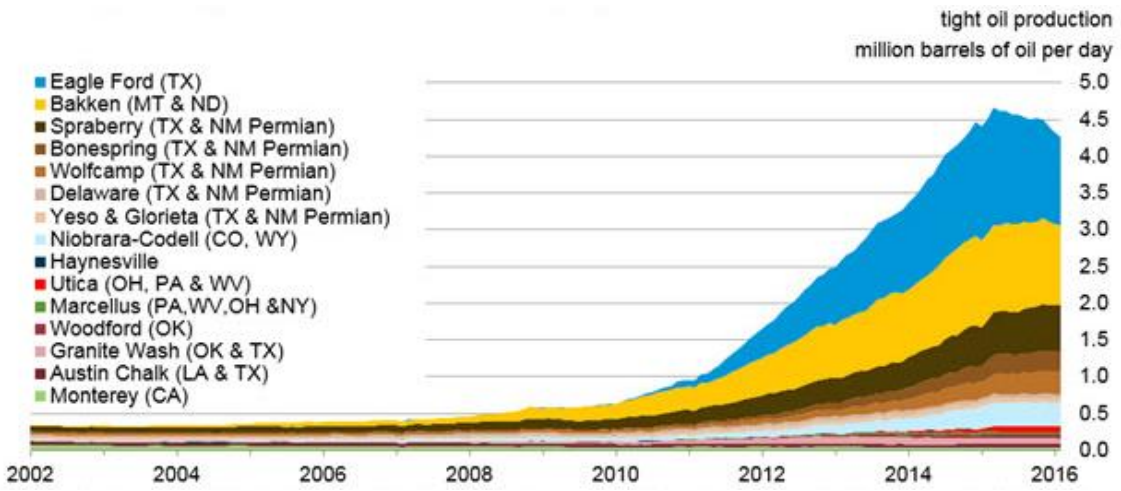

Figure 2. U.S. tight oil production until Feb. 2016, (EIA, 2016)

EIA (2016) also provides projections for dry natural gas and tight oil production by source in United State until 2040 as shown below in Figure 3 and Figure 4. The significance of these tight reservoirs for domestic energy security therefore cannot be minimized.

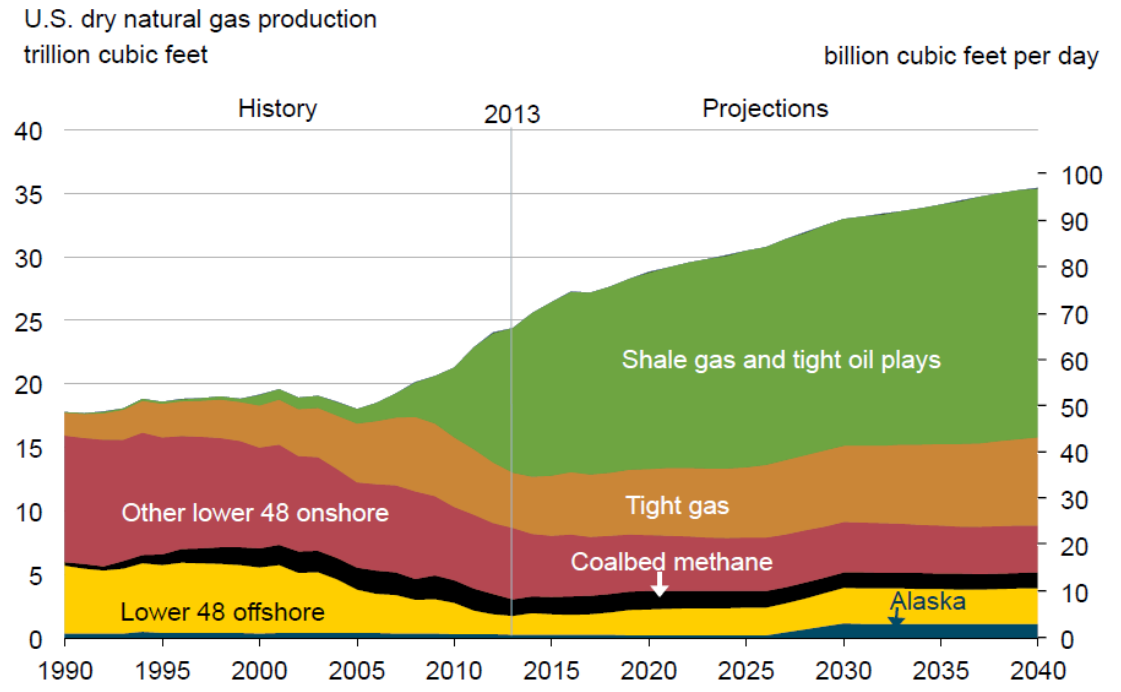

Figure 3. U.S. dry natural gas production (EIA, 2014)

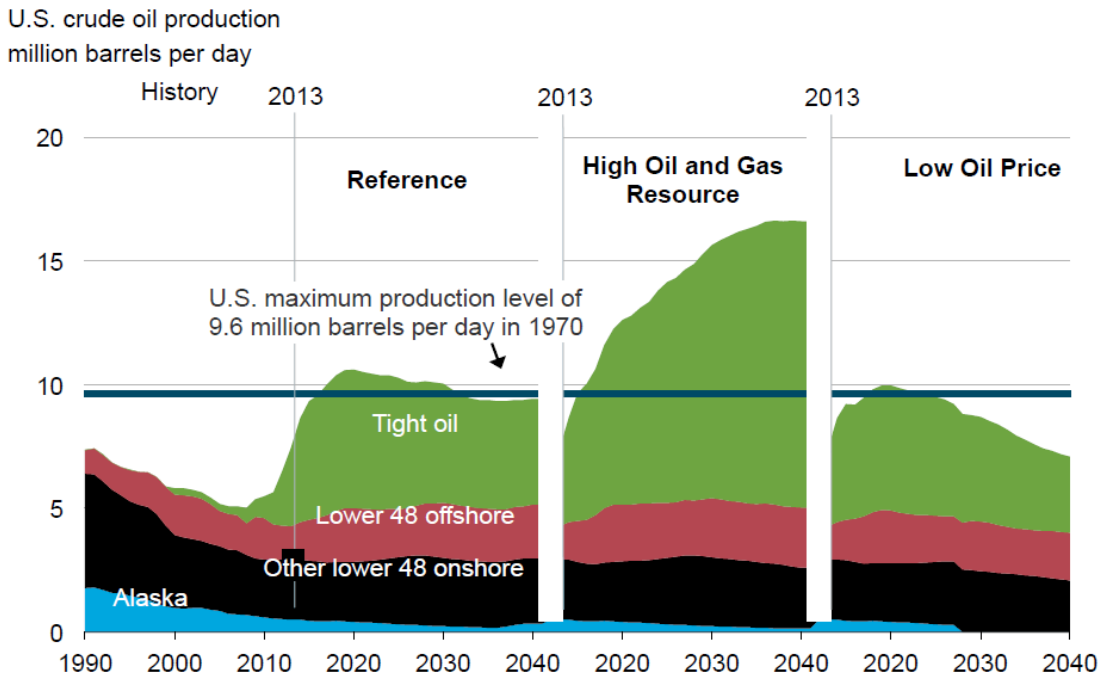

Figure 4. U.S. crude oil production (EIA, 2015)

1.1. Production Trends in Liquids-Rich Shales

Curtis et al. (2010) were among the first to discuss the microstructural features that are unique to shales. Specifically, at the micro-scale, shales can be characterized by the presence of an inorganic matrix with organic matter embedded within. Additionally, there may be micropores within both the organics and the inorganic matrix as well as natural microcracks.

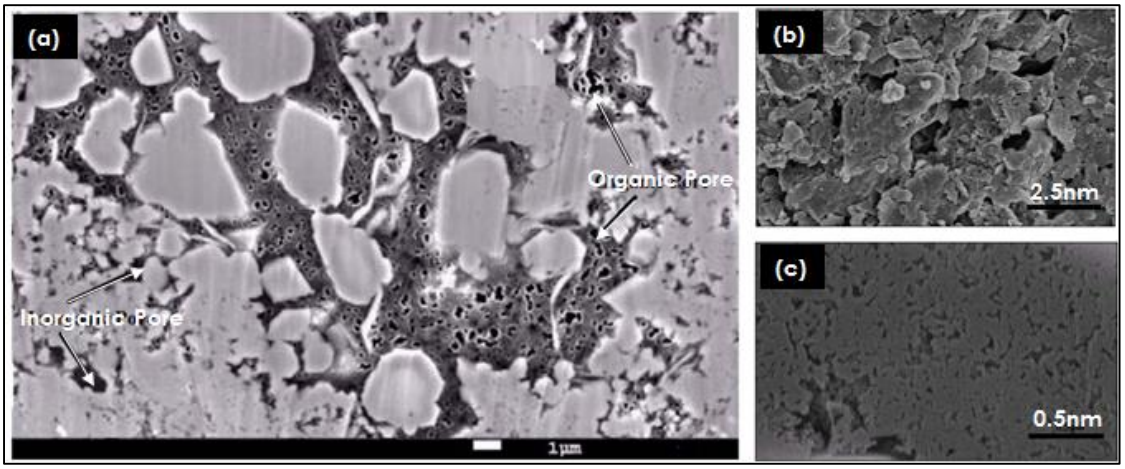

Figure 5. SEM image of a selected gas shale sample.
(a) SEM image of organic and inorganic pores (Passey et al., 2010).
(b) Inorganic pore SEM image, (c) Organic pore SEM image (Wang, 2014)

Hydrocarbon storage within the shale may be classified (Gupta et al., 2015) as:

1. Free hydrocarbon within the organics or inorganic pore and fracture systems.
2. Absorbed hydrocarbon on the surface of the organic pores.

The initial production rate is dominated by free hydrocarbon followed by a significant rate decline and an accompanying pressure drop in the matrix and fracture systems. As the pressure drops, increasing amounts of the adsorbed hydrocarbon becomes available for transport and production may be sustained for extended periods following the initial decline.

There are however several interesting observations that are unique to liquids-rich shales. A common observation is extended periods of constant production gas-oil ratios (GOR) in spite of wells operating at pressures below the fluid saturation pressure. The stable

GOR production usually occurs following very early production as shown in Figure 6 and may last several months to years with minor changes (Khoshghadam et al., 2015).

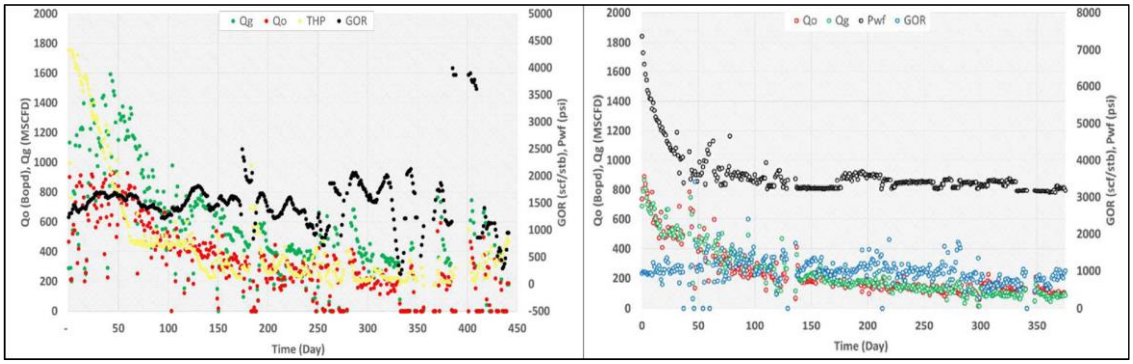

Figure 6. Constant GOR production in liquids-rich shale reservoirs.
Typical two wells of Eagle Ford Shale (Khoshghadam et al., 2015)
(THP : Top Head Pressure, Pwf : Bottomhole flowing pressure)

Another unique production trend in the shales is discussed by Schettler and Parmely (1989) and Freeman et al. (2012) as shown in Figure 7 that shows compositional variations in the produced fluid over time obtained from field data.

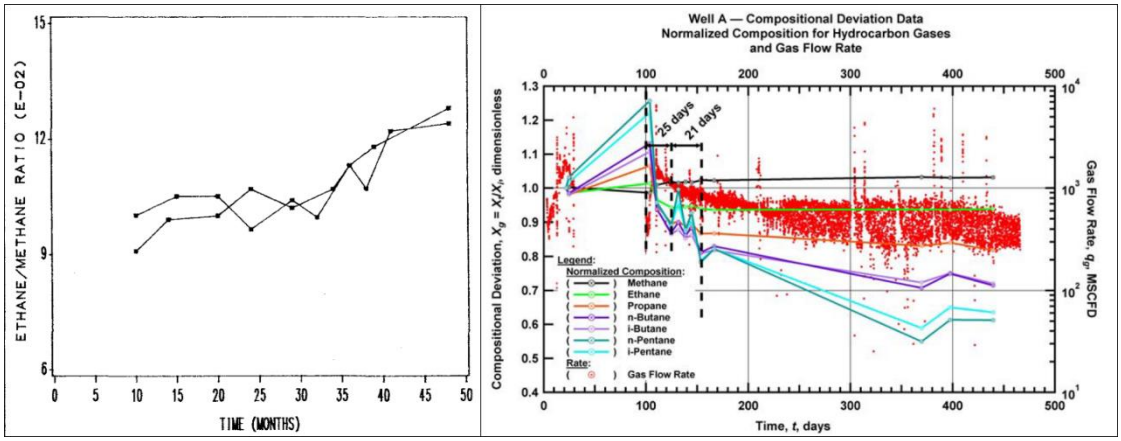

Figure 7. Produced fluid composition changes in shales. The figure on the left shows ethane to methane ratio from different two wells (Schettler and Parmely, 1989) and the figure on the right shows the composition changes with time (Freeman et al. 2012)

Schettler and Parmely (1989) examined 30 sandstone wells and 200 gas samples with a 10- to 48-month production period and they conclude that the changes in gas composition can be attributed to adsorption in clay particles and Knudsen diffusion through small pores. Freeman et al. (2012) also report analogous trends in produced fluid compositions and utilize a numerical model with gas diffusion and adsorption to explain field observations.

These two unique production trends will be investigated in this thesis by analyzing multicomponent fluid flow in nanopores. The thesis is organized as follows:

1. Chapter 2 provides an overview of the known physical phenomena governing single- and multicomponent gas flows in nanoporous media, including slip flow, diffusion and adsorption.
2. Chapter 3 is a discussion of a 1-D reservoir simulation model developed in-house that incorporates the physics of multicomponent gas flow discussed in Chapter 2.
3. Chapter 4 utilizes a commercially available reservoir simulator to model these same physical phenomena on a larger, reservoir-scale model. Commercial simulators do not account for these phenomena; therefore I make a few reasonable assumptions regarding diffusion.
4. Chapter 5 is a sensitivity study that explores the impact of various reservoir and completion-related variables on production trends.
5. Chapter 6 provides the conclusions of this study and recommendations for future work.

Chapter 2. Overview of Transport in Shales

Following the discussion of some of the production trends observed in liquids-rich shale wells in both the condensate and volatile oil window, in this chapter 1 provide an overview of recent developments in describing transport in shales for both single-component and multi-component gases and liquids. This chapter will lead to the development of the case studies presented in Chapters 3 and 4.

2.1. Flow Regimes in Shales

Shales are characterized by a range of pore and pore throat sizes (Curtis et al., 2010). Darcy's law which describes flow in the viscous regime therefore may not be appropriate in nanopores where slip flow effects become important. The governing factors controlling flow at these scales are the pore pressure, pore sizes as well as the fluid compositions. In order to develop a model for flow at these scales, it is important to characterize the different flow regimes possible as a function of these variations.

2.1.1. Flow Regimes Categorization

For shales characterized by pores on the order of a few nanometers to several hundred nanometers where gas transport may be governed by slip flow effects and convective flow, Javadpour et al. (2007) provided a general guide to identifying the predominant flow regime based on the Knudsen number as shown below in Table 1. The Knudsen number is defined in the next section.

Table 1. Flow regimes distinguished by Javadpour et al. (2007)

Knudsen number, Kn	Flow regime
Kn < 0.001	Darcy flow (Continuum flow)
0.001<Kn<0.1	Knudsen diffusion (Slip flow)

Freeman (2010) also categorized flow in 3 different regimes as convection flow, Knudsen diffusion dominated flow and molecular diffusion. Later, Civan. (2010) and Swami et al. (2012) identified 4 different flow regimes based on the Knudsen number as shown below in Table 2.

Table 2. Flow regimes from Swami et al. (2012)

Knudsen number, Kn		Flow regime
Kn < 0.001		Viscous flow
0.001 < Kn < 10	0.001 < Kn < 0.1	Slip flow
	0.1 < Kn < 10	Transition flow
Kn > 10		Knudsen flow

Figure 8 shows the flow regimes identified by Shi et al. (2013) based on the Knudsen number as well as the corresponding flow equations appropriate for each regime.

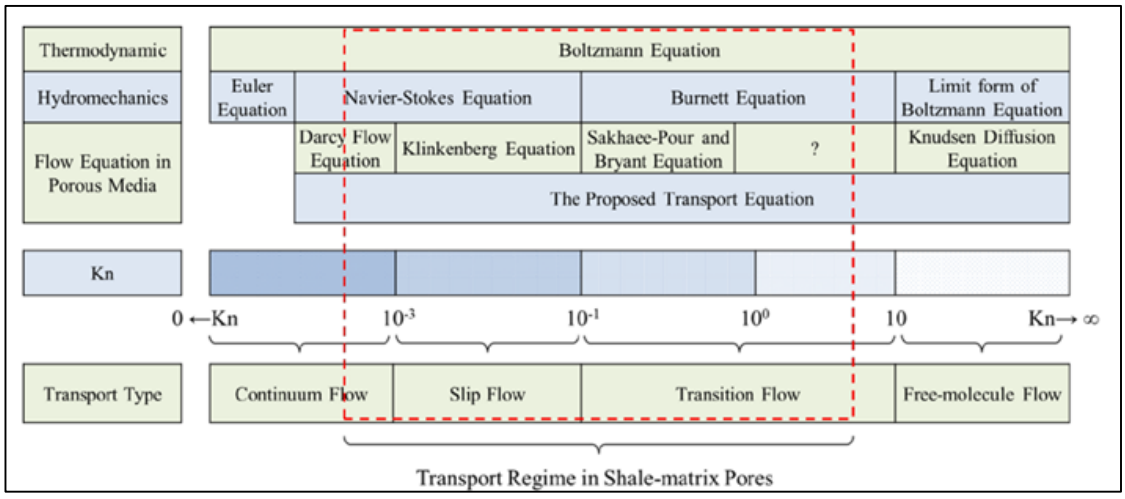

Figure 8. Flow regime chart based on Knudsen number (Shi et al., 2013)

Although there are slight differences in the classification of flow regimes, in general Darcy flow is more appropriate for low Knudsen number flows while slip flow becomes dominant at higher Knudsen numbers. In the following section, I provide an overview of the Knudsen number that represents molecular activity in a specific pore system. In order to understand the Knudsen number, I first discuss the mean free path for gases.

2.1.2. Mean Free Path

The free path of a gas molecule is the distance that the molecule travels before a collision with other molecules. Because the gas molecules move randomly, the average value of the free path called as the mean free path is defined at a specified pressure and temperature conditions. Figure 9 shows a simple conceptual diagram of the free path for a gas molecule.

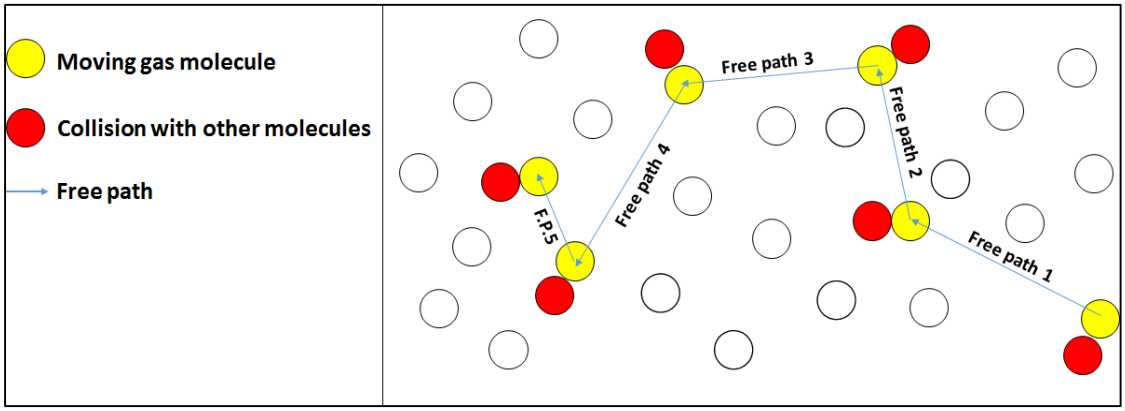

Figure 9. Conceptual illustration of the free path of a gas molecule.

To calculate the mean free path, the first step is to define the average relative velocity. From Reif (2009), the movement of the gas molecules are assumed to be random and for 2 randomly selected gas molecules, their velocities may be represented by the vectors, $\overrightarrow{V_1}$ and $\overrightarrow{V_2}$.

The relative velocity V_{rel} is defined as:

$$\overrightarrow{V_{rel}} = \overrightarrow{V_1} - \overrightarrow{V_2} \tag{1}$$

$$|V_{rel}| = \sqrt{\overrightarrow{V_{rel}} \cdot \overrightarrow{V_{rel}}} = \sqrt{(\overrightarrow{V_1} - \overrightarrow{V_2}) \cdot (\overrightarrow{V_1} - \overrightarrow{V_2})} \tag{2}$$

$$|V_{rel}| = \sqrt{(\overrightarrow{V_1} \cdot \overrightarrow{V_1}) - 2(\overrightarrow{V_1} \cdot \overrightarrow{V_2}) + (\overrightarrow{V_2} \cdot \overrightarrow{V_2})}$$

The magnitude of the average relative velocity is:

$$|\overline{V_{rel}}| = \sqrt{\overline{(\overrightarrow{V_1} \cdot \overrightarrow{V_1})} - 2\overline{(\overrightarrow{V_1} \cdot \overrightarrow{V_2})} + \overline{(\overrightarrow{V_2} \cdot \overrightarrow{V_2})}}$$

$$|\overline{V_{rel}}| = \sqrt{\left(\overrightarrow{\overline{V_1}^2}\right) + \left(\overrightarrow{\overline{V_2}^2}\right)} \tag{3}$$

Because of the random nature of motion of the gas molecules, $\overrightarrow{V_1} \cdot \overrightarrow{V_2} = 0$

If $\overrightarrow{V_1}$ and $\overrightarrow{V_2}$ possess the same magnitude, the average relative velocity can be defined as:

$$\overline{V_{rel}} = \sqrt{2}\overline{V} \tag{4}$$

Figure 10 is the conceptual scheme of the effective collision area by Carl (1998) which is calculated based on the diameter of the gas molecules.

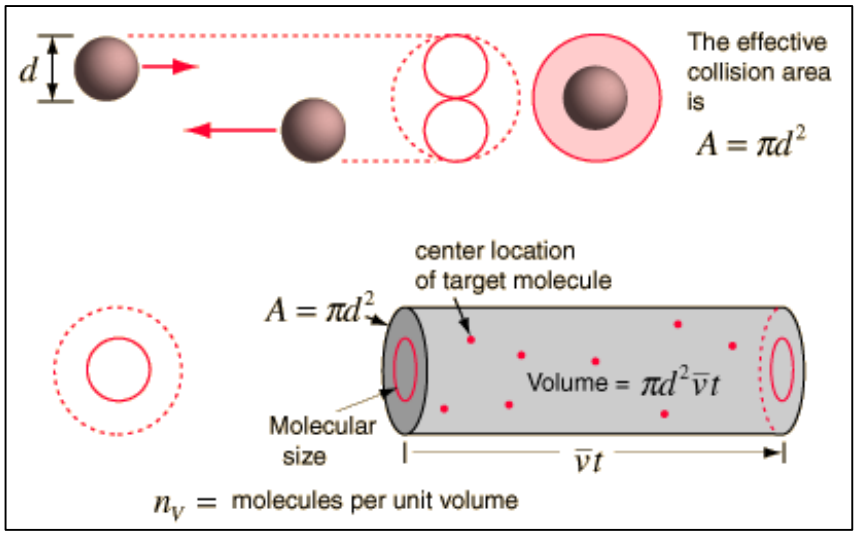

Figure 10. Effective collision area (Carl, 1998)

Equation 5 defines the mean free path with a fixed number of target molecules.

$$\lambda = \frac{\text{Travel distance}}{\text{Total vol. of interaction} \times \text{Number of molecules per unit vol.}} = \frac{\bar{V}t}{\pi d^2 \bar{V}t \times n_v} \tag{5}$$

An additional correction for the volume of interaction is needed to account for the relative velocities of the different molecules. Therefore,

$$\lambda = \frac{\bar{V}t}{\pi d^2 \sqrt{2}\bar{V}t \times n_v} = \frac{1}{\pi d^2 \sqrt{2} n_v} \tag{6}$$

Number of molecules per unit volume for an ideal gas can determined using Avogadro constant N_A,

$$n_v = \frac{nN_A}{V} = \frac{N_A P}{RT} = \frac{P}{k_B T} \tag{7}$$

Finally the mean free path can be calculated using Equation 8.

$$\lambda = \frac{k_B T}{\sqrt{2} P \pi d_g^2} \tag{8}$$

Where P：Gas pressure, [Pa]

d_g: Effective diameter of a gas molecule, [m]

k_B: Boltzmann constant, [1.3807×10^{-23} J/K]

T：Temperature of the gas, [K]

R: Gas constant, [8.314472 $J/(K \cdot mol)$] = $N_A \times k_B$

N_A: Avogadro number, [$6.02214129 \times 10^{23} mol^{-1}$]

Equation 8 is valid for ideal single-component gases where the motion of the molecules is random and for no interactions between the different molecules. For a

multicomponent gas mixture, Freeman (2010) proposed Equation 9 as the mean free path of component 1.

$$\bar{\lambda_1} = \frac{\overline{V}_1}{\sum_{i=1}^{n} \pi d_1 d_i \sqrt{\overline{V_1}^2 + \overline{V_i}^2} \left(\frac{N_A P_i}{RT}\right)} \tag{9}$$

Where, P_i: Partial Pressure of component i, [Pa]

R: Gas constant, $[8.314472 \ \ J/(K \cdot mol)] = N_A \times k_B$

N_A: Avogadro number, $[6.02214129 \times 10^{23} mol^{-1}]$

d_i: Lennard $-$ Jones Potential Parameter, [m]

$\overline{V_i}$: Average velocity of a single component $'i'$ in gas mixture, [m/s]

Mean molecular velocity, $\overline{V} = \sqrt{\frac{8RT}{\pi M}}$, [m/s]

T : Temperature, [K]

Derivation of the Equation 9 starts from the average mean free path definition as given Equation 5. From the definition of average mean free path, travel distance of 'component 1' equals $\overline{V}_1 t$ and the interaction volume is sum of the interaction volumes between 'component 1' and each of the other molecules. Therefore, from average relative velocity shown in Equation 3, total interaction volume with respect to component 1 can be defined shown in Equation 10 for a gas mixture with 'n' components.

$$\text{Interaction Vol}_{1,i=1} = \pi d_1 d_{n=1} \cdot \overline{V}_{rel,1,i=1} \cdot t$$

$$\text{where, } \overline{V}_{rel,1,i=1} = \sqrt{\vec{V}_1^{\,2} + \vec{V}_1^{\,2}}$$

$$\text{Interaction Vol}_{1,i=2} = \pi d_1 d_{i=2} \cdot \overline{V}_{rel,1,i=2} \cdot t$$

$$\text{where, } \overline{V}_{rel,1,i=2} = \sqrt{\vec{V}_1^{\,2} + \vec{V}_2^{\,2}}$$

$$\vdots$$

$$\text{Interaction Vol}_{1,i=n} = \pi d_1 d_{i=n} \cdot \overline{V}_{rel,1,i=n} \cdot t$$

$$\text{where, } \overline{V}_{rel,1,i=n} = \sqrt{\vec{V}_1^{\,2} + \vec{V}_n^{\,2}}$$

Therefore, total interaction volume with respect to component 1 can be defined as:

$$\sum_{i=1}^{n} \text{Interaction Vol}_{1,i} = \sum_{i=1}^{n} \left(\pi d_1 d_i \cdot t \cdot \sqrt{\vec{V}_1^{\,2} + \vec{V}_i^{\,2}} \right) \tag{10}$$

Using the total interaction volume defined in Equation 10 gives:

$$\overline{\lambda_1} = \frac{\overline{V}_1 t}{\sum_{i=1}^{n} \left(\pi d_1 d_i t \sqrt{\overline{V_1}^2 + \overline{V_i}^2} \right) n_v} \tag{11}$$

Also applying the Equation 7 to Equation 11 gives:

$$\overline{\lambda_1} = \frac{\overline{V}_1}{\sum_{i=1}^{n} \pi d_1 d_i \sqrt{\overline{V_1}^2 + \overline{V_i}^2} \left(\frac{N_A P_i}{RT} \right)} \tag{12}$$

2.1.3. Knudsen Number

The Knudsen number, *Kn* introduced by Knudsen (1934) is defined as the ratio of mean free path to the pore diameter.

$$Kn = \frac{\lambda}{d_p} \tag{13}$$

In Equation 13, d_p is the pore diameter and λ is the mean free path of the gas. In a capillary tube, the diameter is well known. However in porous media, this number is not known and the Knudsen number is defined as the ratio of the mean free path to the hydraulic radius, R_h. The hydraulic radius, R_h is the ratio of the cross-sectional area to

the perimeter of a pipe. For the cylindrical tube, pore diameter equals to $2R_h$. Additionally in organic pores where adsorption may be significant, the actual cross-sectional area available to flow may be reduced. Figure 11 demonstrates the reduction in pore diameter because of single-layer and multi-layer adsorption (Wang et al. 2015). This can have an impact on the Knudsen number. In this thesis, I do not consider this effect for a few reasons. Our knowledge of adsorption in organic pores continues to be limited. There is evidence to suggest multilayer adsorption for single-component fluids (Didar and Akkutlu, 2013). However the extension to multi-component fluids is lacking because of challenges in describing competitive adsorption between different species.

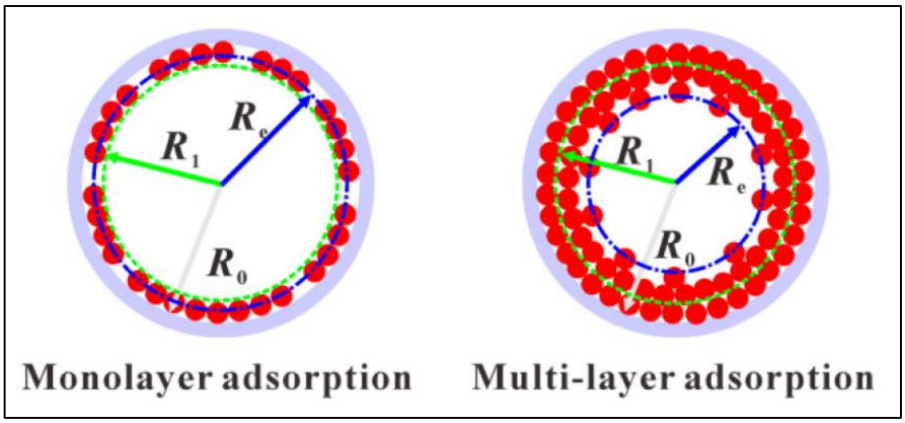

Figure 11. Monolayer and multi-layer adsorption (Wang et al., 2015).

2.2. Models for Gas Flow in Shales

2.2.1. Klinkenberg or Slippage Effect

The Darcy equation for viscous flow may be derived from the Navier-Stokes equation when no slip conditions exist. This is largely the case for flow through larger capillary tubes or pore diameters and pore throat diameters common to conventional rocks. For smaller pores on the order of nanometers, the Navier-Stokes equation is valid in the center of the pore but not in the vicinity of the pore wall as shown in Figure 12. With an increase in the Knudsen number as we move to smaller diameter pores, there are more frequent interactions between the gas molecules and the pore wall surface. The area influenced by these interaction is called the Knudsen layer that can be described by the Boltzmann equation but not the Navier-Stokes equation (Li and Sultan, 2015). The non-zero velocity of gas molecules adjacent to the pore wall is called the slip phenomenon. Figure 12 is a conceptual illustration of the Knudsen layer.

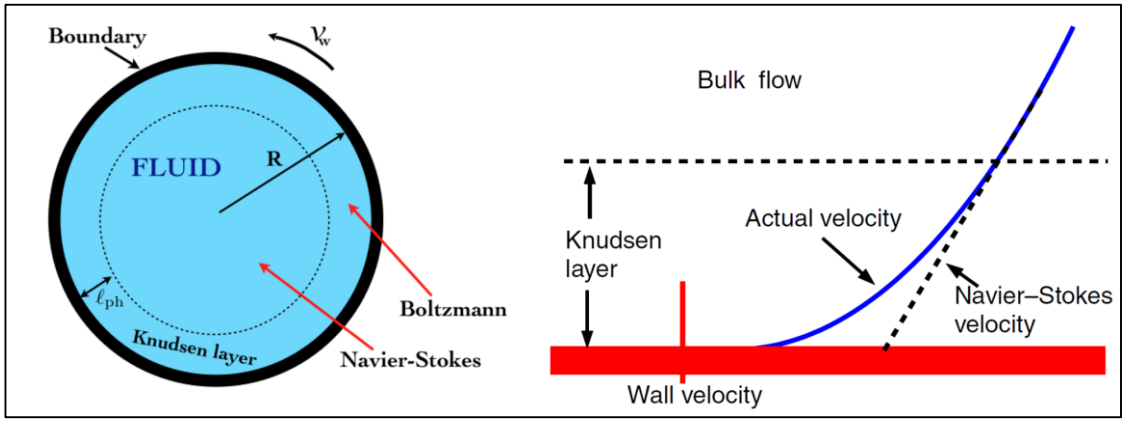

Figure 12. Knudsen layer (Mannarelli, 2013 and Guo et al., 2007)

The slippage effect or the Klinkenberg effect was reported by Muskat (1937) and Klinkenberg (1941) and they attributed deviations from Darcy's law for low pressure

gas flows to the slip flow effect. Slip flow occurs in the Knudsen layer and tends to result in an increase of the gas phase permeability for values of Knudsen number ranging between $10^{-3} < \mathrm{Kn} < 10^{-1}$.

The apparent gas permeability is defined in Equation 14, where k_∞ is the absolute gas permeability (permeability to liquids), *P* is gas phase pressure and *b* is the Klinkenberg factor which depends on the pore radius and temperature of the gas phase. (Wu and Pruess, 1998) The derivation for Equation 14 is provided in Appendix A.

$$\mathrm{K_g} = \mathrm{K_\infty}\left(1 + \frac{b}{\mathrm{P}}\right) \tag{14}$$

$$\mathrm{b} = \mathrm{b_k} = \frac{4\mathrm{C}\lambda\mathrm{P}}{\mathrm{r}} \tag{15}$$

where, $\mathrm{K_\infty}$: Absolute permeability, $[\mathrm{m}^2]$

$\mathrm{b_k}$: Klinkenberg coefficient, [Pa]

C : Constant

P : Pressure, [Pa]

r : Radius of the pore, [m]

λ : Mean Free Path, [m]

2.2.2. Recent Developments in Modeling Flow in Shales

Although there are several approaches to model slip flow in shales (Swami et al. 2012), in this thesis I adopt the approach proposed by Civan (2010) also known as the Civan 'A method'. A discussion of these methods is provided later in this section. Civan (2010) and Michel et al. (2011) document the variations in Knudsen number with pore size and pore pressure and these are shown in Figure 13.

Civan (2010) 'A method' defines the apparent permeability to model the nanoscale flow as a function of Knudsen number and a permeability correction factor, $f(Kn)$. The equations that define these quantities are provided below. A key input is the parameter α that is defined as the rarefaction coefficient that changes with the range of the Knudsen number:

$$0 < \alpha < \alpha_0$$

$$\text{with } 0 \leq \text{Kn} < \infty$$

The coefficient α is defined by Beskok and Karniadakis (1999) empirically as:

$$\alpha = \alpha_0 \frac{2}{\pi} \tan^{-1}(\alpha_1 \text{Kn}^{\alpha_2}) \tag{16}$$

When the Knudsen number is infinite, which means free molecular flow condition,

$$\alpha_1 = 4.0\ ,\ \alpha_2 = 0.4\ ,\ \alpha_0 = \frac{64}{3\pi(1-\frac{4}{\text{b}})}$$

Where b is a slip coefficient and generally defined to be -1.0 with $\alpha = 0$ for fully slip flow.

$$\alpha_0 = \frac{64}{15\pi}$$

Therefore,

$$\alpha = \frac{128}{15\pi^2}\tan^{-1}(4\mathrm{Kn}^{0.4}) \tag{17}$$

The permeability correction factor is defined in Equation 18,

$$\mathrm{f(Kn)} = (1 + \alpha\mathrm{Kn})\left(1 + \frac{4\mathrm{Kn}}{1 - \mathrm{bKn}}\right) \tag{18}$$

Under full slip conditions, we have:

$$\mathrm{f(Kn)} = 1 + \frac{4\mathrm{Kn}}{1 + \mathrm{Kn}}$$

$$\therefore \mathrm{K_a} = \mathrm{K_\infty f(Kn)} = \mathrm{k_\infty}\left(1 + \frac{4\mathrm{Kn}}{1 + \mathrm{Kn}}\right) \tag{19}$$

Figure 13 shows Knudsen number increases with a decrease in pore size for specified values of pressure and temperature and for a fixed pore diameter, the Knudsen number increases as pore pressure decreases. In other words, slip flow effects become dominant under low pressure conditions and in small pores.

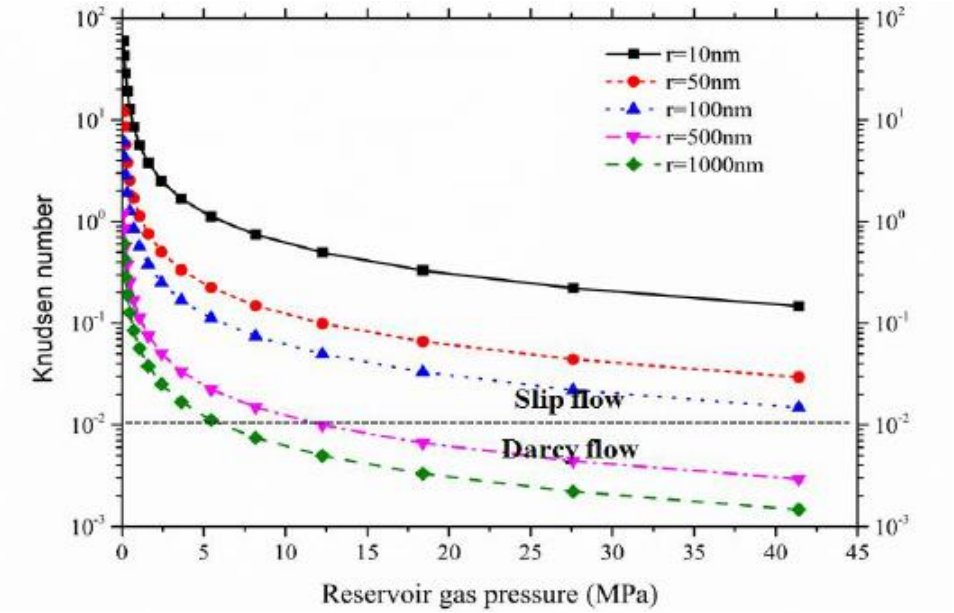

Figure 13. Effect of pore size on Knudsen number (Zhang and Hu, 2014)

As indicated earlier, there are several recent developments in modeling gas flows in shales. (Swami et al. 2012) Several of these are based on the use of the Knudsen number (Beskok and Karniadakis, 1999) while others are extensions to the Klinkenberg slip model (Fathi et al., 2012). In this work we chose the model provided in Civan (2010) because the differences between the various models for slip flow is not appreciable as shown in the work done by Swami et al. (2012) and shown in Figure 14 and Figure 15. Figure 14 plots the ratio of apparent permeability k_a to the matrix permeability k_m, k_a/k_m and shows that increases as pressure decreases for each of the 10 different models shown. Figure 15 shows k_a/k_m also increases with a decrease in pore diameter at specified pressure and temperature conditions for all models. An overview of these methods is provided in Table 3.

Table 3. Different approaches to model slippage effect

Type 1	**Authors**	**Eqn.**
Apparent or effective permeability related to Klinkenberg slippage factor, b_K	Jones & Owens (1980)	$b_K = 12.639(k_\infty)^{-0.33}$
	Sampath & Keighin (1982)	$b_K = 13.581\left(\frac{k_\infty}{\emptyset}\right)^{-0.53}$
	Florence et al. (2007)	$b_K = 43.345\left(\frac{k_\infty}{\emptyset}\right)^{-0.5}$
Type 2	**Authors**	**Eqn.**
Slippage factor on basis of Knudsen diffusion, valid for slip flow regime.	Ertekin et al. (1986)	$D_K = \frac{31.54}{\sqrt{M}}(k_\infty)^{0.67}$ $b_K = \frac{\overline{P} D_K \mu c_g}{\alpha k_\infty}$
	Beskok & Karniadakis (1999)	$b_K = \frac{3\pi D_K \mu}{2r^2}$
Type 3.	**Authors**	**Eqn.**

Based on Beskok & Karniadakis (1999) work, valid for slip and transition flow regimes.	Sakhaee-Pour & Bryant (2012)	$k_a = k_\infty(0.8453 + 5.4576Kn + 0.1633Kn^2$ *Valid for $0.1 \leq Kn \leq 0.8$
	Civan (2010) Civan A. method	$k_a = k_\infty f(Kn)$ $f(Kn) = (1 + \alpha Kn)\left(1 + \frac{4Kn}{1-b}\right)$ $\alpha = a_0\left(\frac{Kn^B}{A + Kn^B}\right)$ $a_0 = 1.358$ A=0.178 B=0.4348 Slip coefficient $b = -1$
Based on the work of Florence et al (2007) work for Kn<<1.	Civan (2010) Civan B. method	$b_K = \frac{2790\mu}{\sqrt{M}}\left(\frac{k_\infty}{\emptyset}\right)^{-0.5}$
Type 4	**Authors**	**Eqn.**
Equivalent permeability including Knudsen diffusion and slippage	Javadpour et al. (2007) and Javadpour et al. (2009) *But they do not include slippage which occurs because of molecular collision with pore walls.	$k_a = \frac{D_K \mu M}{RT\rho} + Fk_D$ D_K : Knudsen diffusion coefficient μ : Gas viscosity ρ : Average gas density F: Slippage factor k_D: Darcy's permeability F is given by Brown et al, 1946 $F = 1 + \left(\frac{8\pi RT}{M}\right)^{0.5} \frac{\mu}{\overline{Pr}}\left(\frac{2}{f} - 1\right)$
Type 5	**Authors**	**Eqn.**
Correction to Klinkenberg's theory	Fathi et al. (2012)	$k_a = k_\infty\left[1 + \left(\frac{b_K}{\overline{P}}\right)^2\left(\frac{L_{KE}}{\lambda}\right)\right]$ Where, L_{KE} is the length scale associated with the kinetic energy of molecules that bounce back after colliding with the pore wall. They report $\frac{L_{KE}}{\lambda} \approx 2.05$ with Lattice Boltzmann method for a pore size of 6.5nm.

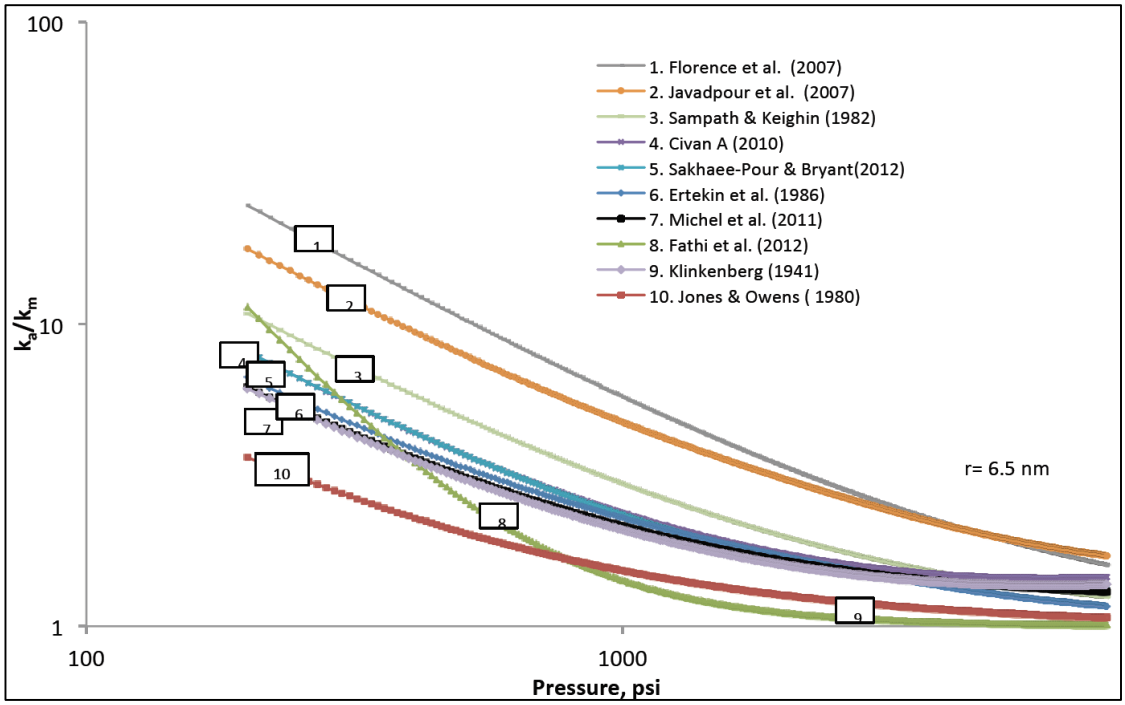

Figure 14. k_a/k_m versus average pressure (200~8,000 psia) for pore radius 6.5nm (Swami et al. 2012)

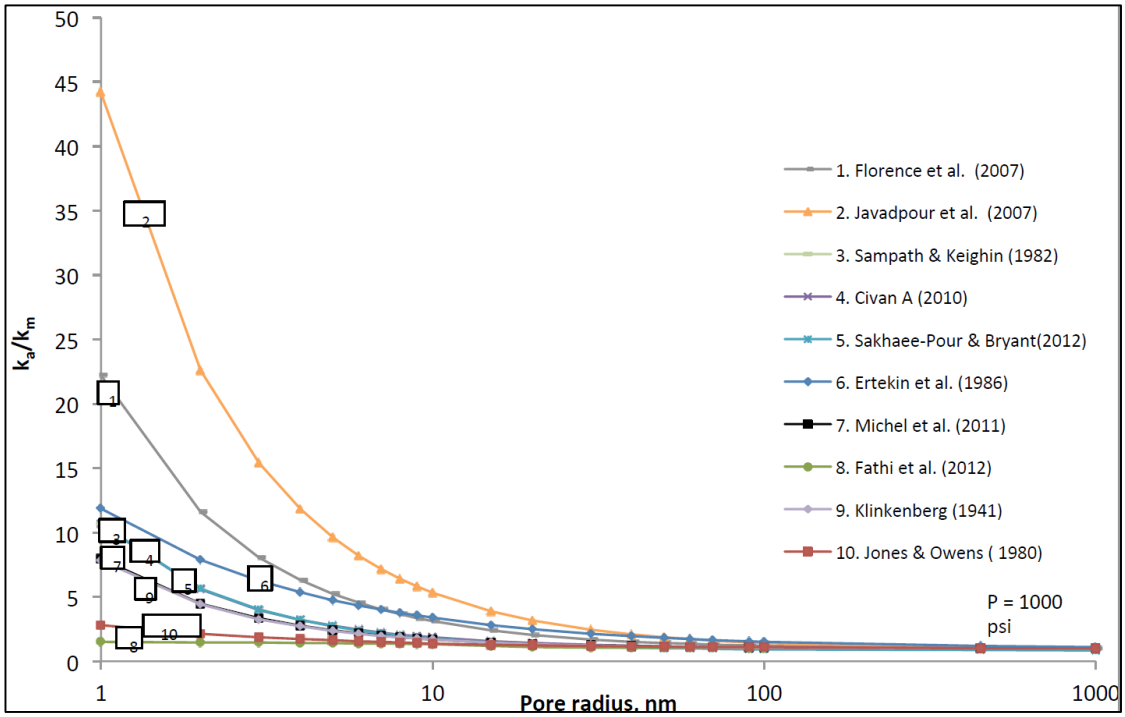

Figure 15. k_a/k_m versus pore radius (1~ 1,000nm) at an average pressure 1,000 psia (Swami et al. 2012)

2.2.3. Extension to Multicomponent Flows

Based on the equation for the mean free path for a single-component in a multi-component gas mixture as shown in Equation 9, we can define a Knudsen number for each component in the mixture.

$$\mathrm{Kn_i} = \frac{\lambda_i}{\mathrm{R_{eff}}} \tag{20}$$

Because component 'i' is moving with an apparent permeability given by $K_\infty f(Kn_i)$, the relative flux of component 'i' is given by Equation 21:

$$\widetilde{y_i} = \frac{y_i f(\mathrm{Kn_i})}{\sum_{i=1}^{n} y_i f(\mathrm{Kn_i})} \tag{21}$$

The phase permeability can be estimated by the definition of molar flux of the multi-component mixture and absolute permeability for a simple cylindrical shape capillary tube. Equations 22 and 23 describe the molar flux for a multicomponent mixture.

$$\dot{n} = \frac{\sum_{i=1}^{n} n_{v_i} K_\infty f(\mathrm{Kn_i})}{\mu} \nabla P \tag{22}$$

$$\dot{n} = n_v \frac{K_{amix}}{\mu} \nabla P \tag{23}$$

Therefore,

$$n_v \frac{K_{amix}}{\mu} \nabla P = \frac{\sum_{i=1}^{n} n_{v_i} K_\infty f(\mathrm{Kn_i})}{\mu} \nabla P \tag{24}$$

$$K_{amix} = K_\infty \sum_{i=1}^{n} y_i f(\mathrm{Kn_i})$$

$$\text{where } y_i = n_i / n_v$$

$$K_\infty = \frac{N \pi R_{eff}^4(P)}{8 A_c} \tag{25}$$

Where, N : Number of capillary tubes
R_{eff} : Effective pore radius, [m]
A_c : Cross sectional area, [m^2]

2.2.4. Slip Flow Effects from Recent Experimental Data

Mathur (2015) conducted a series of experiments using helium and nitrogen in shale samples to determine the apparent permeability corresponding to different flow regimes (Transient flow or slip flow) for the following pressure ranges:

1. 100 to 250 psi
2. 800 to 1,200 psi
3. 1,800 to 2,200 psi
4. 2,800 to 3,200 psi

Based on the observations from these experiments to measure shale sample permeability using helium and nitrogen across a wide range of pressures, Mathur (2015) indicates that approximately below 2,000 psia, slip flow effects may be dominant and appropriate corrections are necessary. However, when the pore pressure is above 2,000 psi, there is no experimental evidence for slip flow in the samples tested and consequently, a slip flow correction may be unnecessary. This is a significant result because current development activity in most shale plays is in regions where the pore pressures as well as the bottomhole flowing pressures are considerably above 2,000 psia. For all practical purposes a slip flow correction may be unnecessary. However Mathur (2015) also notes that for experimental determination of permeability to gas at low pressures, these corrections may be important. Table 4 provides a description of the corrections necessary based on Mathur (2015).

Table 4. Flow regimes in shales with the corresponding correction (Mathur, 2015).

Pore pressure, psia	Correction method	Dominant flow regime
$P_P < 500$	Double slip correction	Transition flow
$800 \leq P_P \leq 1{,}200$	Klinkenberg correction	Slip flow
$P_P > 2{,}000$	Uncorrected	-

2.3. Diffusion Coefficients

Molecular diffusion and Knudsen diffusion are the 2 most common types of diffusion observed in porous media (Ho and Webb, 2006). However, other forms of gas phase diffusion in porous media such as surface diffusion and configurational diffusion are not considered in this thesis. The following sections provide an overview of these transport mechanisms.

2.3.1. Molecular Diffusion

Consider a 1D system with a gas mixture of two components A and B. If there is a concentration gradient, then molecular diffusion of component A will occur and it can be described by Fick's law as shown below in Equation 26 (Freeman et al. 2012).

$$J_A = -D_{AB}\left(\frac{dc_A}{dx}\right) \tag{26}$$

where, D_{AB} : Binary molecular diffusion coefficient of A through B,$[m^2/s]$

$\frac{dc_A}{dx}$: Concentration gradient along the $x-$ axis

Binary molecular diffusion coefficient D_{AB} can be estimated by using Equation 27 (Cowling, 1970):

$$D_{AB} = \frac{3}{8n_v\sigma_{AB}^2}\sqrt{\frac{k_B T}{2\pi}\left(\frac{1}{M_A}+\frac{1}{M_B}\right)} \tag{27}$$

Equation 27 can expressed as shown in Equation 28 by applying the ideal gas law and the Boltzmann coefficient k_B,

$$n_v = \frac{P}{k_B T}$$

$$D_{AB}[cm^2/s] = 0.000018583\sqrt{T^3\left(\frac{1}{M_A}+\frac{1}{M_B}\right)}\frac{1}{P\sigma_{AB}^2\Omega_D} \tag{28}$$

where, T : Temperature, [K]

P : Pressure, [atm]

M_A, M_B : Molecular weights of A and B, [g/mol]

σ_{AB}^2 : Average collision factor of A and B

Ω_D : Dimensionless collision integral

σ : Lennard − Jones diameter, [nm]

$\sigma_{AB} = (\sigma_A + \sigma_B)/2$

2.3.2. Knudsen Diffusion

With decrease of the pore diameter, the collision of gas molecules with the pore wall become more frequent than collisions between the gas molecules themselves. The diffusion of gas molecules that includes molecule – pore wall collisions is called Knudsen diffusion.

Knudsen diffusion coefficient, $D_{K,A}$ *i*s defined as below Equation 29 (Mason and Malinauskas, 1983):

$$J_A = -D_{K,A}\left(\frac{dc_A}{dx}\right) \tag{29}$$

The Knudsen diffusion coefficient $D_{K,A}$ is related to the mean molecular velocity, $\overline{V} = \sqrt{\frac{8RT}{\pi M}}$ and defined as shown in Equation 30 and Equation 31 depending on the pore geometry. For a cylindrical pore:

$$D_{K,A} = \frac{d_P}{3}\sqrt{\frac{8RT}{\pi M}} \tag{30}$$

For typical porous media with tortuous pore networks:

$$D^{eff}_{K,A} = \frac{\varepsilon_P}{\tau_K}\frac{d_P}{3}\sqrt{\frac{8RT}{\pi M}} \tag{31}$$

where, d_P : Pore diameter, [m]

M : Molecular weight, [g/mol]

ε_P : Relative pore volume

τ_K : Tortuosity

Equation 31 describes the 'Effective diffusion coefficient' that includes the effect of tortuosity in porous media and such corrections are made for molecular diffusion as well (Webb, 1996). Figure 16 illustrates tortuosity (Lister and Djilali, 2005) which is defined as:

$$\tau = \left(\frac{\text{Actual Path Length}}{\text{Point to point path length}}\right)^2 \tag{32}$$

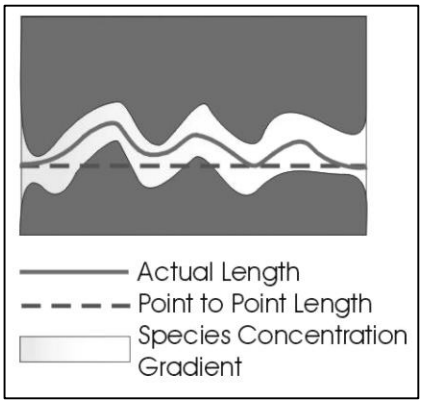

Figure 16. Schematic of tortuosity (Lister and Djilali, 2005)

2.3.3. Equivalent Diffusivity

Using the Bosanquet (1923) equation, the combined diffusion coefficient including molecular diffusion and Knudsen diffusion can be determined to give the equivalent diffusivity $\bar{D}$ (Zalc et al., 2004). Figure 17 illustrates molecular movement corresponding to each type of diffusion.

$$\frac{1}{\bar{D}} \cong \frac{1}{D_{AB}} + \frac{1}{D_{K,A}} \tag{33}$$

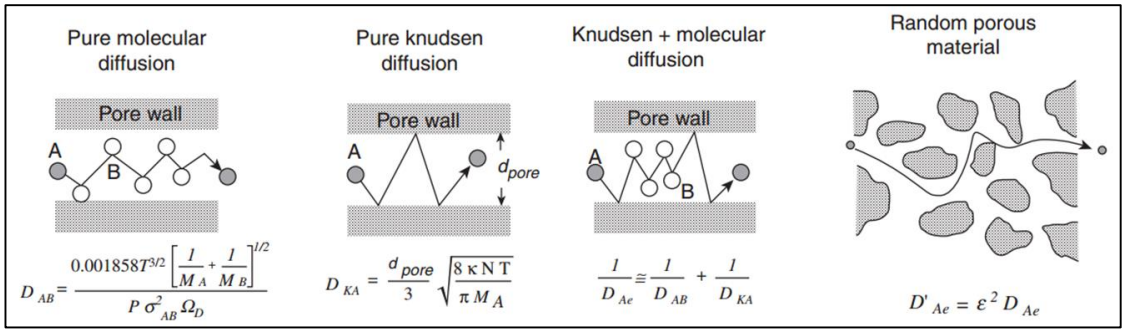

Figure 17. Types of porous diffusion (Welty et al., 2009)

2.3.4. Two Phase Diffusion

Under certain pressure and temperature conditions such as below the fluid saturation pressure, the fluid may exist as two phases and consequently, diffusion in both the oil and gas phase should be considered. The diffusion coefficients of each component in different phases is likely to be different as shown below Figure 18 (Hoteit, 2013) for the diffusion of nitrogen in oil and gas phases. The results from Hoteit (2013) indicate that the diffusion coefficient in the gas phase can be two orders of magnitude larger than the diffusion coefficient in the liquid phase.

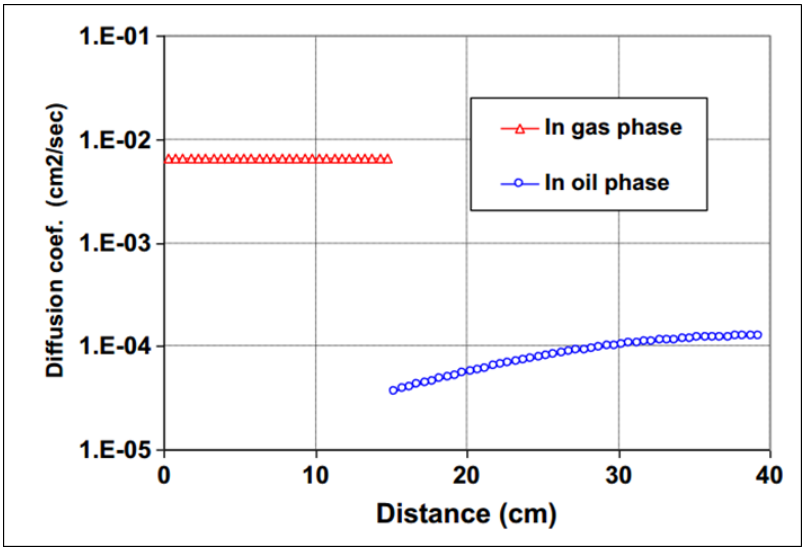

Figure 18. Nitrogen diffusion coefficients in gas and oil phase (Hoteit, 2013)

2.4. Pore Proximity Effect

Several authors have also documented a phenomenon called the pore proximity effect that is restricted to small pores and causes variations in the critical properties of the individual components in the fluid. Figure 19 shows pore diameter distribution in an organic shale sample showing numerous pores with less than 10nm diameter and containing 20 to 40% of the pore volume. (Curtis et al., 2010 and Sigal, 2015)

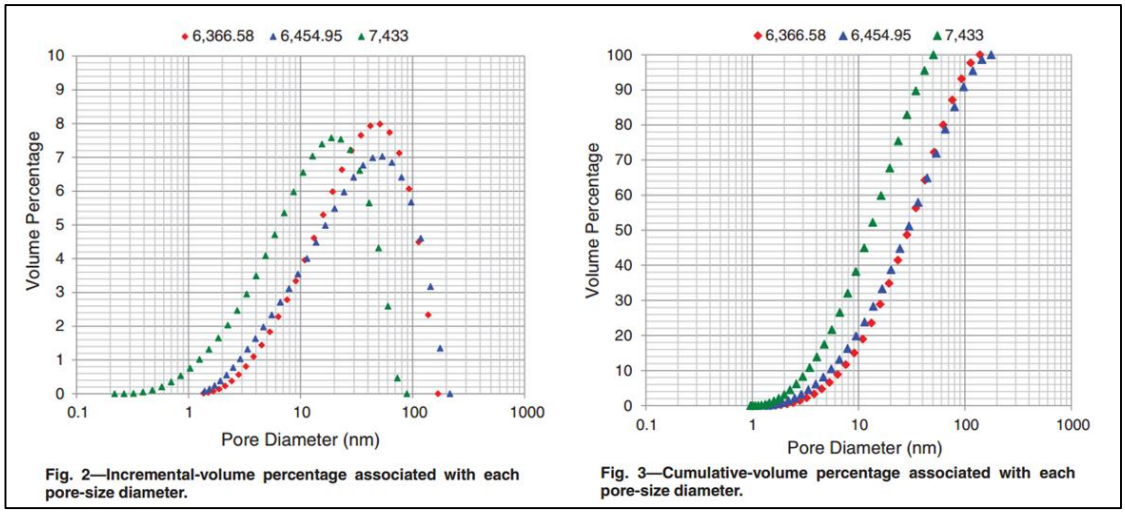

Figure 19. Pore size distribution in organic shale (Sigal, 2015)

Jin et al. (2013) proposed a correlation that can predict critical pressure and critical temperature changes under confinement as shown below in Table 5 to estimate the pore proximity effect.

Table 5. Critical properties change under confinement (Jin et al., 2013)

Critical temperature, K	$T_{cp} = T_{cb} \times \left(0.985 - 0.8493 \times \left(\frac{D}{\sigma}\right)^{-1.241}\right)$
Critical pressure, MPa	$P_{cp} = P_{cb} \times \left(1 - 1.8 \times \left(\frac{D}{\sigma}\right)^{-0.775}\right)$

Table 6. Six components fluid composition

Component	C1	C2	C3	C4	C5	C6
Fraction	0.8	0.07	0.05	0.05	0.02	0.01

Because of the changes in the critical pressure and critical temperature of all components, the result is a change in the phase diagram. Figure 20 shows the phase diagram in a 4nm diameter pore in comparison to the bulk fluid phase diagram.

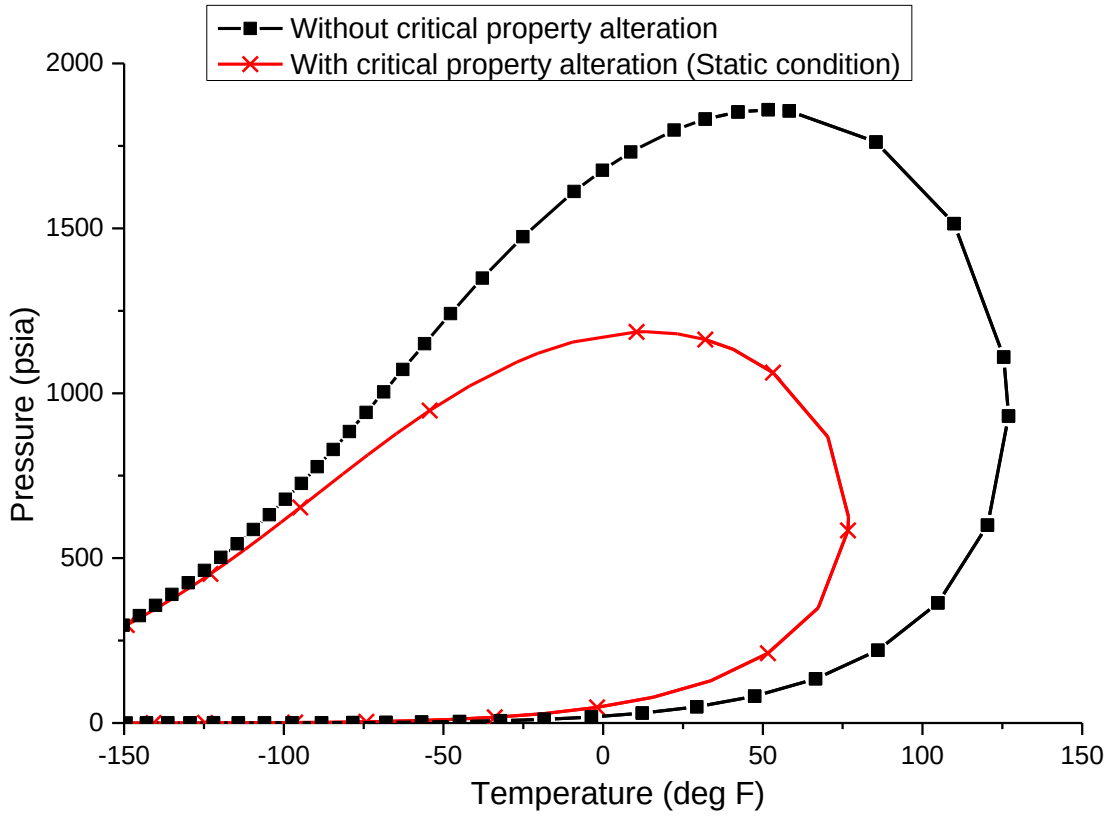

Figure 20. Phase diagram shrinks with critical properties alteration
(Bulk vs. 4nm pore size)

The phase diagram has been shown to change as a function of pore size; however these effects are expected to vanish for pores with a diameter larger than approximately 20 nm. Consequently, although the pore proximity effect may be appreciable in small pores,

this is likely not to have an appreciable impact because the pore volume contained in the smallest of pores typically tends to be less.

The constant GOR trends shown earlier in Chapter 2 have been previously attributed to the pore proximity effect and shrinkage of the phase envelope (Devegowda et al. 2012). In this thesis, I do not consider any pore proximity effects to underscore the significance of Knudsen diffusion to constant GOR flows.

Chapter 3. 1D Multicomponent Gas Flow

The previous chapter provided an overview of the predominant flow mechanisms for gas in nanoporous media. It is important to note that while molecular diffusion is prevalent across all pressure ranges, Knudsen diffusion is generally significant only at lower pore pressures. In this chapter, I examine the effects of the Knudsen diffusion on the produced fluid composition in a synthetic case study with a multicomponent fluid. This 1-D simulator was developed in-house and incorporates the Civan (2010) 'A method' as well as the Florence et al. (2007) approach for single- and multicomponent fluids.

3.1. Case Study: Grid and Fluid Properties

In this case study, a grid system consisting of five cells is chosen to represent flow through a cylindrical nanoscale pore of various diameters. Figure 21 is a schematic of the grid system. Cell 1 has about $6e^7$ times the volume of the other cells and therefore acts as a large but finite source and is chosen to represent an isolated organic body. Cell 5 is open to flow and represents flow to a fracture or to another larger pore.

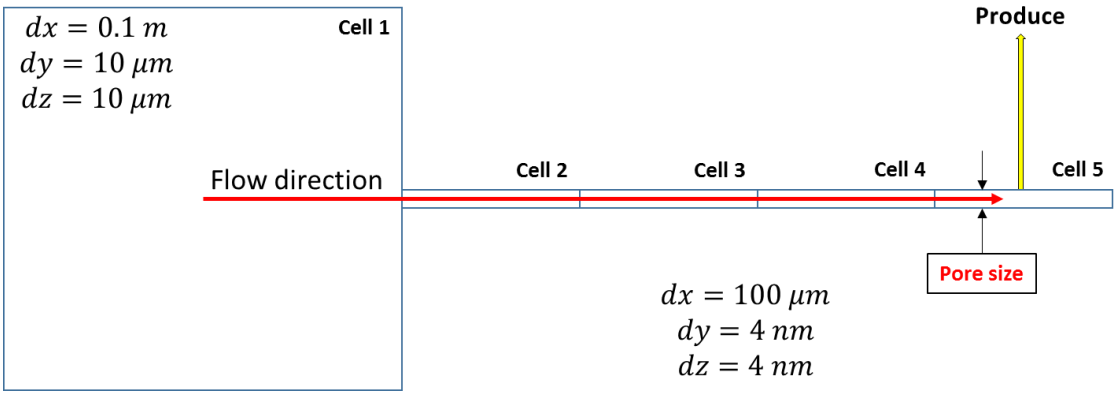

Figure 21. Simple one dimension grid model

For this case study, the fluid under consideration is the six-component sample provided in Table 6. Figure 22 plots the Knudsen number, Kn as a function of pore pressure and pore size for 3 different components, C1, C2 and C6. It readily becomes apparent that the Knudsen number in the case of multicomponent gas flows follow the same trends as shown with single-component fluids in Figure 22. The Knudsen number also shows a marked decrease in value from the lighter component, C1 to the heavier components, C2 and C6 at the same pore pressure. The differences in the Knudsen number corresponding to each component will therefore also lead to different velocities for each component. Figure 23 plots the variations in the quantity, $f(Kn_i)$ as defined in Equation 18 as a function of pore pressure and pore diameter for 3 components, C1, C2 and C6.

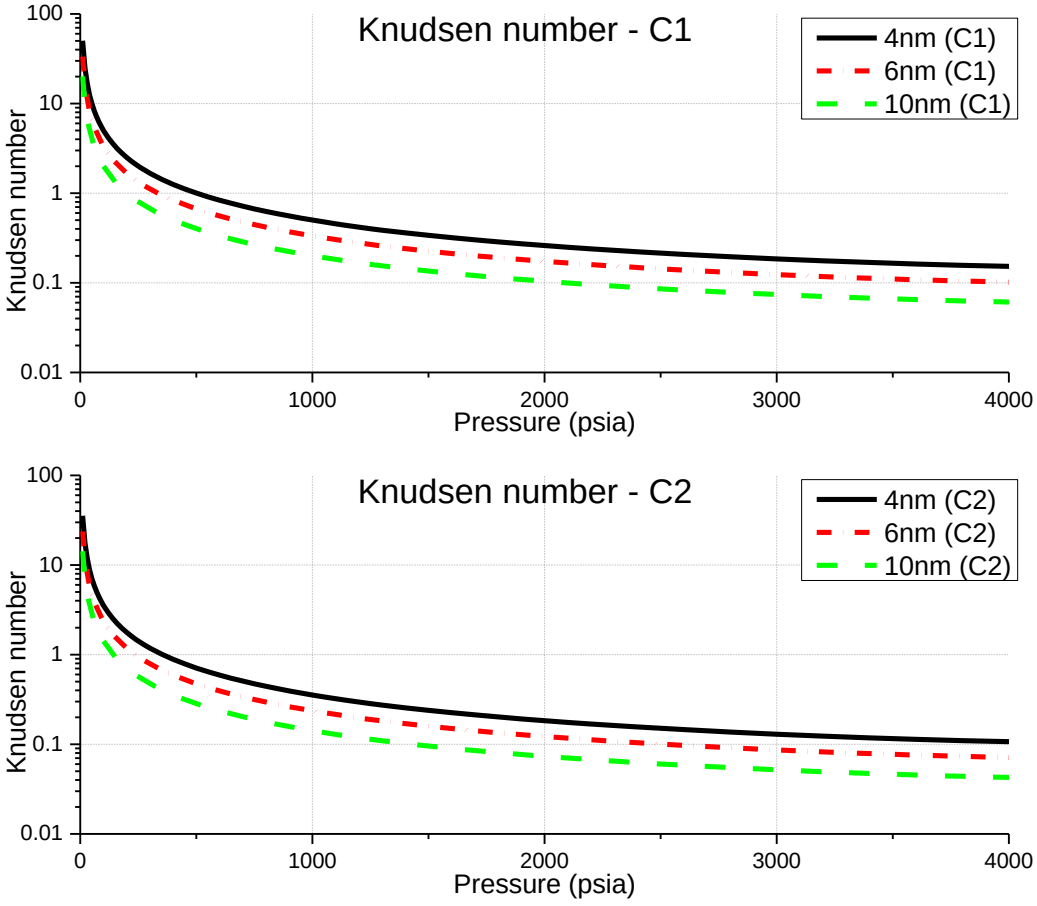

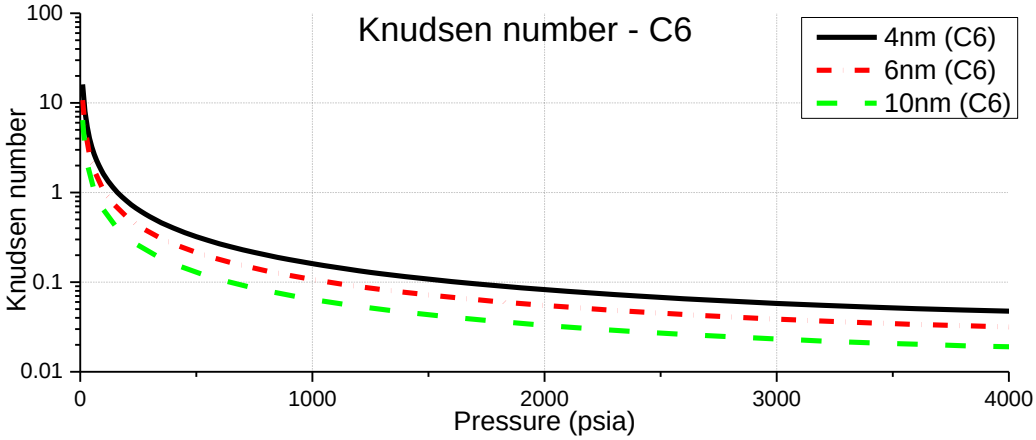

Figure 22. Knudsen number as a function of pore pressure for different pore diameters.

Again, individually the variations in the permeability correction follow similar trends corresponding to single-component gas flows. However a closer inspection reveals that there are marginal differences between the quantity, $f(Kn_i)$, for C1 and C2 and more appreciable differences between the lighter (C1 and C2) components and the heavier C6 fraction. Consequently, this implies that when flow occurs under a pressure gradient, C1 molecules are likely to move more rapidly in comparison to the C2 fraction. The C6 molecules because of their higher molecular weight are likely to move at a slower rate in comparison to C1 and C2. The results also indicate that while the effects of Knudsen diffusion are minimal and restricted to low pore pressures for the heavier components, they may be significant for the lighter components, C1 and C2 over a wider range of pressures. At 4,000 psia for instance, in a 10 nm pore, the value of $f(Kn_i)$ for C1 is 1.3, indicating that there is 30% increase in the transmissibility to methane at higher pressures. Although the work presented in this chapter indicates a higher mobility for the lighter components as a consequence of the increased effects of Knudsen diffusion in small pores, there is a need for experimental verification of the theory presented here in order to validate these conclusions.

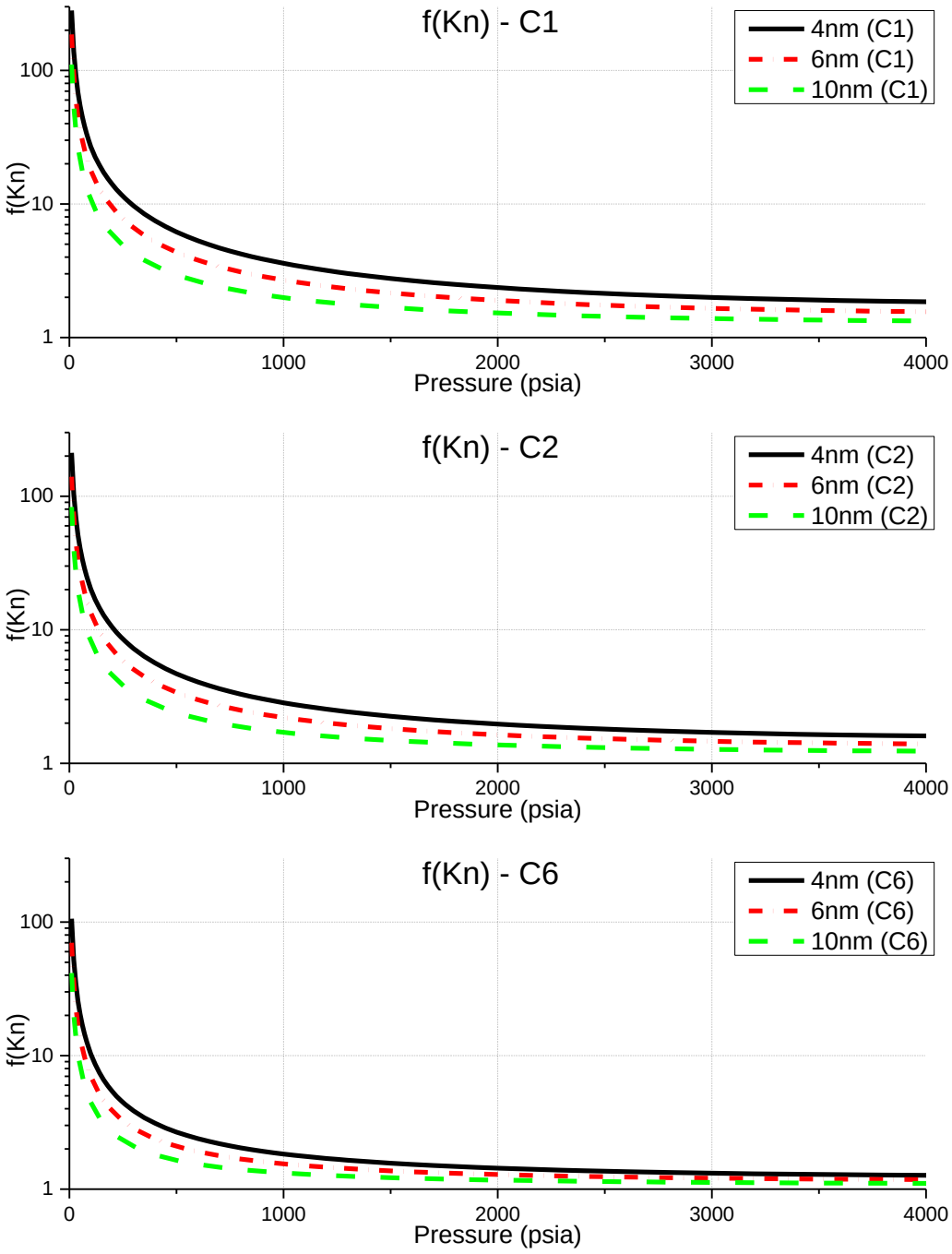

Figure 23. f(Kn) as a function of pore pressure for different pore diameters.

I use the 1-D simulator for multicomponent gas flows to illustrate the differences in flowing gas composition for the case study described earlier in Figure 21.

3.2. Results from the Case Study

3.2.1. Multicomponent Gas Transport via Knudsen Diffusion

In order to avoid multiphase flow effects, for all case studies I maintain a pore pressure in excess of the fluid dew-point pressure. The producing well operates at a constant bottomhole pressure. The reservoir conditions provided below are employed to simulate flow of the 6-component gas mixture provided in Table 6. Gas viscosity was estimated using the Lee, Gonzales and Eakin correlation. (Lee et al., 1966) And iteration time step is one second.

1. Reservoir Temperature = 300 °F
2. Initial pressure = 3,000 psia
3. Pore diameter = 4 nm, 6 nm, 10 nm

Figure 24 and Figure 25 illustrate the variations in the produced fluid composition in terms of the lighter (C1) component fraction and the heavier (C2 through C6) component fractions respectively computed using Equation 21 for a 4nm diameter pore. The original mole fraction of C1 is 0.8 while Figure 24 indicates that the initial mole fraction of C1 in the produced fluid is higher. This is a consequence of the variations in the quantity, $f(Kn_i)$ for each of the components in the mixture as shown in Figure 25. Figure 25 shows that the initial mole fractions of the heavier components in the produced fluid are marginally lower. This indicates that under drawdown, the produced fluid is likely to be lighter in composition in comparison to the original fluid.

At later time periods, Figure 24 and Figure 25 indicate that the produced fluid composition becomes identical to the in-situ fluid composition. This is a consequence of

the geometry of the problem as defined in Figure 21 where Cell 1 serves as a very large source and therefore the produced fluid composition eventually approaches steady state conditions and returns to the original fluid composition. I chose this arrangement because for transient flow in shale wells the source may be considered to be infinite. However, the case study defined in Figure 21 is an overly simplistic view of multicomponent flows. Again, in reality, flow rarely occurs through tubes of a specified diameter. Instead, the connectivity within shales may be defined by a complex network of pores and pore throats and these may lead to varying Knudsen diffusion effects depending on the local composition and the local flow geometry. I provided composition change ratio plot of below Figure 24 to Figure 31 compared with its original composition in Appendix B.

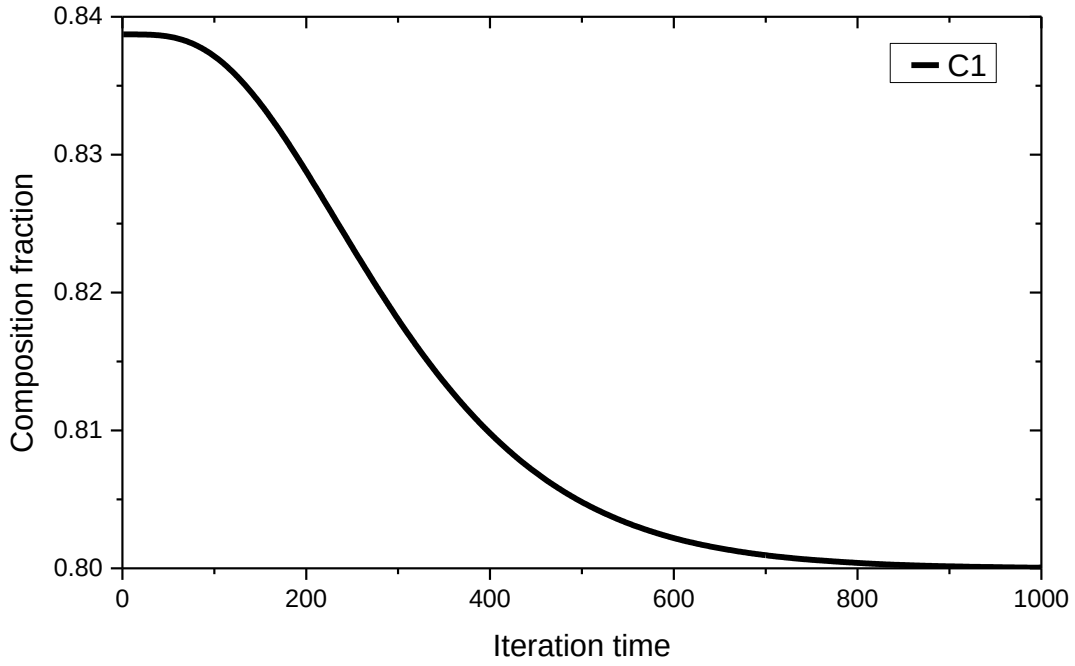

Figure 24. C1 mole fraction in the produced fluid as a function of time. (4nm pore)

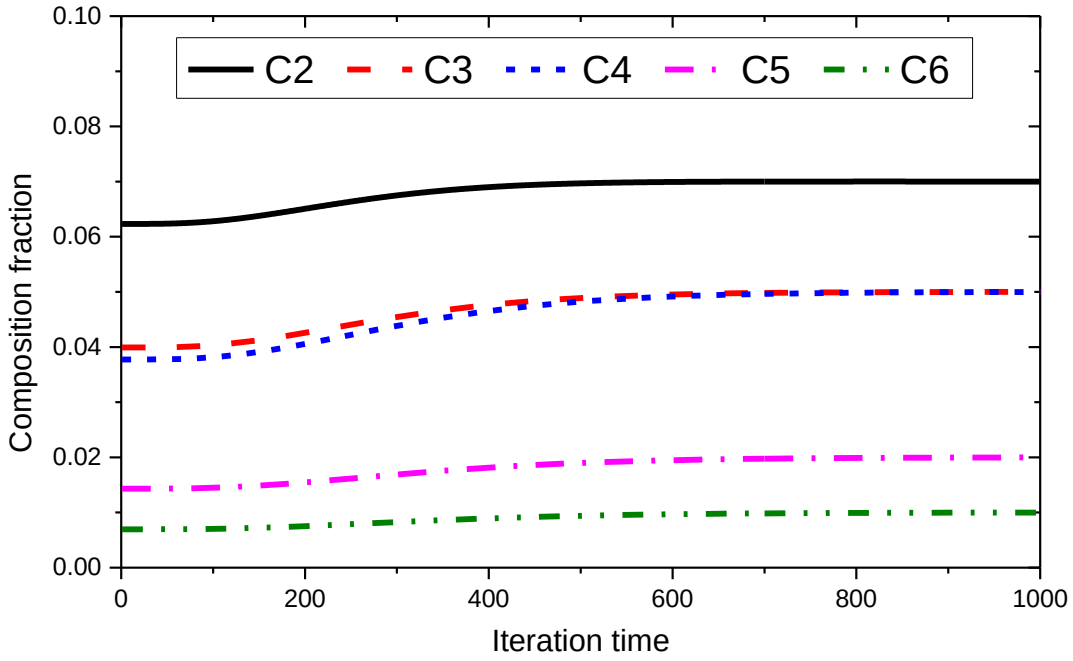

Figure 25. C2-C6 mole fractions in the produced fluid as a function of time. (4nm pore)

Because Knudsen diffusion varies with pore diameter, this case study includes a comparison of the produced fluid compositions for pores of diameter 4nm, 6nm, and 10nm as shown below in Figure 26 to Figure 31. In each of these case studies, the produced fluid is shown to be lighter in composition in comparison to the original reservoir fluid, although the severity of the variations diminishes with increased pore diameter.

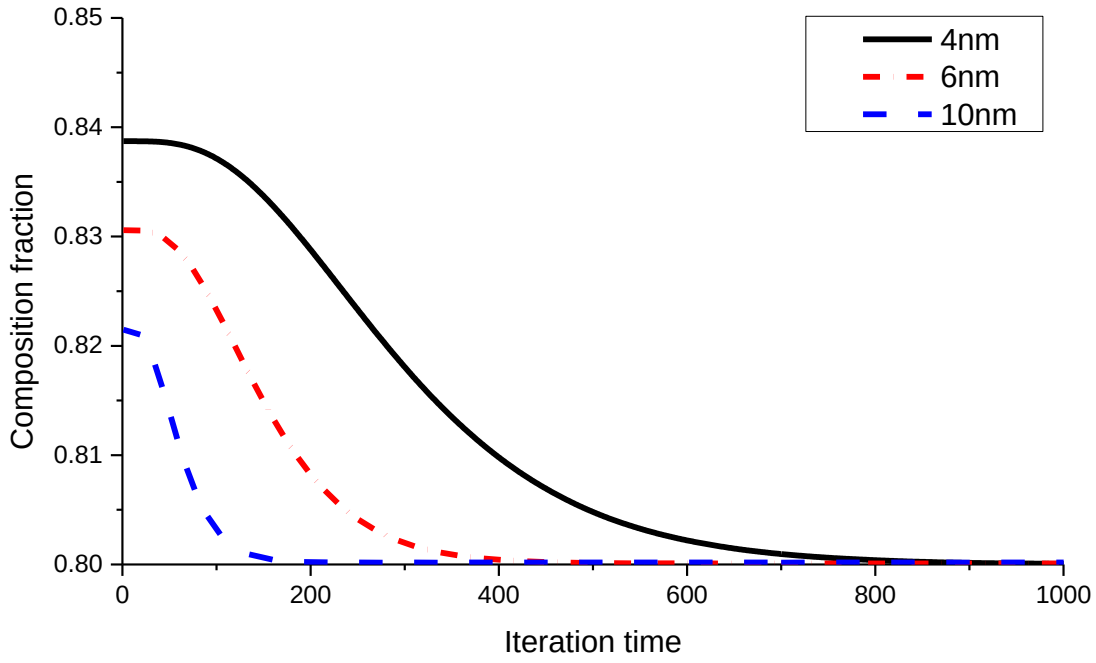

Figure 26. C1 mole fraction in the produced fluid as a function of time in 4nm, 6nm, 10nm diameter pores.

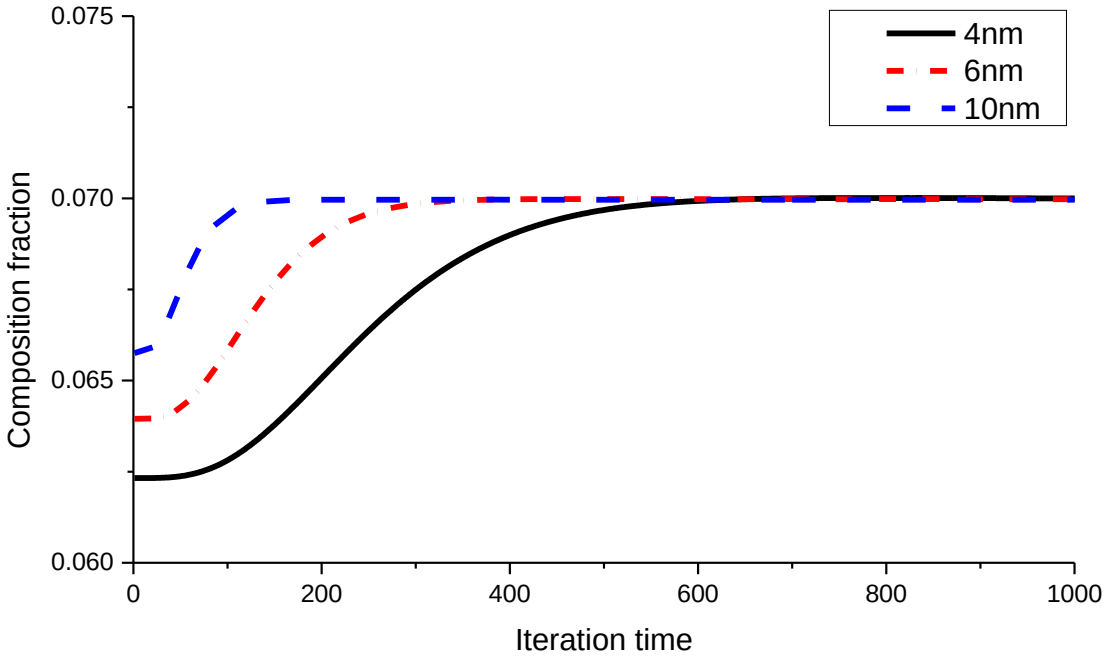

Figure 27. C2 mole fraction in the produced fluid as a function of time in 4nm, 6nm, 10nm diameter pores.

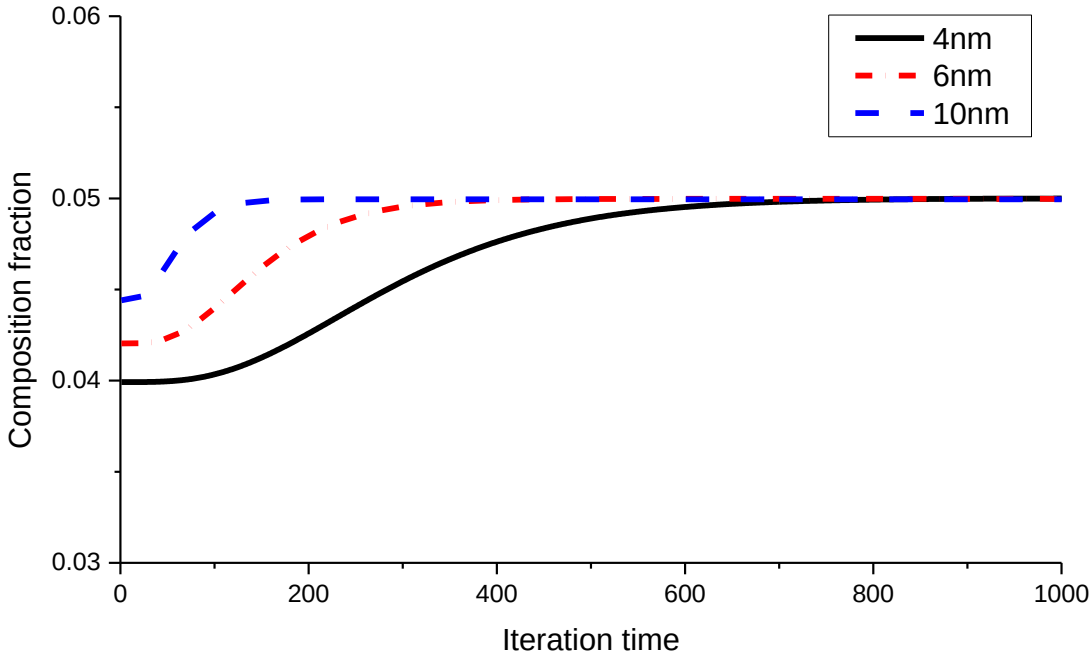

Figure 28. C3 mole fraction in the produced fluid as a function of time in 4nm, 6nm, 10nm diameter pores.

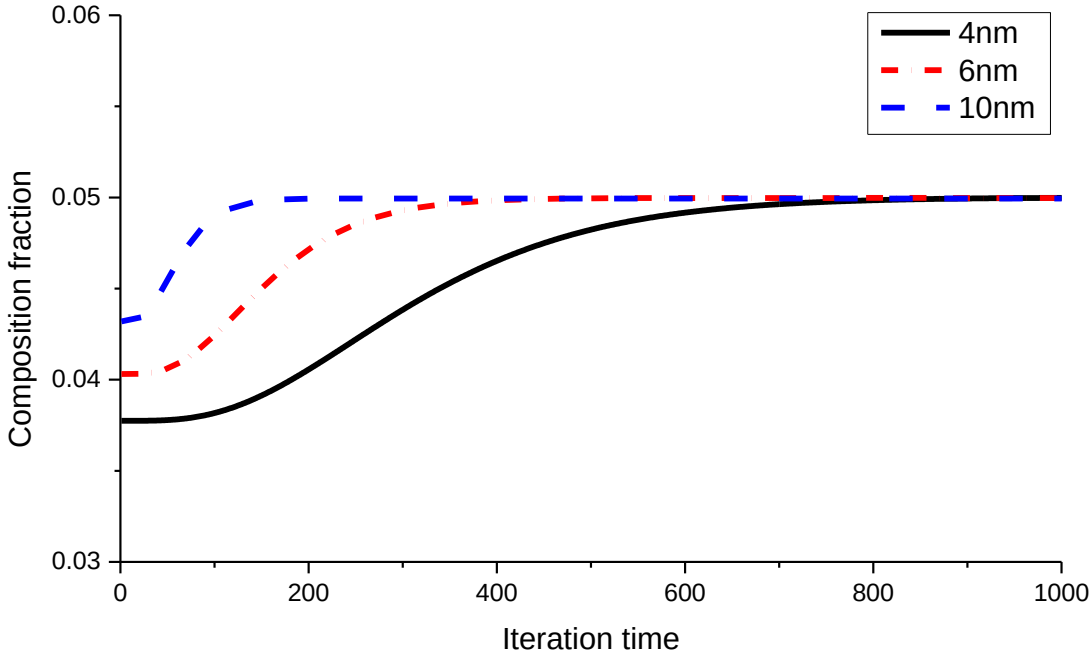

Figure 29. C4 mole fraction in the produced fluid as a function of time in 4nm, 6nm, 10nm diameter pores.

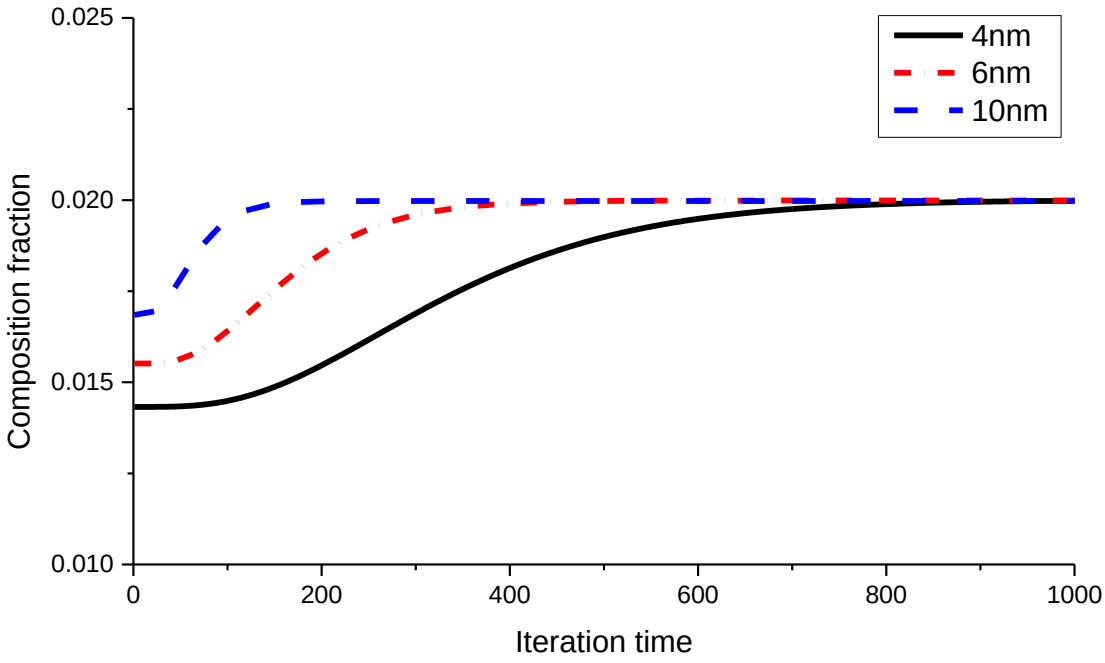

Figure 30. C5 mole fraction in the produced fluid as a function of time in 4nm, 6nm, 10nm diameter pores.

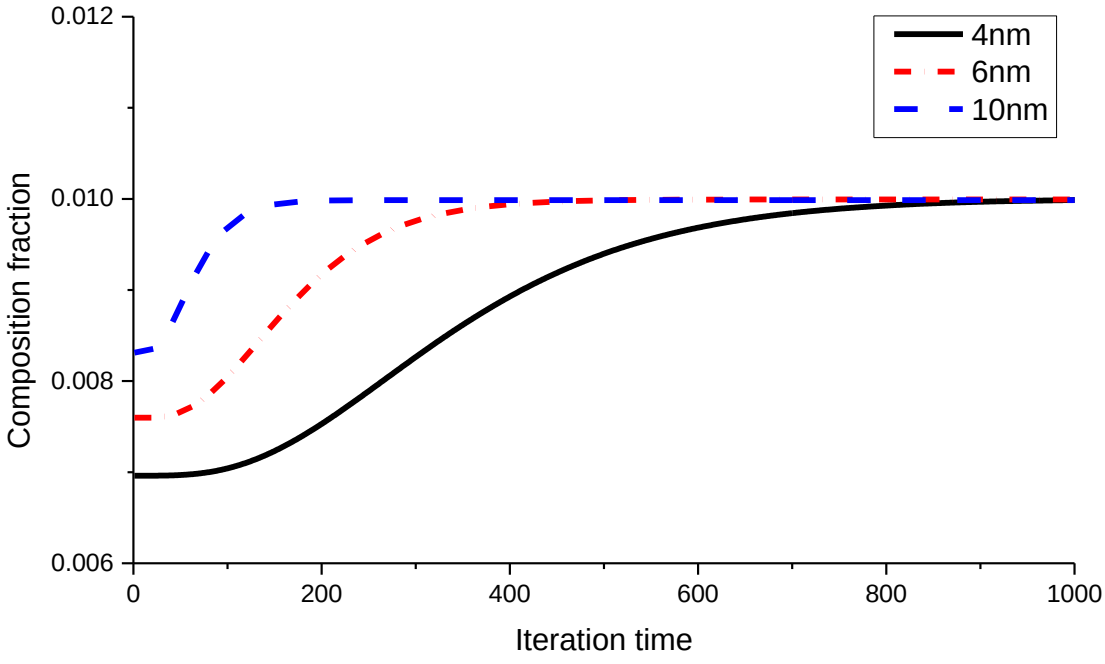

Figure 31. C6 mole fraction in the produced fluid as a function of time in 4nm, 6nm, 10nm diameter pores.

There are several conclusions to be drawn from this case study. Although in this work, I am neglecting the effect of adsorption as indicated earlier, multicomponent adsorption is

likely to increase the severity of the variations shown in the preceding figures. This is because heavier components tend to be more readily adsorbed in comparison to the lighter components. (Do et al., 2001)

Secondly, Figure 26 to Figure 31 indicate that multicomponent flow in nanopores may cause the remaining fluid in the reservoir to become heavier in composition and therefore condense. However, this may not necessarily be the case. An analysis of the compositions within each grid cell of the case study presented here highlights the reasons for a lack of condensation of the heavier components as the lighter components are transported out of each grid cell. When flow is initiated, lighter components leave Cell 5 at a faster rate than the heavier components; however, simultaneously, the lighter components from Cell 4 are also being transported to Cell 5 at a faster rate than the heavier components. So the composition in Cell 5 remains relatively stable for an extended period of time as shown in Figure 32. This implies that for condensate shale wells the compositions within the reservoir may be relatively stable in comparison to the produced fluid compositions.

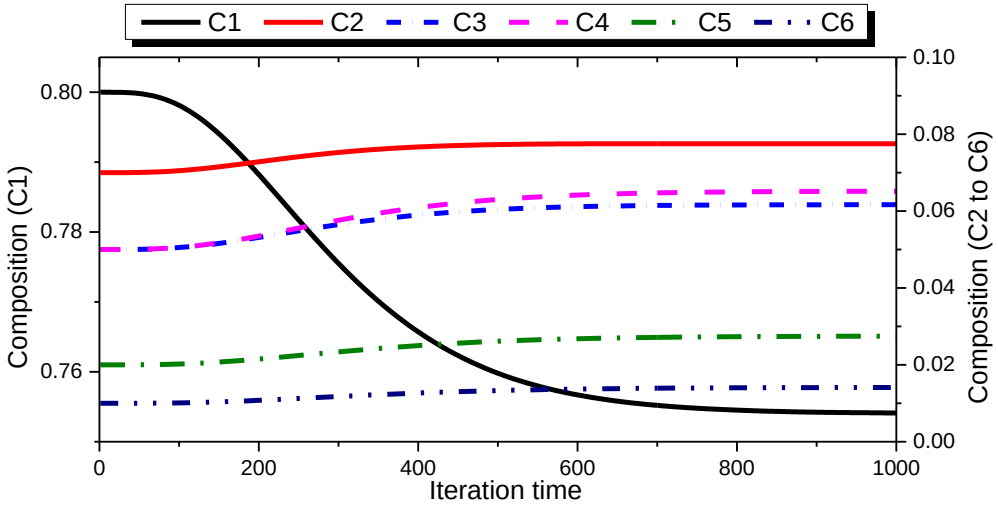

Figure 32. Composition of the fluid located in Cell 5. (4nm pore)

3.2.2. Sensitivity with Initial Pressure

In order to evaluate the sensitivity of the variations in the produced fluid compositions as a function of initial reservoir pressure, I also run a few case studies with different initial reservoir pressure as shown in Table 7 based on 4nm pore size case for the fluid whose composition is provided in Table 6.

Table 7. Different initial pressure cases

Case #	Initial pressure (psia)
Base case	3,000
Case 1	4,000
Case 2	5,000
Case 3	6,000
Case 4	7,000

Figure 33 to Figure 35 show the trends in the produced fluid compositions for different initial reservoir pressures and indicate that the severity of the variations again diminishes with increased reservoir pressures. This is analogous to the argument provided in Chapter 2 where the apparent permeability correction was shown to have a minimal effect on the permeability to gas at higher reservoir pressures or for small Knudsen number flows when Darcy flow may be considered to be valid. In the case of multicomponent flows, we observe a similar effect. The produced fluid composition is closer to the original reservoir fluid when the initial reservoir pressure is higher.

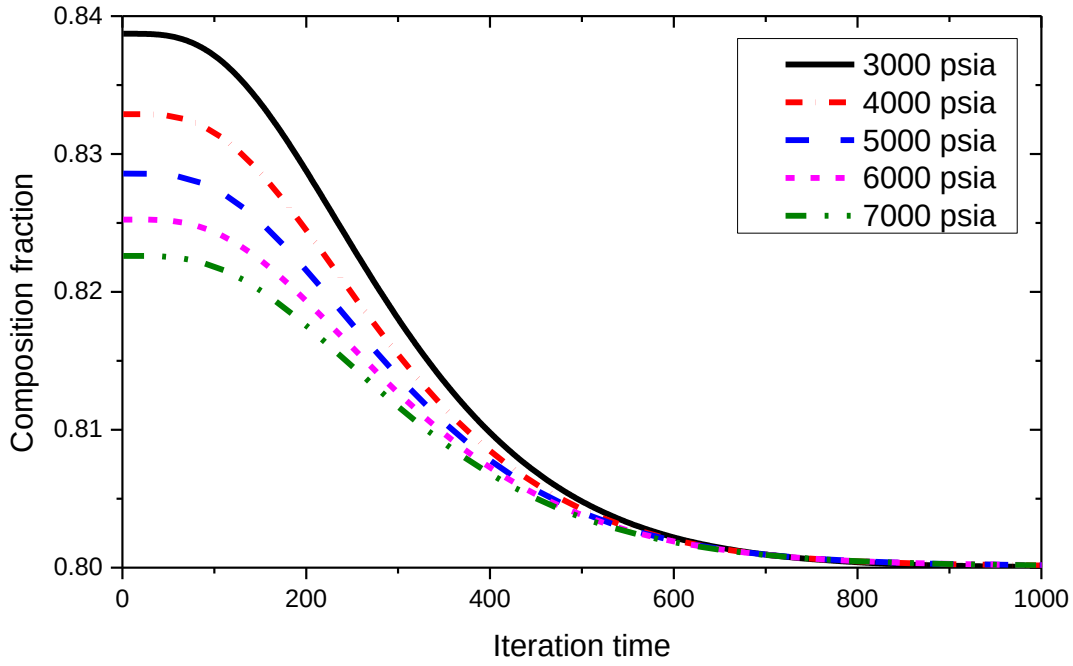

Figure 33. Flowing composition with various initial pressure conditions (C1)

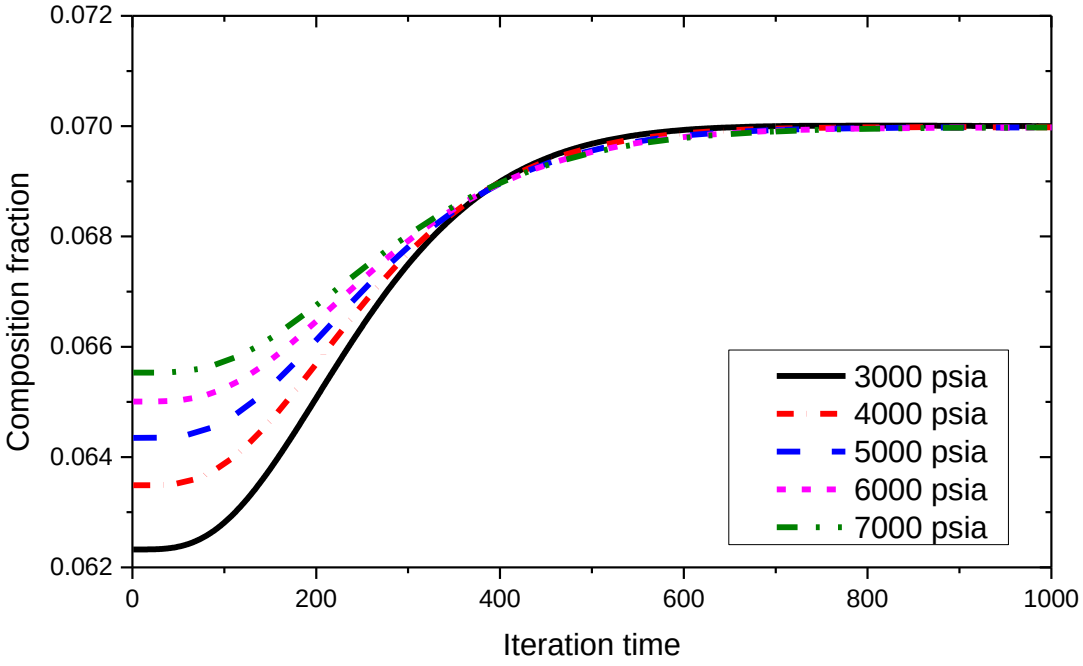

Figure 34. Flowing composition with various initial pressure conditions (C2)

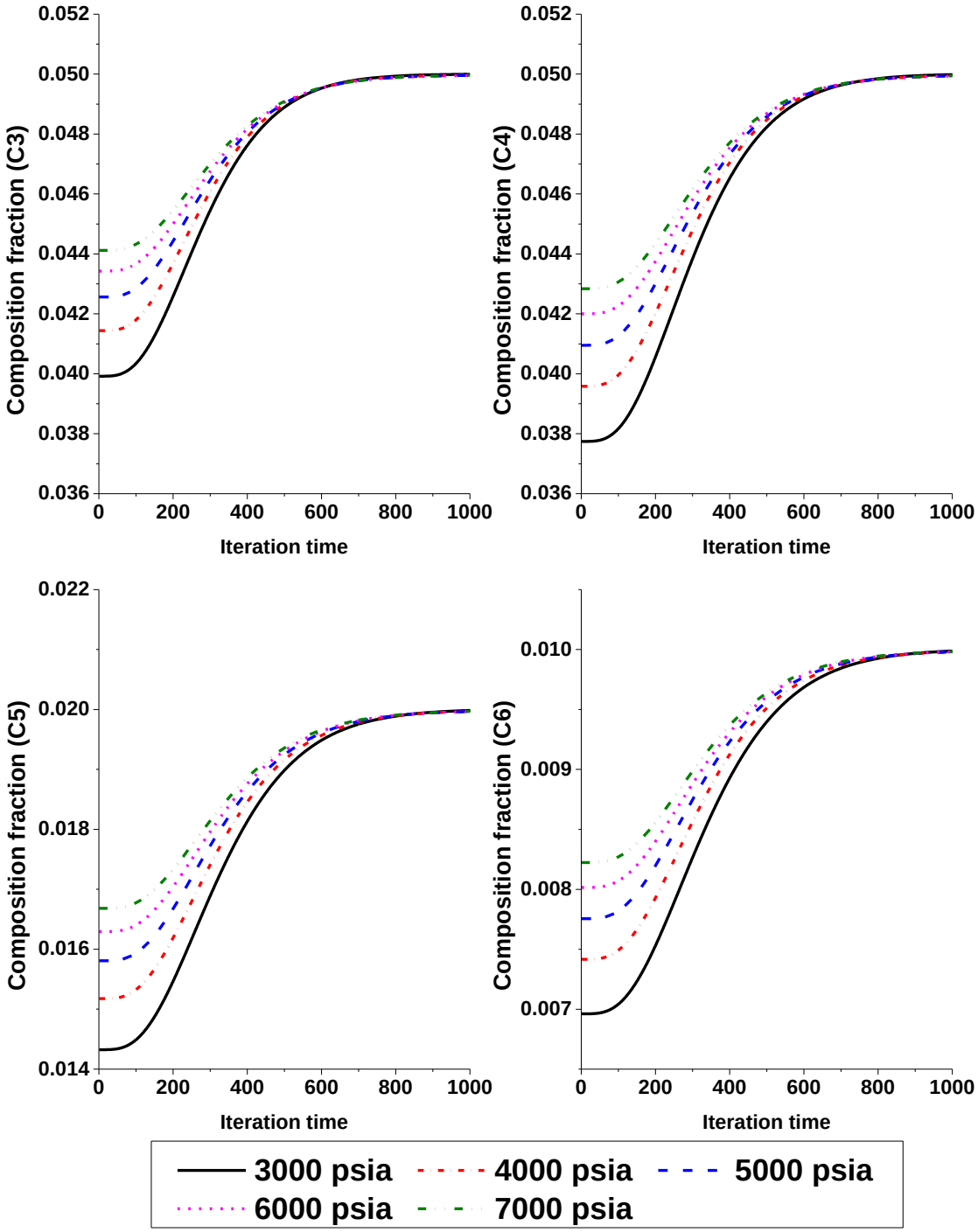

Figure 35. Flowing composition with various initial pressure conditions (C3 to C6)

Chapter 4. Reservoir Modeling of Multicomponent Flow

In Chapter 3, I investigated the role of Knudsen diffusion on the composition of the produced fluids using a simple case study on a synthetic fluid. The key conclusions from the chapter were that multicomponent Knudsen diffusion will result in in-situ fractionation because of the different velocities of the individual species. The conclusions from the study were valid for pressures above and below the saturation pressure of the gas. One missing element in Chapter 3 is the role of multicomponent adsorption in governing fluid phase compositions and that is beyond the scope of this study. In this chapter, I extend the same concepts to reservoir scale modeling and 2-phase flow using a numerical reservoir simulation approach.

In this case study, I assume a single pore size for the entire reservoir. Connectivity in shales is poorly understood (Curtis et al. 2010); however, if the pore connectivity resembles Figure 36a where all pores are arranged in parallel then the discussion presented in this thesis will be valid only for the largest pores that contain the highest percentage of the pore volume. For the largest of pores, the effect of Knudsen diffusion and slip flow is not significant. However, if the larger pores feed through smaller pores/pore throats as seen in Figure 36b, then the smallest pore throats control transport and the discussion presented in this thesis is valid across all pressure ranges irrespective of the pore volume contribution of the smallest pores.

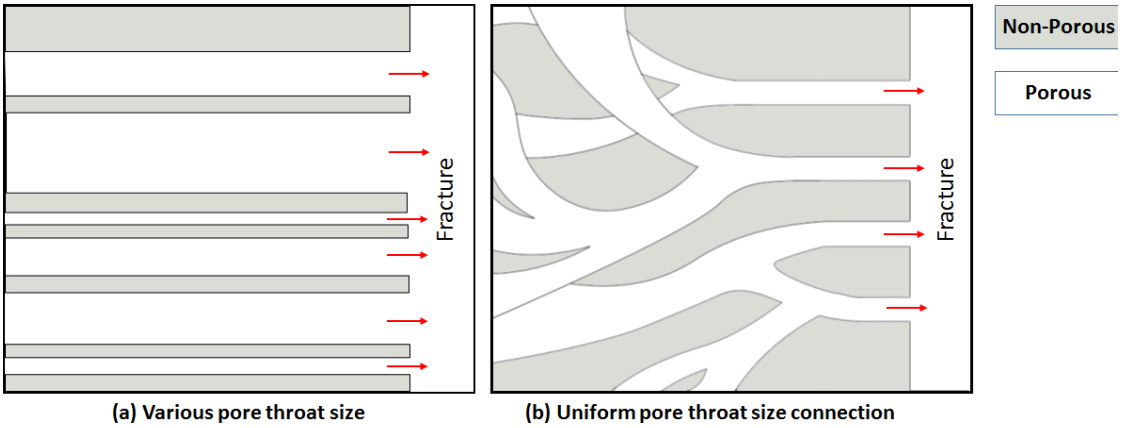

Figure 36. Pore connectivity scheme

4.1. Modeling of Multicomponent Gas Flow in a Reservoir Simulator

The Knudsen diffusion can be modeled using multicomponent diffusion and Klinkenberg keywords in numerical reservoir simulator (Reinecke and Sleep, 2002). The following sections provide an overview of these capabilities specifically using CMG-GEM (CMG, 2015).

4.1.1. Langmuir Adsorption

Multicomponent adsorption in numerical reservoir simulators is modeled using the extended Langmuir isotherm given by Equation 34 that specifies ω_i or the moles of component 'i' per mass of the rock (Arri et al., 1992 and Hall et al., 1994). The keywords used in this study are provided in Table 8.

$$\omega_i = \frac{\omega_{i,max} B_i y_{ig} P}{1 + P \sum_j (B_j y_{jg})} \tag{34}$$

where, B_i : Parameter for Langmuir isotherm relation

ω_i : Moles of adsorbed component per unit mass of rock

P : Pressure

y_{ig}: Molar fraction of adsorbed component i in the gas phase

$y_{ig}P$: Partial pressure of component i in the gas phase

Table 8. Langmuir adsorption keywords in CMG GEM

Method	Keywords	Details
Arri et al., 1992 Hall et al., 1994	*ADGCSTC *ADACSTC	Inverse mole fraction parameter (1/psi), B_i
	*ADGMAXC *ADAMAXC	Maximum moles of adsorbed component per unit mass of rock (kg/lb), $\omega_{i,max}$
From Lab data (Table input)	*ADSTAB *ADSTABA	ω_i at partial pressure versus each components (Table array)
	*ADSORBTMAX *ADSORBTMAXA	$\omega_{i,max}$ value of each components (Table array)
Multiplier	*LANGMULT	Multiplier for Maximum value of the Langmuir adsorption

Although there is very limited information regarding multicomponent adsorption in organic oil-wet nanopores, there is some evidence to suggest that the heavier components adsorb more easily in comparison to the lighter components (Welch and Piri, 2015). In this study I use similar trends to account for the adsorption of individual hydrocarbon species in a multicomponent gas mixture.

4.1.2. Diffusion Keywords

Commercially available numerical simulators also account for different forms of diffusion through the oil, gas, and aqueous phases works for mass transport from matrix to matrix, fracture to fracture and matrix to fracture blocks. The keywords used in this study are provided in Table 9.

Table 9. Diffusion keywords in CMG GEM

Keywords	Phases	Details
*DIFFUSION	Gas phase	Diffusion coefficients in Fractured reservoir (Matrix to Fracture)
*DIFCOR-OIL *DIFCOR-GAS	Oil phase Gas phase	Select Molecular diffusion correlation type
*DIFFC-OIL *DIFFC-GAS *DIFFC-AQU	Oil phase Gas phase Aqueous phase	Molecular diffusion coefficients (Diffusion rate)

4.1.3. Non-Darcy Gas Flow Keywords

Table 10. Non-Darcy flow keywords in CMG-GEM

Keywords	Details
*NONDARCY	Select correlations for gas phase non-Darcy flow · Geertsma's (1974) · Frederick and Graves (1994) 1st and 2nd correlation · Table input (β [1/ft], α_g)
*KLINKENBERG	Reference pressure for the Klinkenberg effect (psi)

*NONDARCY keyword is related to the Forchheimer coefficient for high velocity gas flows. The *KLINKENBERG keyword modifies the effective gas permeability as a function of pressure as shown in Equation 35.

$$k_{g,eff} = k_{liquid}(1 + (P_{Klinkenberg}/P)) \quad (35)$$

where, k_{liquid} : Liquid permeability at infinite pressure

$P_{Klinkenberg}$: Reference pressure for Klinkenberg effect

P : Reservoir pressure

In this work, I do not account for Forchheimer non-Darcy flow effects.

4.2. Reservoir Simulation Model

Figure 37 is an example of field production data showing very stable and constant GOR trends over an extended period of time for a gas-condensate well in the Eagleford (Data source confidential). Because a stable GOR (or CGR trend) is not the norm for wells producing from conventional reservoirs, the central theme of this chapter is to investigate the reasons behind this phenomenon for shale wells using the concepts of Knudsen diffusion as outlined earlier in Chapter 2 and demonstrated in Chapter 3.

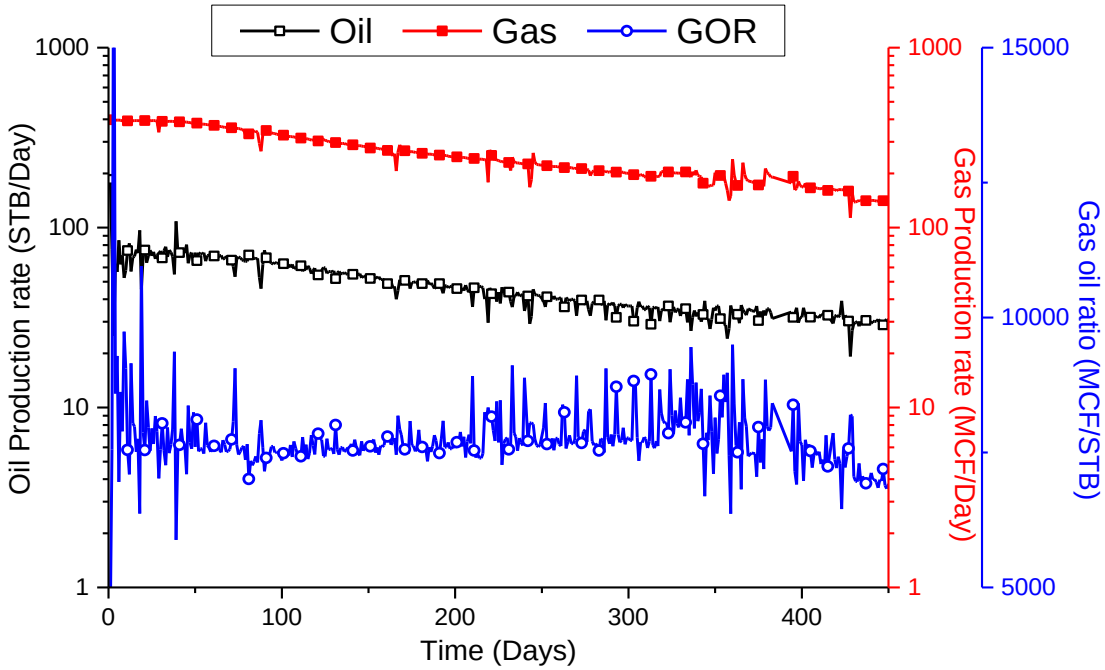

Figure 37. Reference real field production data (Confidential)

4.2.1. Grid Properties

General reservoir properties used for the reservoir simulation are summarized in Table 11 for a horizontal well intersected by a single bi-wing hydraulic fracture. Figure 38 shows a schematic of the reservoir simulation model used in this modeling study.

Table 11. Reservoir properties

Properties	Value
Reservoir depth (Top), ft	13,000
Initial reservoir temperature, °F	200
Initial reservoir pressure, psia	5,000
Average porosity	5%
Average water saturation (Matrix)	25%
Natural Fracture Permeability, md	1e-4
Matrix Permeability, md	1e-7
Hydraulic Fracture Permeability, md	100
Hydraulic Fracture length, ft (long-axis)	500
Model size (I*J*K), ft	2,800*1,300*150

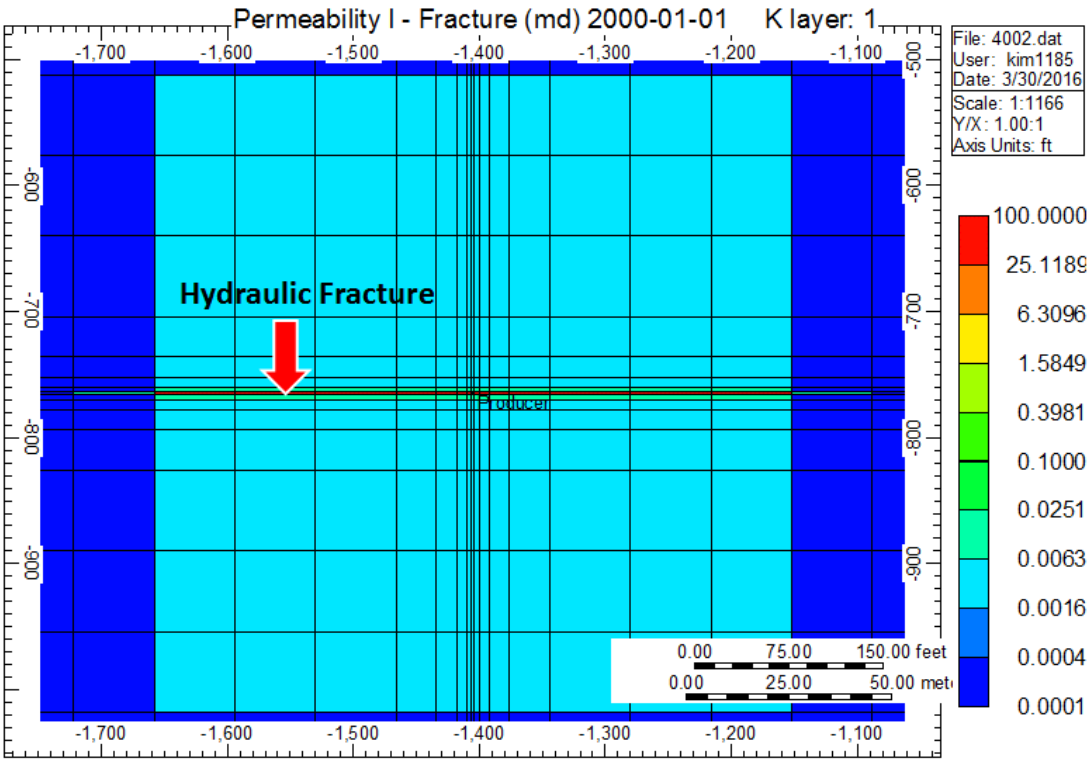

Figure 38. The stimulated reservoir volume showing the location of the hydraulic fracture.

The reservoir model is defined on a grid that is specified to be 2,800 ft x 1,300 ft x 150 ft (I-J-K direction). The hydraulic fracture has a permeability of 100 md and is shown in Figure 38. An idealized reactivated natural fracture network where the permeability progressively decreases from a high value near the main bi-wing fracture to a value higher than $2.5e^{-3}$ md farther away and this stimulated volume is shown in blue in Figure 39. Outside of this region, the natural fractures are considered sealed and have a lower permeability.

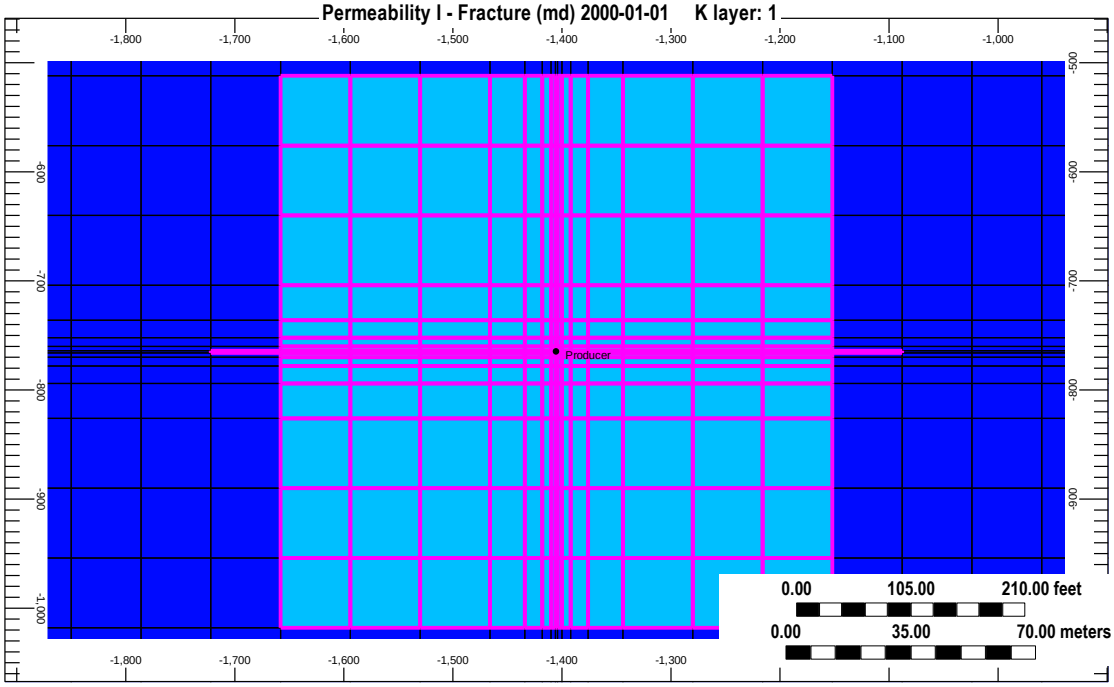

Figure 39. Stimulated reservoir volume with re-activated natural fractures.

4.2.2. Rock & Fluid Properties

For the reservoir simulation case study, I use a 12-component fluid whose composition is shown below in Table 12 and its phase diagram is shown in Figure 40. At 200 °F, the fluid is a gas-condensate with a dew point of 3,371 psia.

Table 12. Fluid composition (12 components, percent) used for reservoir simulation

CH4	C2H6	C3H8	IC4	NC4	IC5	NC5	FC6	FC7	FC8	FC9	FC10
70	11	5	2	2	1	1	1	1	1	1	4

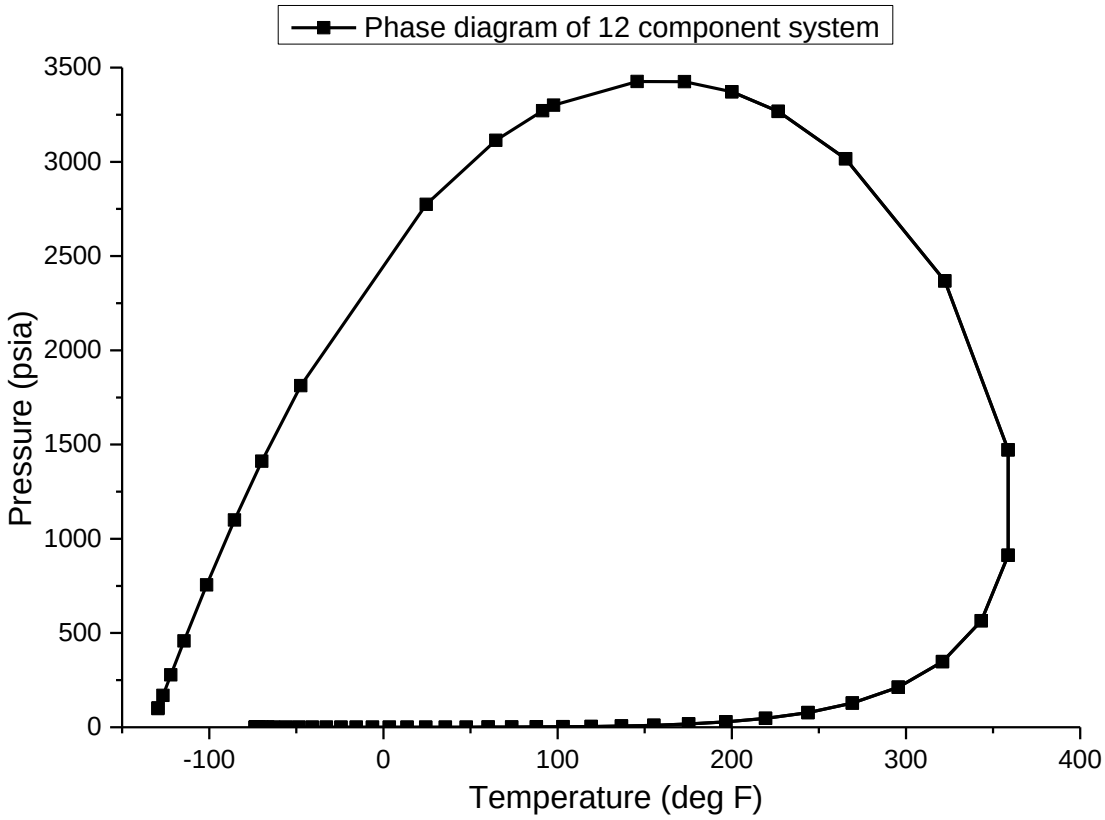

Figure 40. Phase diagram with 12 components

I used Stone's second model shown in Equation 36 and Equation 37 for the three-phase relative permeability as shown in Figure 41 and Figure 42

$$K_{rw} = K_{rwco}\left[\left(\left(\frac{K_{rwo}}{K_{rwco}}\right) + K_{ro}\right)\left(\left(\frac{K_{rwg}}{K_{rwco}}\right) + K_{rg}\right) - K_{ro} - K_{rg}\right] \quad (36)$$

$$K_{ro} = K_{rocw}\left[\left(\left(\frac{K_{row}}{K_{rocw}}\right) + K_{rw}\right)\left(\left(\frac{K_{rog}}{K_{rocw}}\right) + K_{rg}\right) - K_{rw} - K_{rg}\right] \quad (37)$$

where, K_{rwco} : water relative permeability at connate oil

K_{rwo} : water relative permeability with water-oil two phase condition

K_{rwg} : water relative permeability with water-gas two phase condition

K_{rocw} : oil relative permeability at critical water saturation

K_{row} : oil relative permeability with oil-water two phase condition

K_{rog} : oil relative permeability with oil-gas two phase condition

Initial water saturation at the matrix was set as 0.25 and zero for the initial water saturation in the fracture. Other values were assumed.

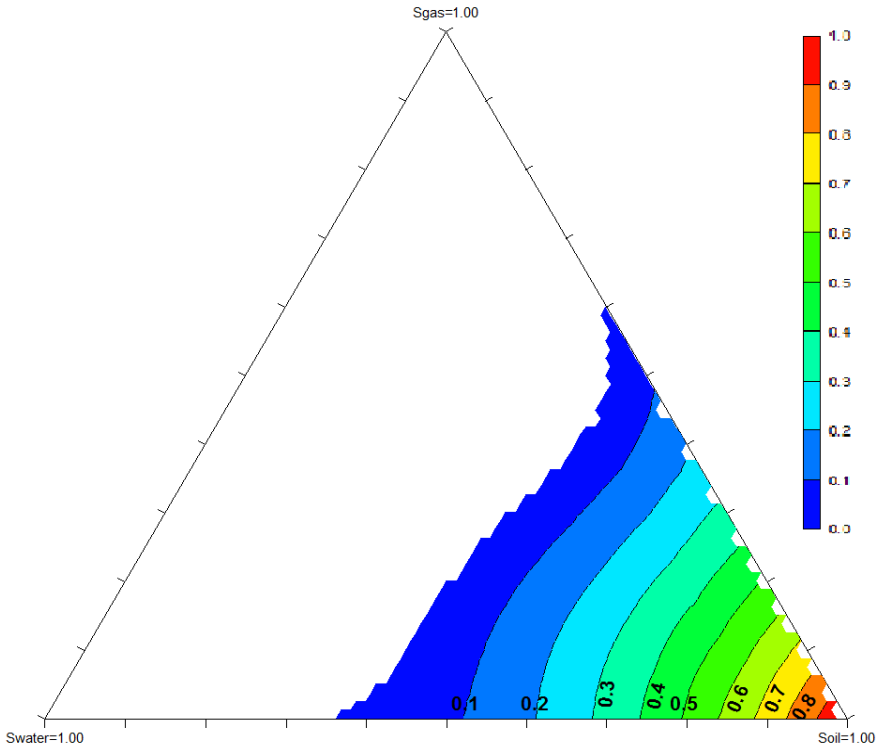

Figure 41. Three phase relative oil permeability (Matrix)

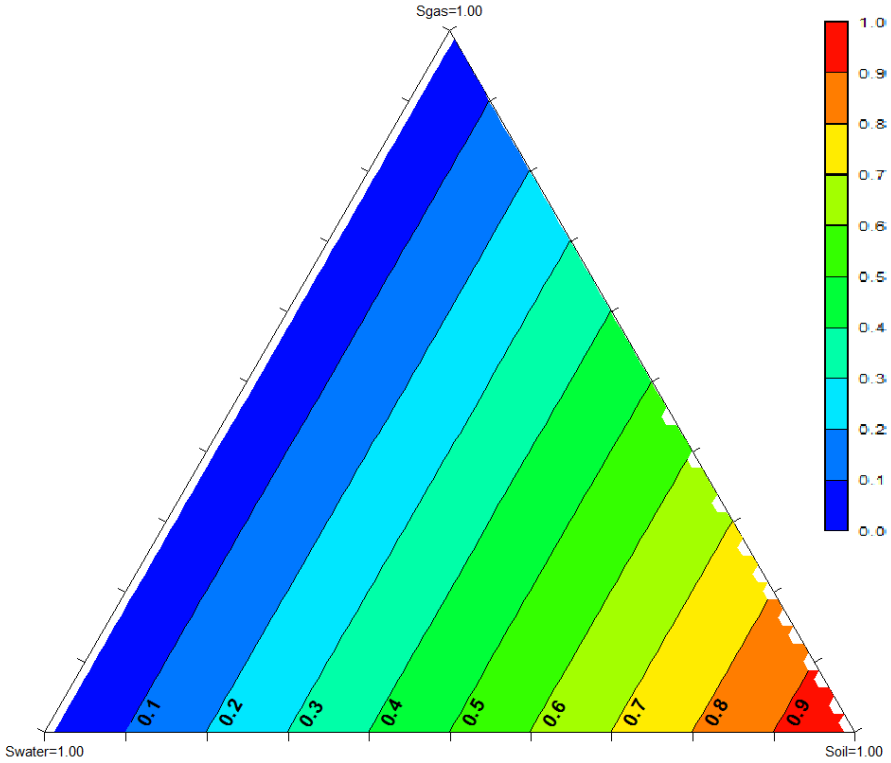

Figure 42. Three phase relative oil permeability (Fracture)

4.2.3. Diffusion Coefficients

Diffusion coefficients used for the case study were calculated based on the study by Kim et al. (2016) that reports the Knudsen diffusion coefficient for C1 as 0.02086 cm^2/s in a 5 nm radius pore. In our case study, the reservoir is assumed to have a 5nm pore size and diffusion coefficient of C1 as 0.02 cm^2/s. The different hydrocarbon species are grouped into 4 as shown in Table 13.

Table 13. Grouped components

Group #	Components
1	C1
2	C2, C3
3	IC4, NC4, IC5, NC5, FC6
4	FC7, FC8, FC9, FC10

The diffusion coefficient of each group was estimated by scaling the diffusion coefficient of C1 from the Kim et al. (2016) study with the average molecular weight of each group using the relationship shown below (Mason and Malinauskas, 1983).

$$D_{K,A} = \frac{d_P}{3}\sqrt{\frac{8RT}{\pi M}} \tag{18}$$

Therefore diffusion coefficient of C1 was set as:

1. DIFFC-GAS (C1 : $2e^{-2}$ cm^2/s), which represents the diffusion coefficient of the gas phase between matrix-matrix and fracture-fracture.
2. DIFFUSION (C1 : $2e^{-2}cm^2/s$) works for matrix-fracture diffusion coefficients for the gas phase.

3. DIFFC-OIL (C1 : $2e^{-4}$ cm^2/s) is diffusion of each component in the oil phase which is assumed to be 100 times lesser than DIFFC-GAS.

Langmuir adsorption and Klinkenberg effect were not modelled in this case study.

4.2.4. Base Case Simulation Result

The well in the simulation model described earlier is operated at a constant bottomhole pressure of 1,000 psia. Figure 43 shows the GOR as a function of time and Figure 44 shows the average oil and gas saturations within the fracture system as a function of time. The fracture system consists of 2 parts: the main hydraulic fracture with a permeability of 100 md as well as the re-activated natural fracture system with a lower permeability. The GOR trends in Figure 43 show relatively stable values for an extended period of time; however when liquid dropout becomes appreciable in the matrix (in the vicinity of 4,000 days), the GOR shows a small jump to a slightly lower value.

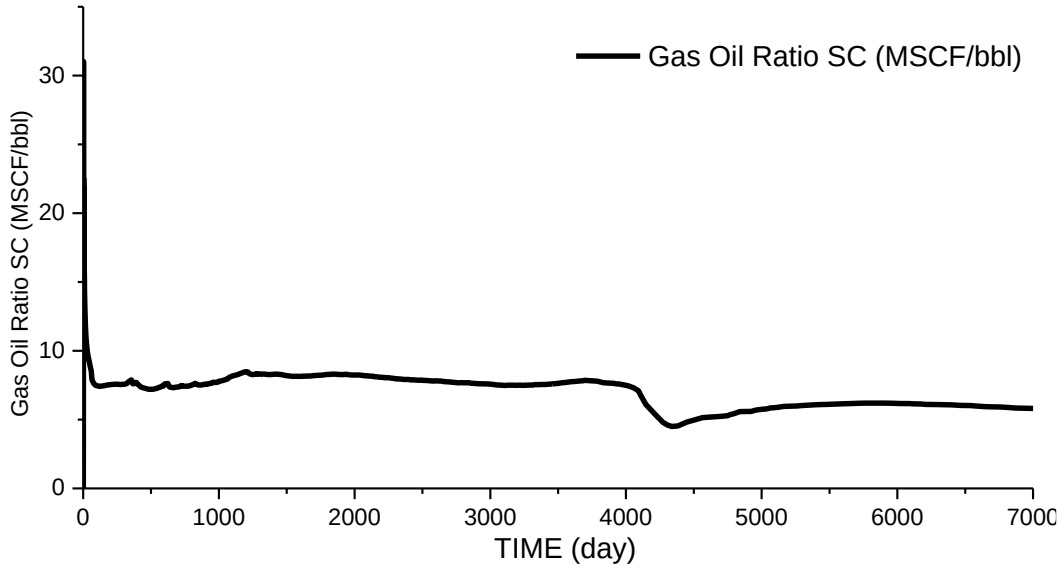

Figure 43. Simulation result – GOR (Base case)

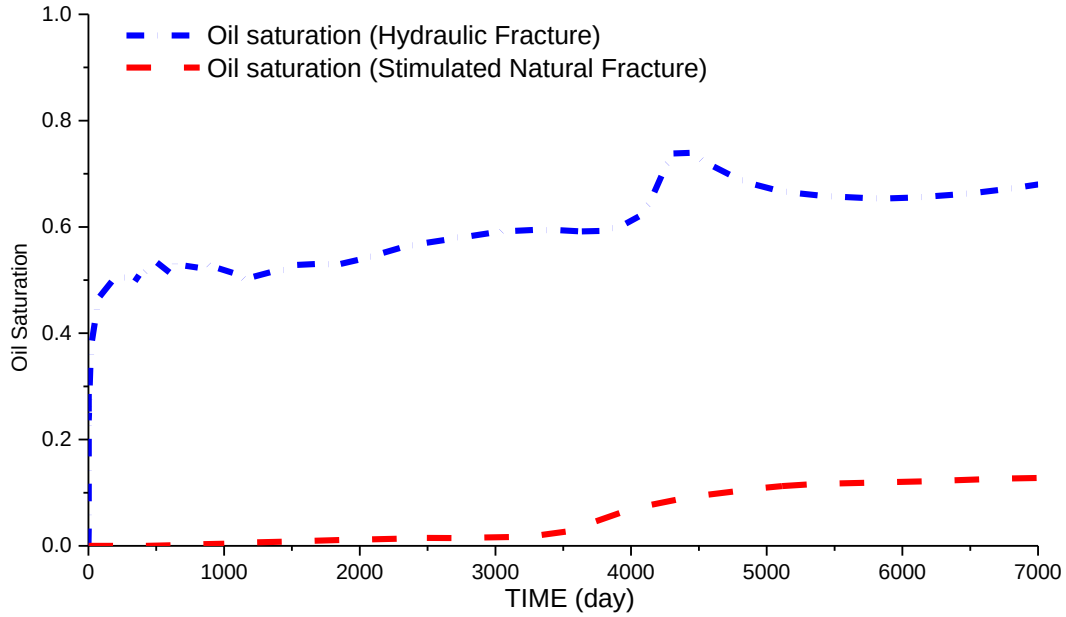

Figure 44. Simulation result – Oil saturation (Base case)

Production for this case study can be analyzed in three different stages corresponding to flow from the key corresponding elements of the completions and the reservoir.

1. Production from the major hydraulic fracture area
2. Production from the stimulated reservoir volume (SRV)
3. Production from the matrix system with accompanying liquid drop out near the stimulated reservoir volume (SRV) boundary.

4.2.4.1. Stage 1 (Start ~ 150 days)

During stage 1, most of the hydrocarbons are produced from the hydraulic fracture volume and adjacent fractures. The GOR shows a rapid response to the low BHP and rapidly climbs because gas flows faster than the liquid phase.

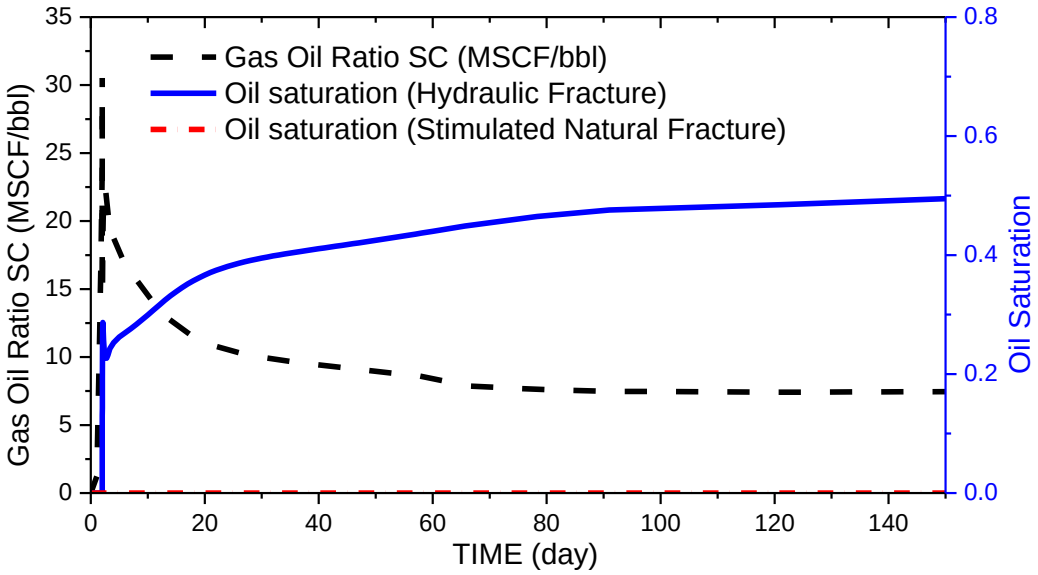

Figure 45. Production trends for the initial 150 days.

A period of relatively flat GOR follows because of a combination of flow from the stimulated natural fractures as well as the hydraulic fracture. Figure 46 shows oil saturation in fracture system.

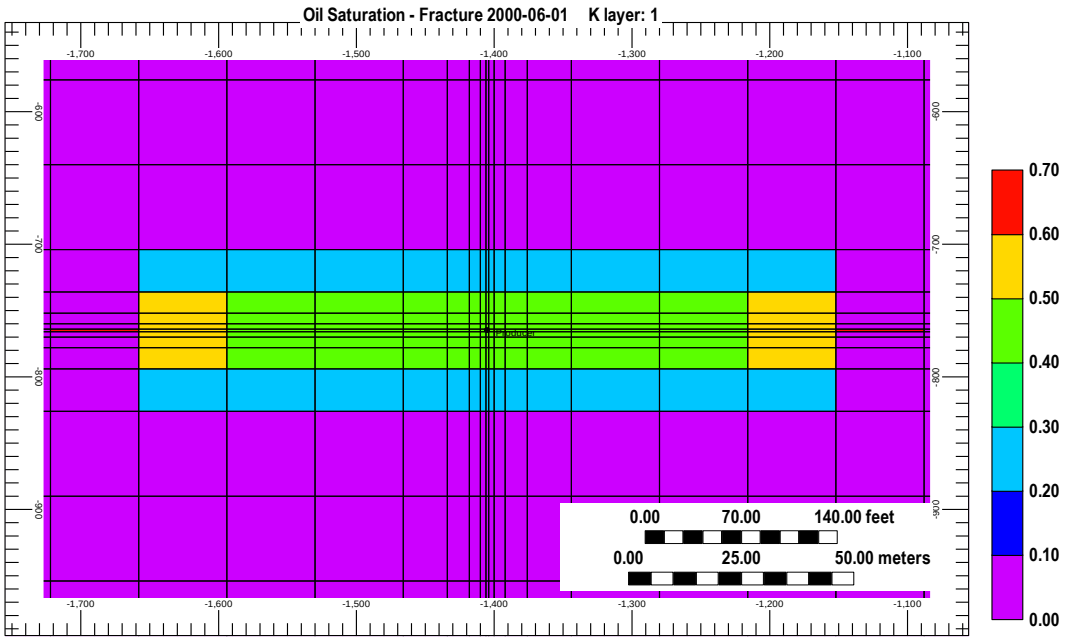

Figure 46. Oil saturation in the fracture system after 5 months.

4.2.4.2. Stage 2 (150 days ~ 10 years)

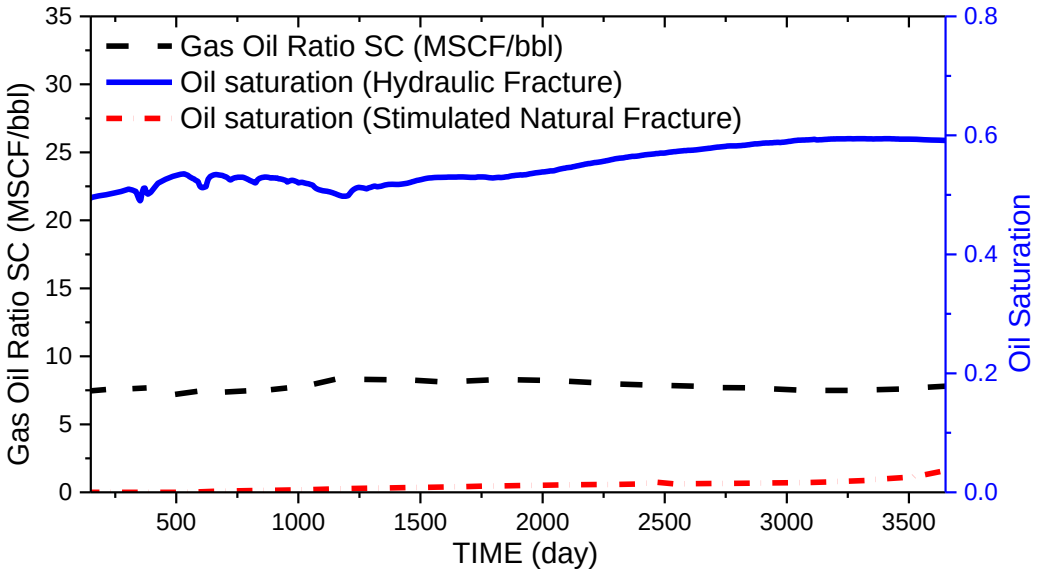

Figure 47. Production trends from 150 days to 10 years of production.

The second stage is identified by the relatively constant GOR trends as shown in Figure 47. Production during this period is primarily from the stimulated volume surrounding the hydraulic fracture and is primarily driven by the Knudsen diffusion of each component as well as some contribution from viscous flow of the oil phase. The GOR remains a constant during this time because although the pressure in the SRV is lower than the fluid saturation pressure, there is no appreciable condensate dropout within the matrix. This is a key outcome of the work presented in this thesis.

In typical gas condensate wells, as the pressure in the wellbore drops below the dew-point pressure of the gas condensate, liquid dropout begins in the vicinity of the wellbore. This condensate ring then rapidly grows and leads to a rapid increase in GOR values as the heavier components condense within the near-wellbore volumes. In this case study, although there is some liquid dropout in the vicinity of the fractures, this region does not grow appreciably over a period of 10 years. The relatively constant

GOR profile and the lack of appreciable condensate dropout can be explained by considering the two competing phenomena occurring within the matrix system and the adjacent fractures. Although the pressure transient is propagating outward from the wellbore and liquid dropout is expected, simultaneously there is the corresponding competitive diffusion of the lighter components (faster) and heavier components (slower) towards the main hydraulic fracture. Consequently, although two-phase flow in the matrix is to be expected with pressures below the dew-point, the faster diffusion of the lighter components towards the wellbore keeps the fluid composition relatively stable and may even re-evaporate some of the heavier condensed hydrocarbons.

Stage 2 of productive well life continues until the pressure transient reaches the boundary of stimulated area. At this point in time, the pressure transients reach a low conductivity, unstimulated fracture system and therefore transport of both oil and gas in to the SRV is reduced. This leads to a build-up of liquid at the boundaries of the SRV as shown in Figure 48.

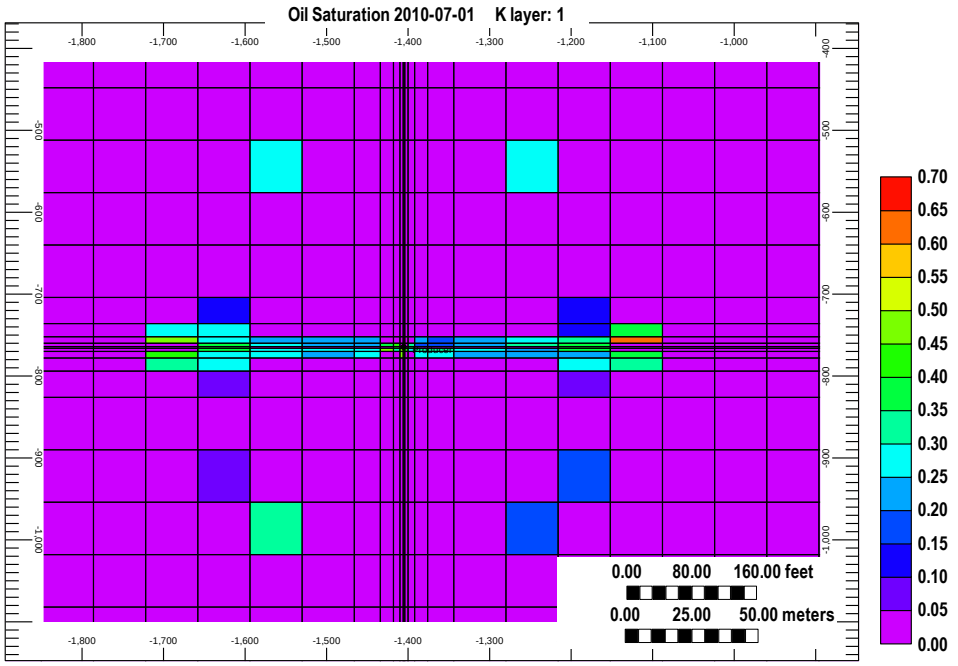

Figure 48. Oil saturation in the matrix after 10 years production

4.2.4.3. Stage 3 (After 10 years)

Once the pressure transient reaches the boundary of the SRV, the flow rates from the unstimulated area remains limited. At this time, liquid dropout in the vicinity of the boundary becomes appreciable and additionally diffusion of the components in the oil phase also becomes appreciable. There is therefore a marginal increase in the oil saturation in the matrix at the boundary of the SRV as shown in Figure 49 and Figure 50.

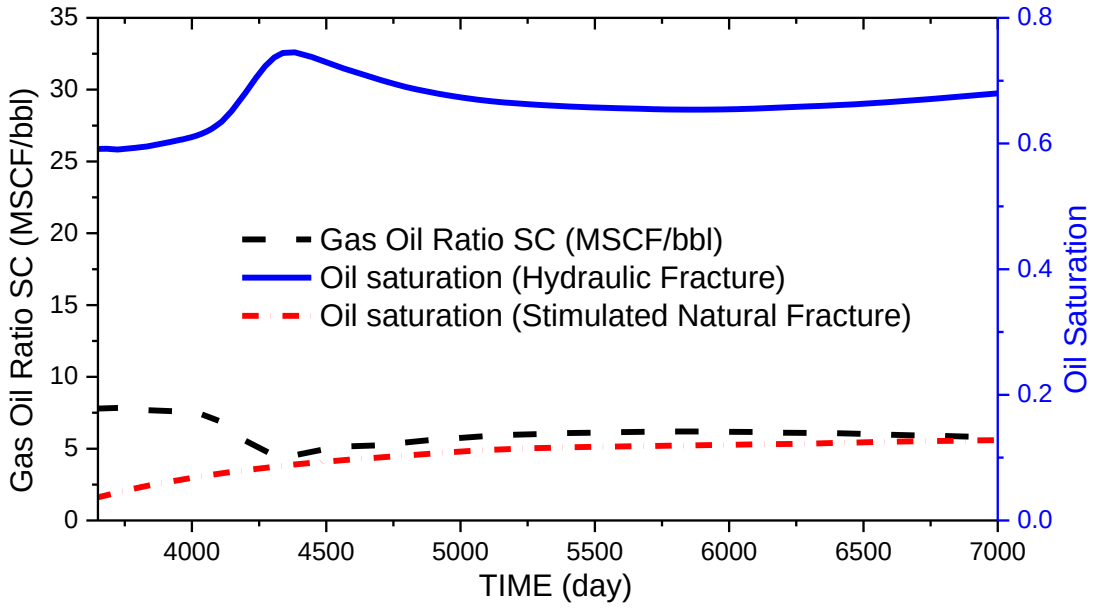

Figure 49. Production results of the Stage 3

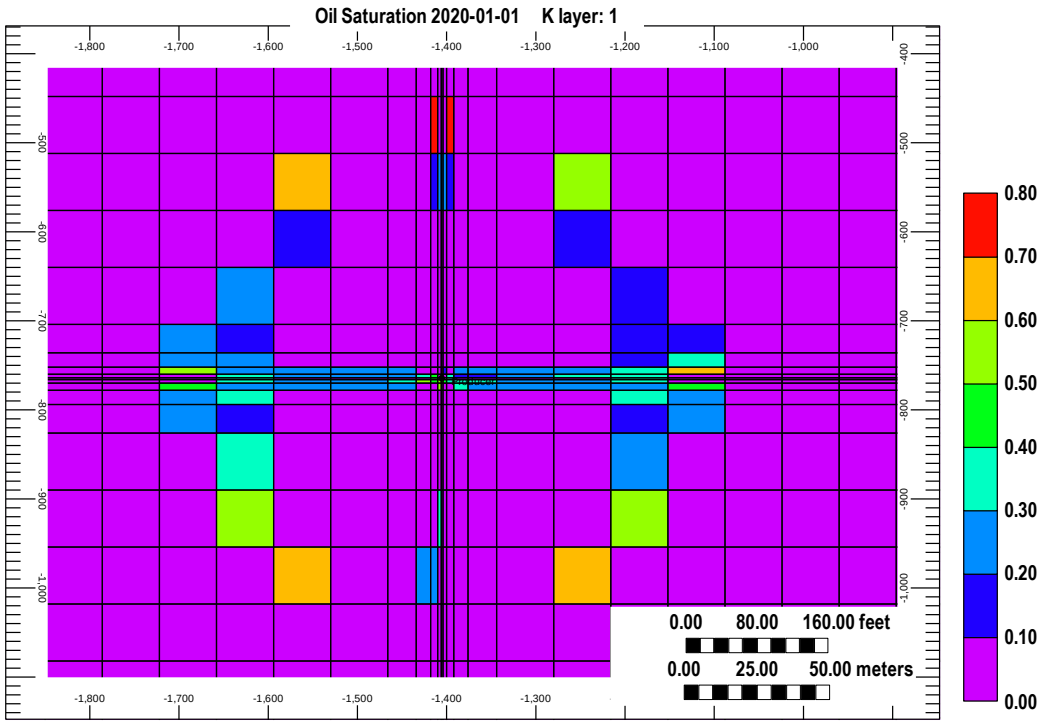

Figure 50. Oil saturation in matrix after 20 years of the production

Figure 51 shows the pressure distribution in the matrix and the fracture systems as a function of time. The pressure distribution in the matrix is shown on the left while the pressure distribution in the fracture systems is shown on the right. It becomes apparent that the primary contribution to the initial flow is from the fracture systems and eventually grows to include the matrix within the SRV. Finally, after the SRV boundary is reached, there is very limited growth in the drainage volume beyond the SRV.

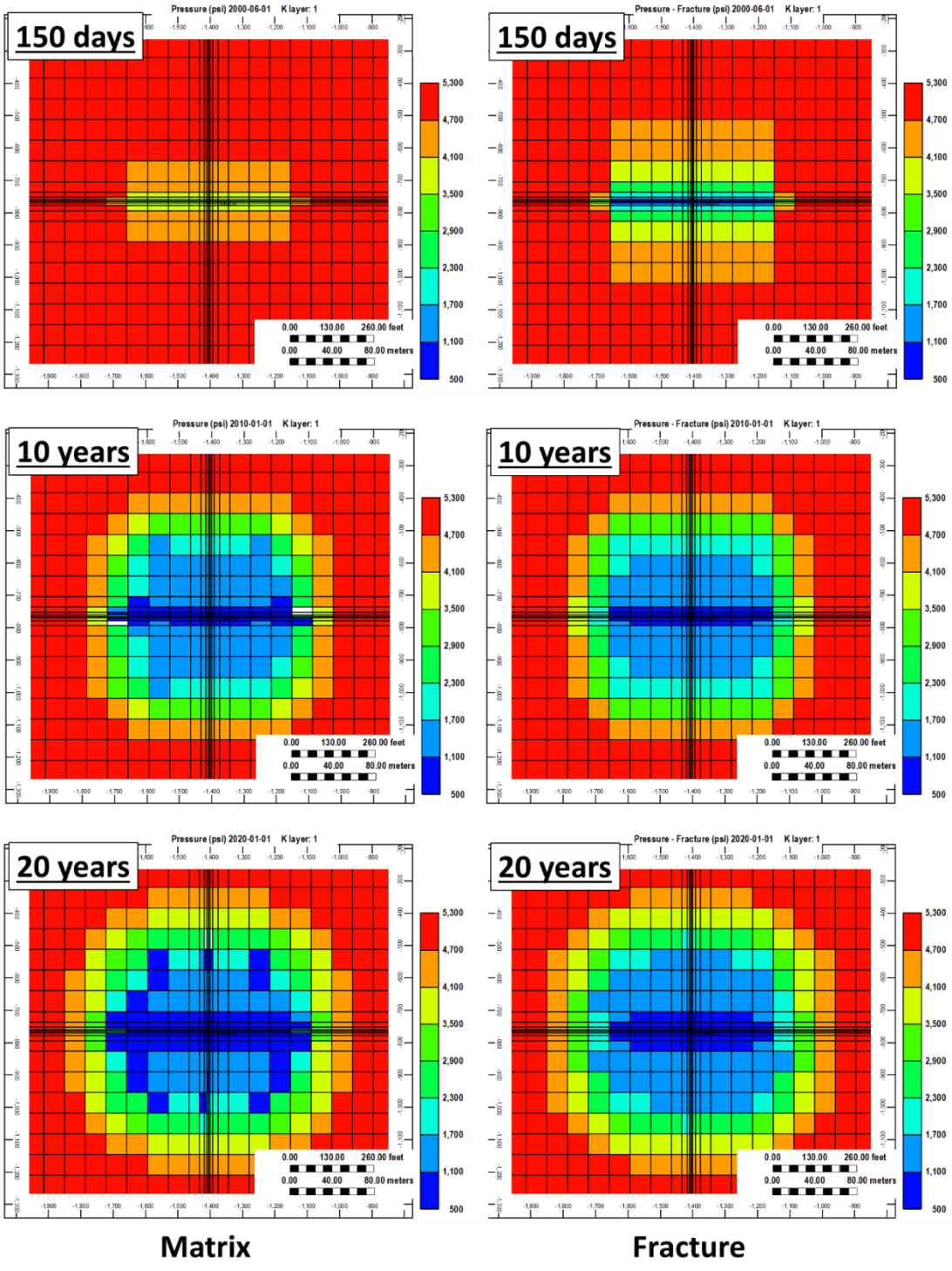

Figure 51. Pressure distribution in the matrix on the left and fracture system on the right with time

4.2.4.4. Composition Change with Time

Figure 52 to Figure 55 show the changes in the produced gas composition with time. C1 mole fractions increase up to 78% at the beginning of production and still remain higher at 74% than the in-situ fluid composition. The C2 mole fraction also increases to a value of 12% in comparison the original mole fraction of 11%. The mole fractions of the heavier components in the produced gas stream however remain lower than the corresponding values for the original reservoir fluid. In general however, following rapid initial changes, the compositions remain relatively stable. Most importantly, the produced fluid composition is lighter in comparison to the original fluid composition. I provided composition change ratio plot of below Figure 52 to Figure 55 compared with its original composition in Appendix B.

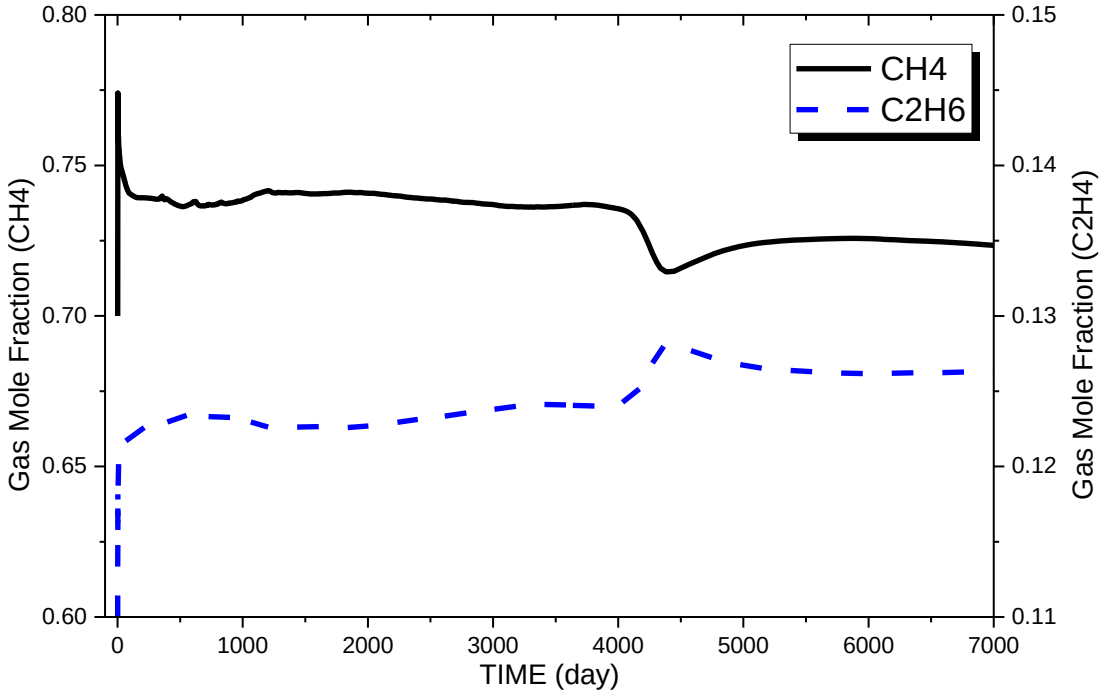

Figure 52. Produced gas composition change - C1, C2

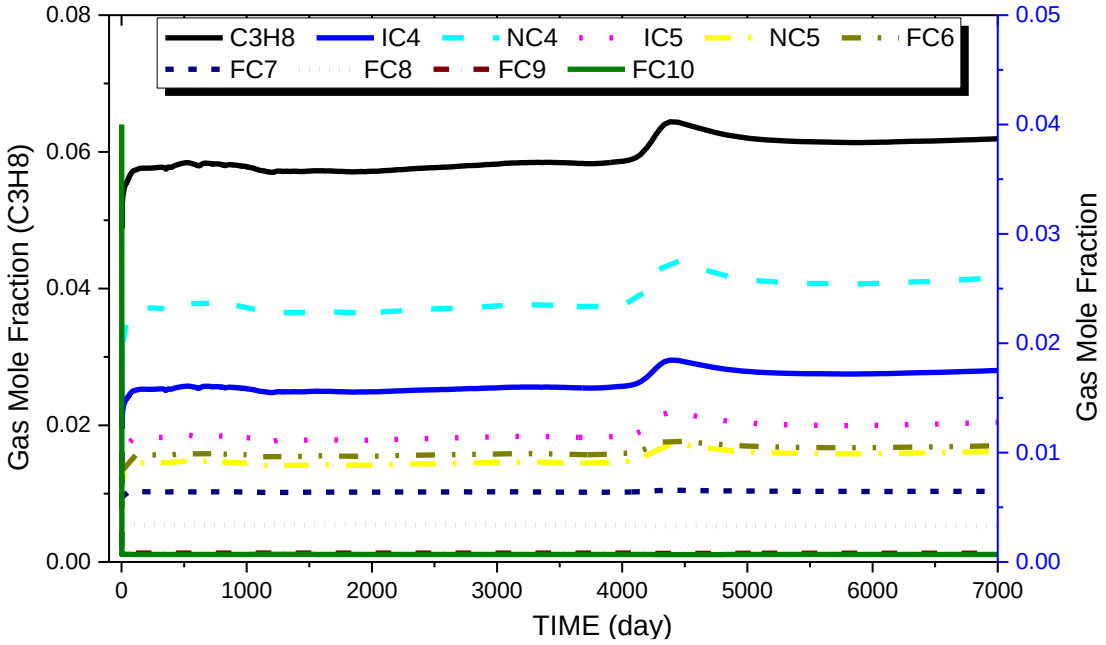

Figure 53. Produced gas composition change - C3 to FC10

The produced oil compositions are shown in Figure 54 and Figure 55 and also indicate relatively stable compositions over an extended period of time.

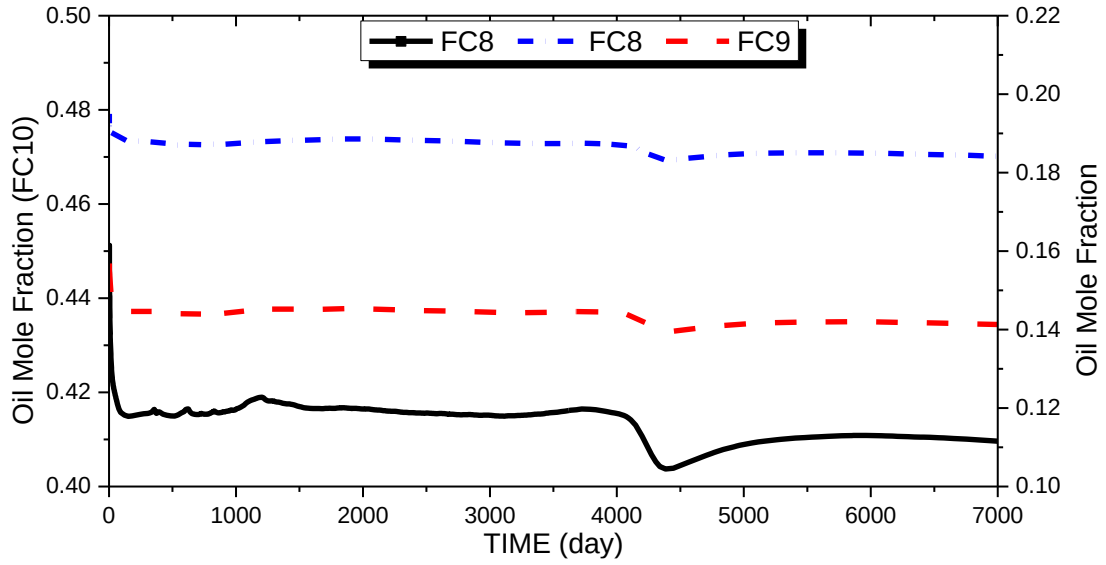

Figure 54. Produced oil composition change - FC8, FC9, and FC10

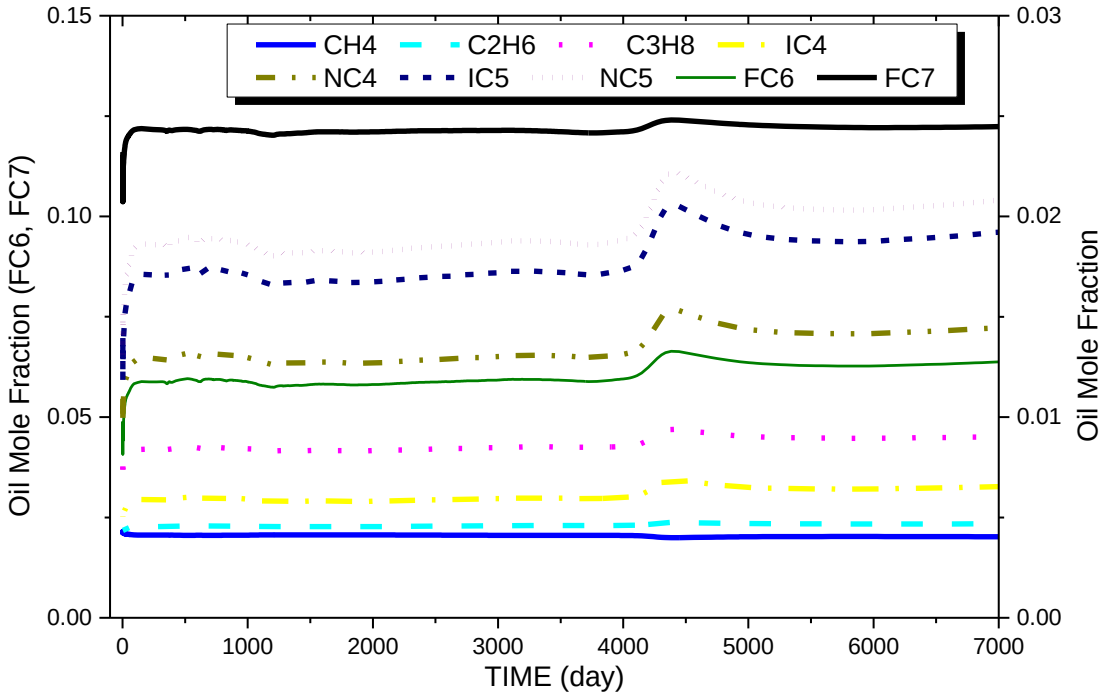

Figure 55. Produced oil composition change - C1 to FC7

4.2.5. Simulation Result without Any Diffusion Keywords

In the previous section, a simulation case study of a hydraulically fractured well was presented to illustrate the effects of multicomponent diffusion on produced fluid compositions as well as GOR or CGR trends. In this section, I discuss the effect of eliminating all diffusion keywords and only incorporating viscous flow governed by Darcy's equation. Figure 56 shows the GOR trends with time showing a marked increase from initial values. Figure 57 shows the average oil saturation in the hydraulic fracture system and the stimulated natural fracture region. The oil saturation rapidly climbs to a value of 0.2 because of liquid dropout. There is however no appreciable liquid dropout in the natural fracture system.

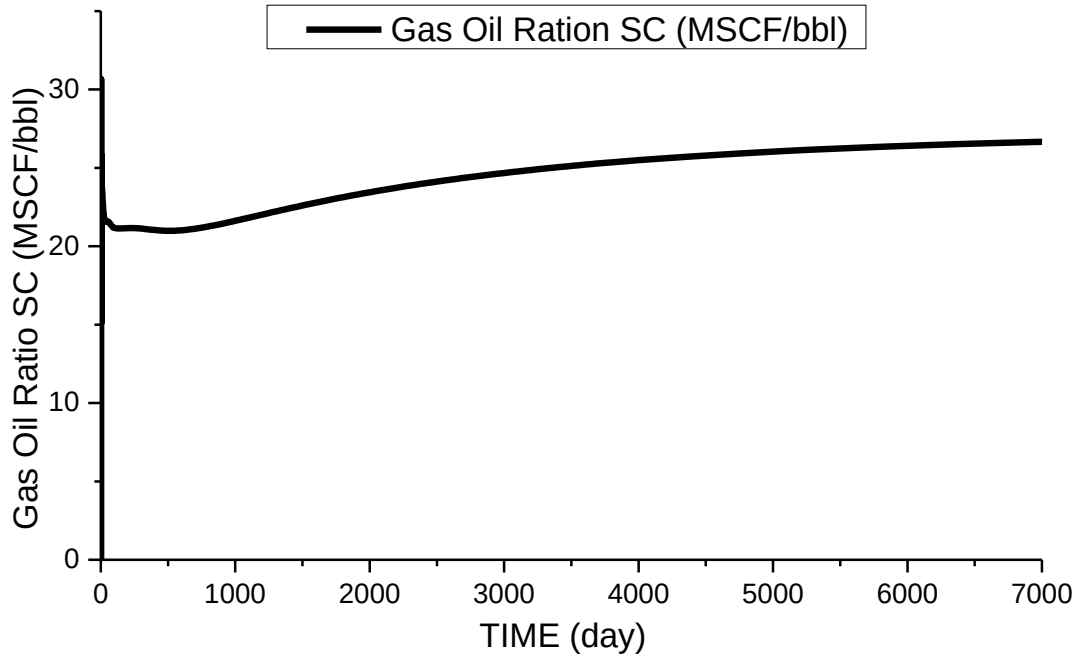

Figure 56. GOR trends with time

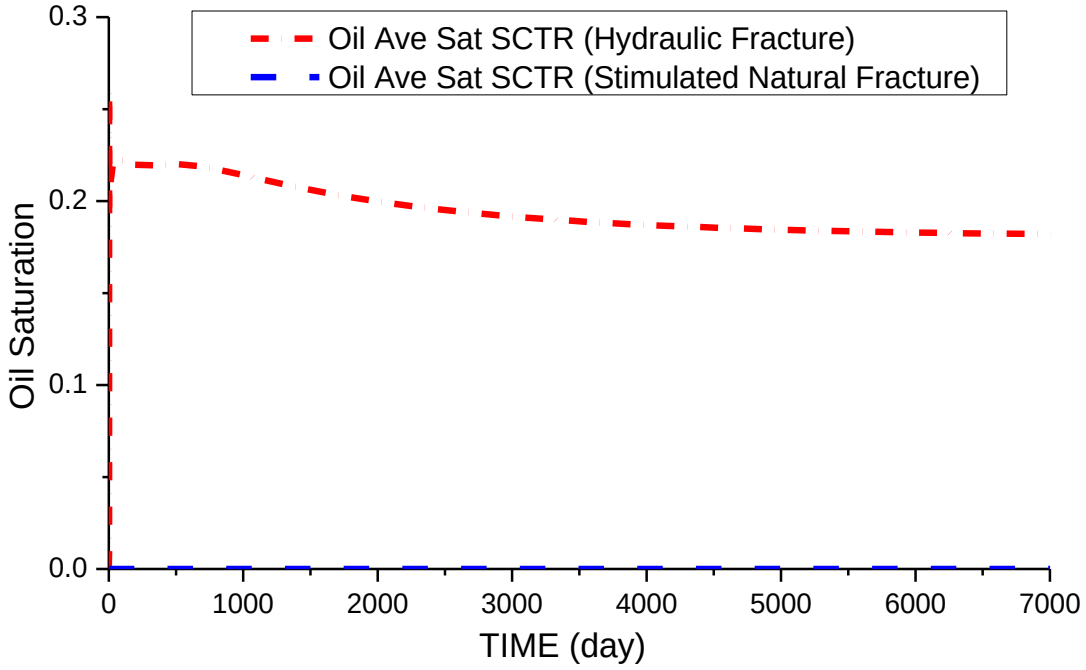

Figure 57. Average oil saturation of 100md fracture area and whole hydraulic fracture area

The most important observation from this study was the lack of pressure propagation within the matrix system even after an extended period of time. The pressure distribution in the matrix after 20 years of production shows most parts still near initial pressure except in the vicinity of the hydraulic fracture as shown in Figure 58. Consequently again liquid dropout in the matrix remains limited.

However at the same time, the fluid flow rates remain limited. It is important to note that without appreciable multicomponent diffusion, realistic oil and gas rates are not feasible in this idealized model unless the SRV is considerably larger than the model volume chosen in this case study. Additionally, without diffusion included, the GOR trends do not remain a constant. However because of a lack of pressure propagation in the matrix, the GOR does not increase substantially either.

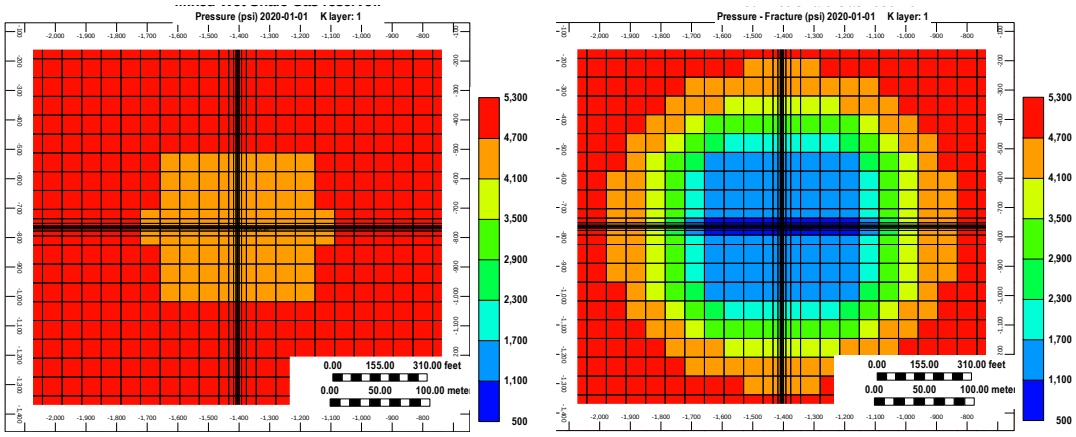

Figure 58. Pressure in the matrix on the left and the fracture on the right after 20 years of production. (There is very limited pressure propagation in the matrix.)

Chapter 5. Sensitivity Studies

In this chapter, I investigate the sensitivity of well and reservoir performance with respect to changes in the stimulated reservoir volume, the diffusion coefficients, the fracture permeability and the matrix permeability.

5.1. Stimulated Reservoir Volume

Table 14 provides the list of case studies considered when varying the width of the SRV. Figure 59 illustrates the width of the SRV extending from the vicinity of the hydraulic fracture. The permeability of all fracture cells in this SRV is assumed to be $2.5e^{-3}$ md.

Table 14. Cases for stimulated reservoir volume sensitivity study

Case #	SRV Width (ft)
Base case	496
Case 1	112
Case 2	240
Case 3	368
Case 4	624

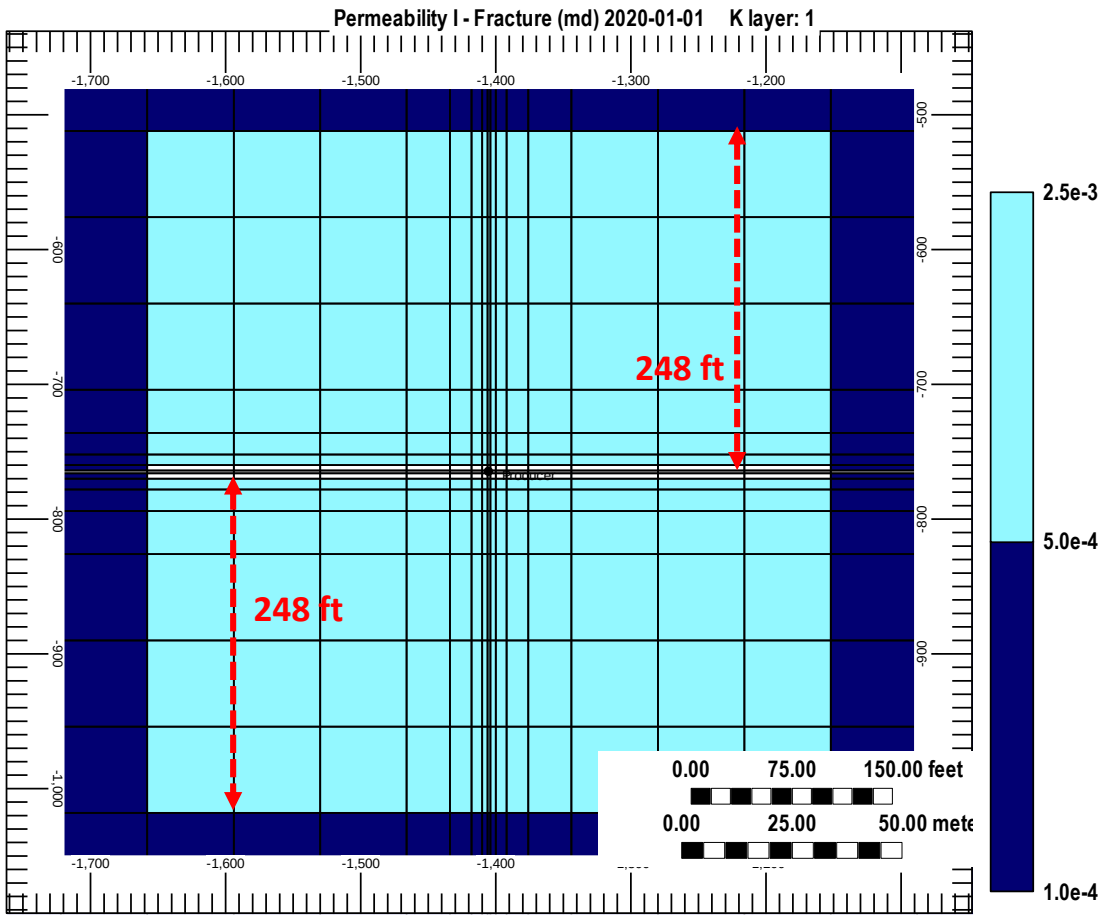

Figure 59. Stimulated reservoir volume width in the base case (light cyan, 248ft + 248ft)

The GOR profiles for each of the case studies is shown in Figure 60 for small stimulated volumes and in Figure 61 for larger stimulated volumes. In all of these cases, we observe a relatively flat GOR trend initially. However at later times, the GOR tends to decrease marginally in all case studies. This occurs when liquid dropout at the boundary of the SRV becomes appreciable and oil flow and diffusion through the oil phase becomes appreciable. However it is important to note that the overall GOR trend appears to be linked to the size of the SRV and when the pressure transients reach the boundary of the SRV.

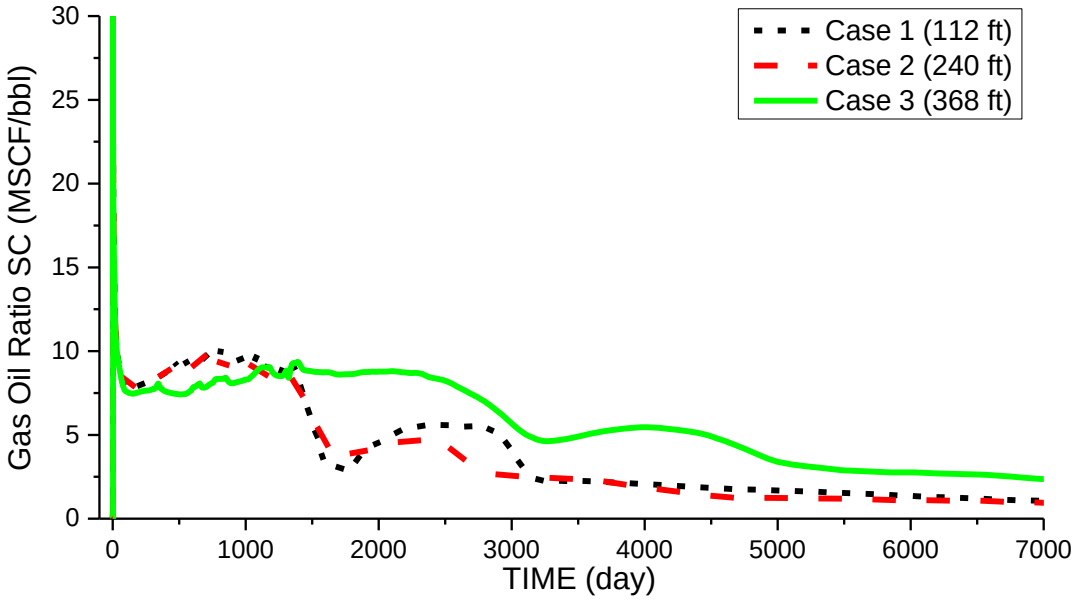

Figure 60. GOR trends as a function of the width of the SRV (Small SRV)

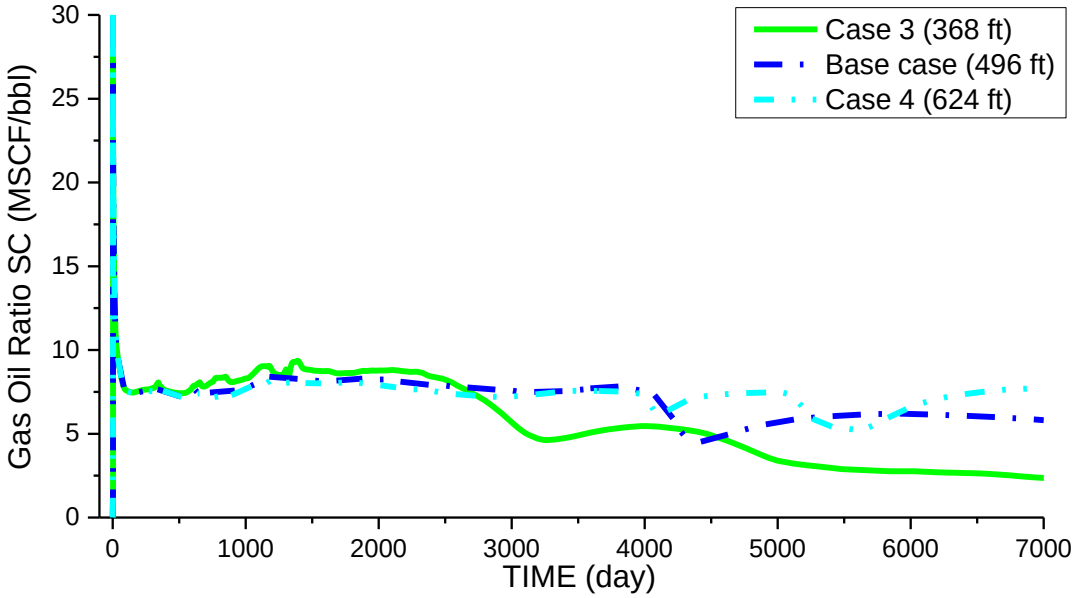

Figure 61. GOR trends as a function of the width of the SRV (Larger SRV)

The corresponding gas production rates are shown in Figure 62. The gas rates are reflective of the size of the SRV and decrease as a function of the SRV.

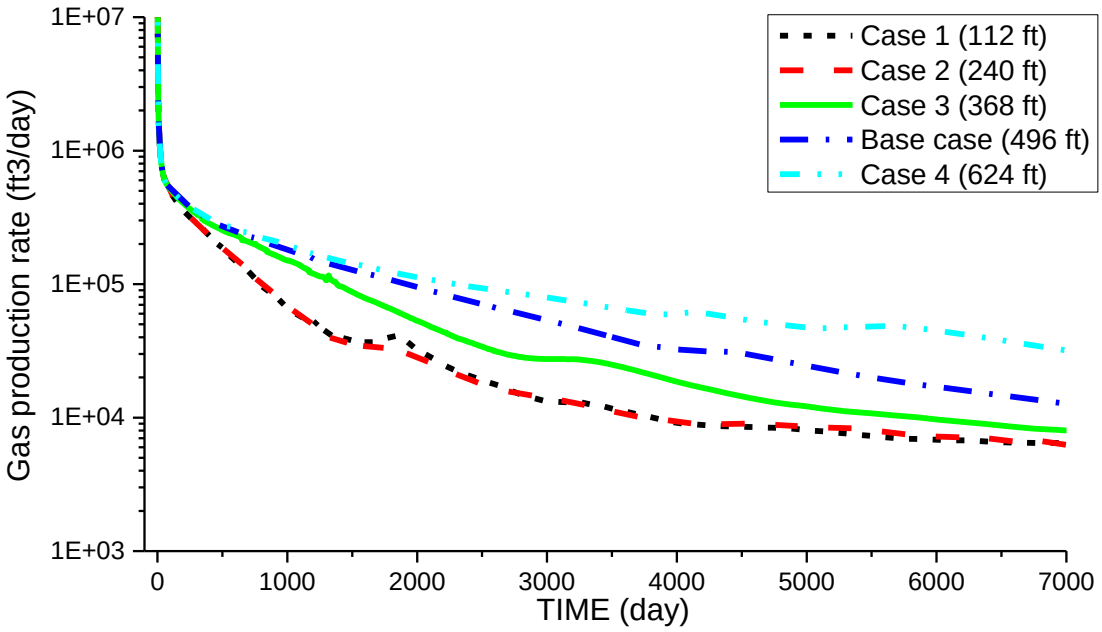

Figure 62. Gas production rates with different widths of the SRV

5.2. Diffusion Coefficients

In the case study presented in Chapter 4, the diffusion coefficient of C1 was chosen to be $2e^{-2}$ cm^2/s and this serves as a reference or base case for the sensitivity studies. The diffusion coefficients for other hydrocarbon species were scaled according to their molecular weights. The oil phase diffusion coefficients for the base case are set as $1e^{-2}$ times the gas phase diffusion coefficients. Table 15 lists the case studies considered in this sensitivity study.

Table 15. Diffusion coefficient (Gas phase) sensitivity study cases

Case #	Diffusion coefficients of the C1 (cm^2/s)
Base case	$2e^{-2}$
Case 1	$5e^{-3}$
Case 2	$1e^{-2}$

Figure 63 to Figure 66 illustrate the differences in production trends because of changes in diffusion coefficients. In all case studies, we observe a period of constant GOR production. In Figure 65, we see moderate differences in the gas rates while Figure 66 shows almost no differences in the oil rates. This is because the primary mode of diffusion is defined to be in the gas phase.

As shown earlier in Chapter 4, when the diffusion coefficients are negligible, the GOR tends to increase as soon as the well begins to produce. For the values chosen in this study, the differences are mostly reflected in the GOR trends and the oil saturation in the matrix system.

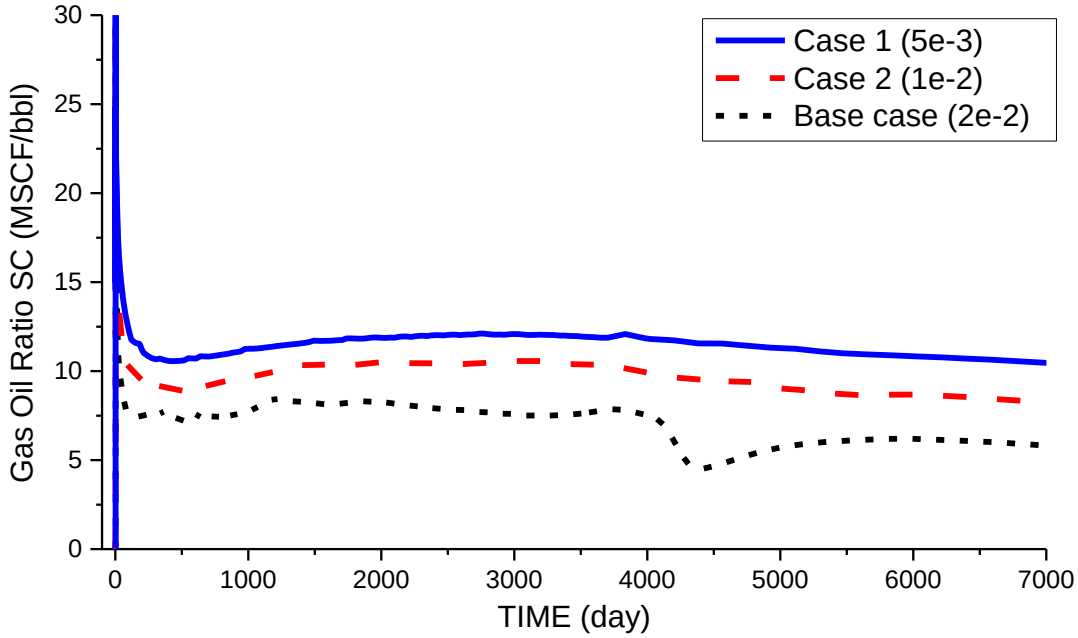

Figure 63. GOR trends with different diffusion coefficients.

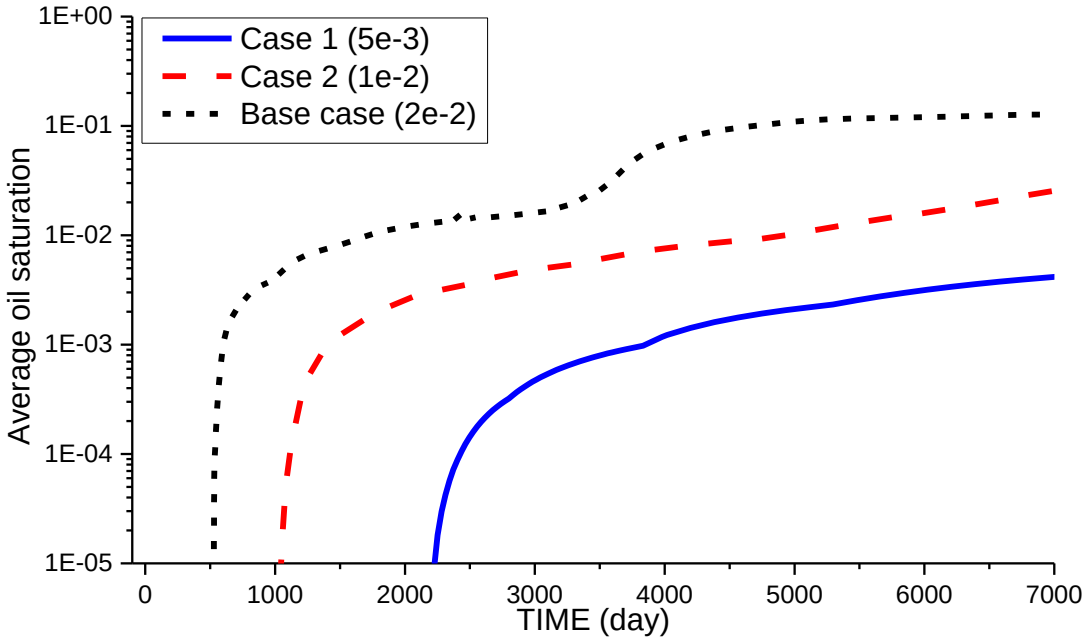

Figure 64. Average oil saturation in the matrix with different diffusion coefficients

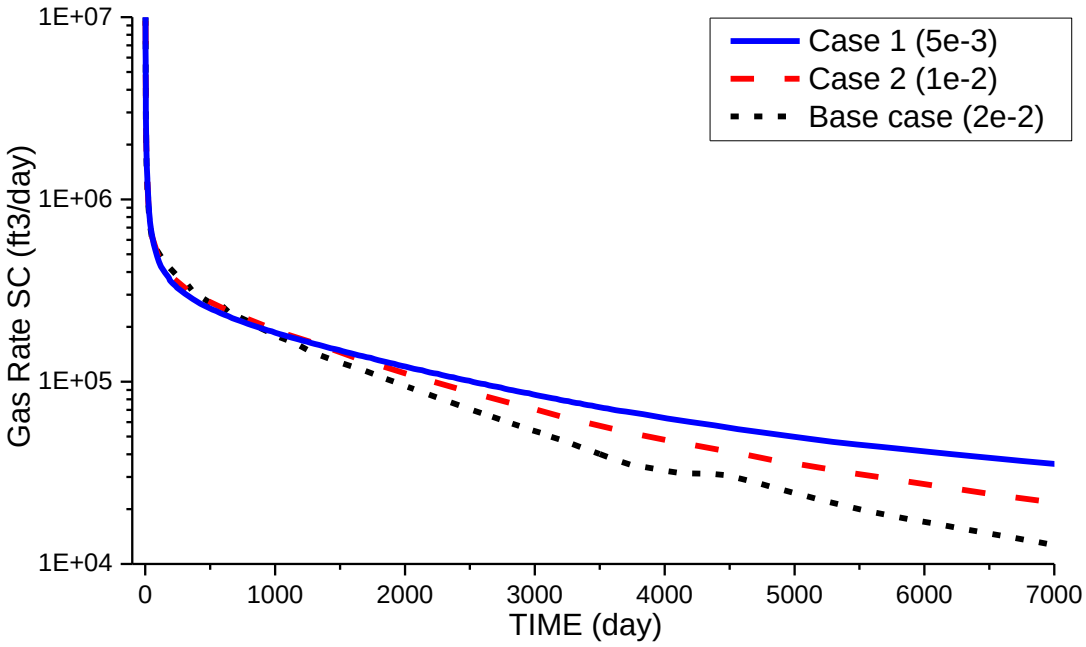

Figure 65. Gas production rate with different diffusion coefficients.

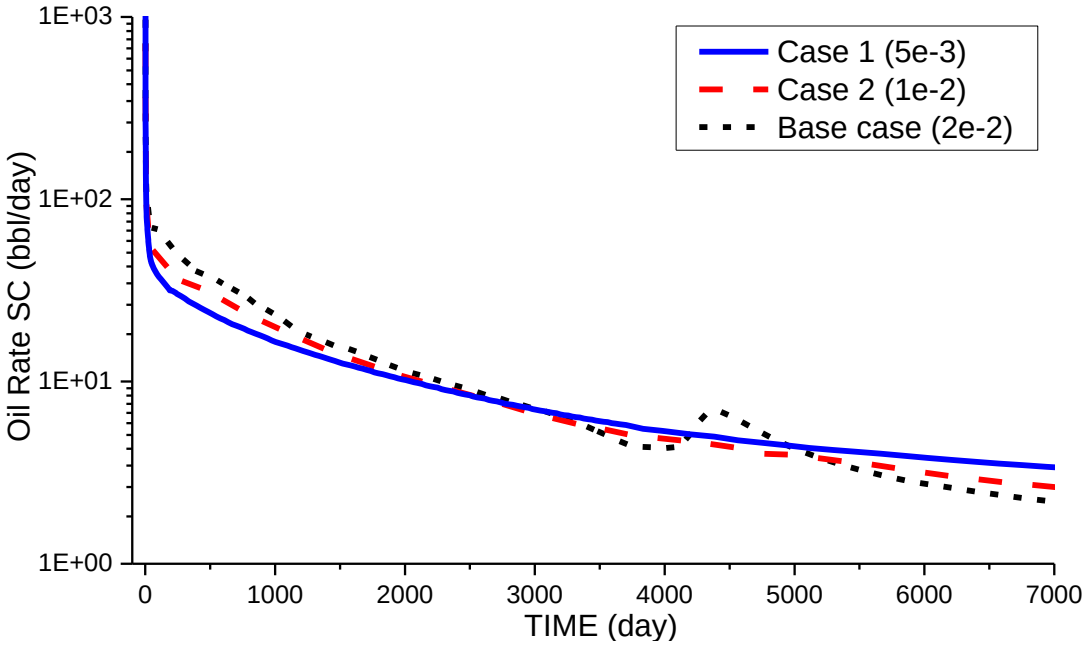

Figure 66. Oil production rate with different diffusion coefficients.

Pressure values within the matrix system in the reservoir are shown in Figure 67 to 68. The figures indicate that the pressure propagation is more rapid when the diffusion

coefficients are higher. This results in an earlier and more appreciable liquid dropout within the matrix as shown in Figure 64 as well.

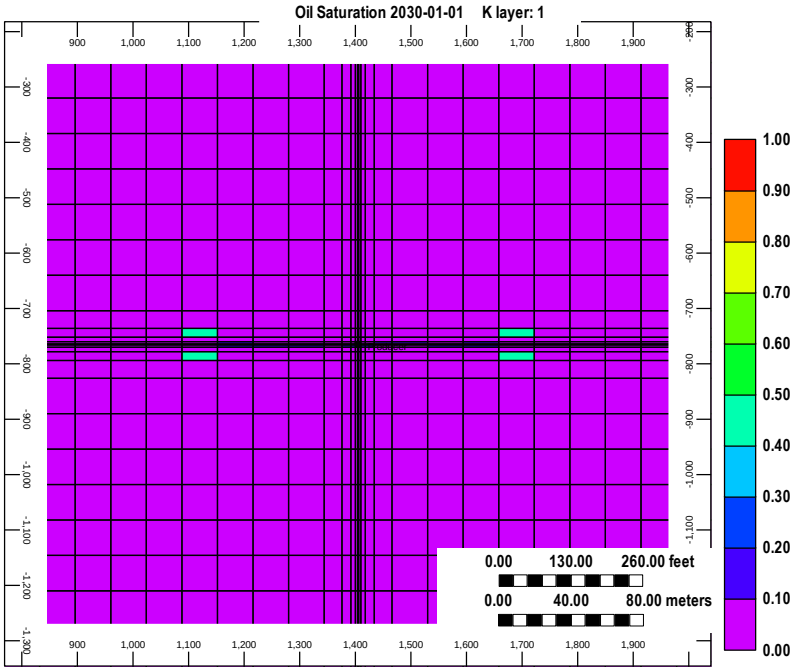

Figure 67. Oil saturation in matrix after 30 years of production with $D_k = 5e^{-3}$

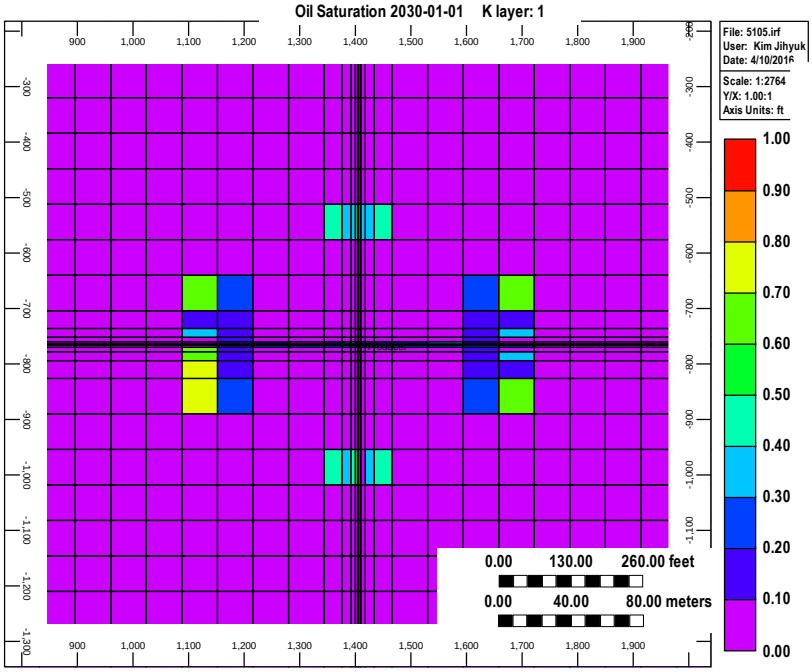

Figure 68. Oil saturation in matrix after 30 years of production with $D_k = 1e^{-2}$

5.3. Matrix Permeability

Although fluid transport from the shale matrix exists during entire period of production but is contribution to the overall production trend remains unclear. In this section, I vary the matrix permeability and assess if there are any changes to the production trends from the hydraulically fractured well. The case studies considered are listed in Table 16. The reader should note that this reflects only changes to the matrix; the surrounding un-stimulated natural fracture permeability remains $1e^{-4}$ md.

Table 16. Matrix permeability sensitivity cases.

Case #	Matrix permeability (md)
Base case	$1e^{-7}$
Case 1	$1e^{-8}$
Case 2	$1e^{-6}$
Case 3	$1e^{-5}$

Figure 69 plots the GOR trends for all case studies considered once again illustrating a stable GOR profile over extended periods of time. There are marginal differences in the GOR trends but no appreciable changes except when the matrix permeability is specified to be $1e^{-5}$ md. In this situation, there is appreciable condensate dropout in the matrix with an accompanying increase in the production GOR. This is also reflected in the marginal increase in condensate saturation in the matrix as shown in Figure 70.

However, these increases in matrix permeability do not have a significant or appreciable impact on the gas flow rates as shown in Figure 71 or on the oil flow rates as shown in Figure 72.

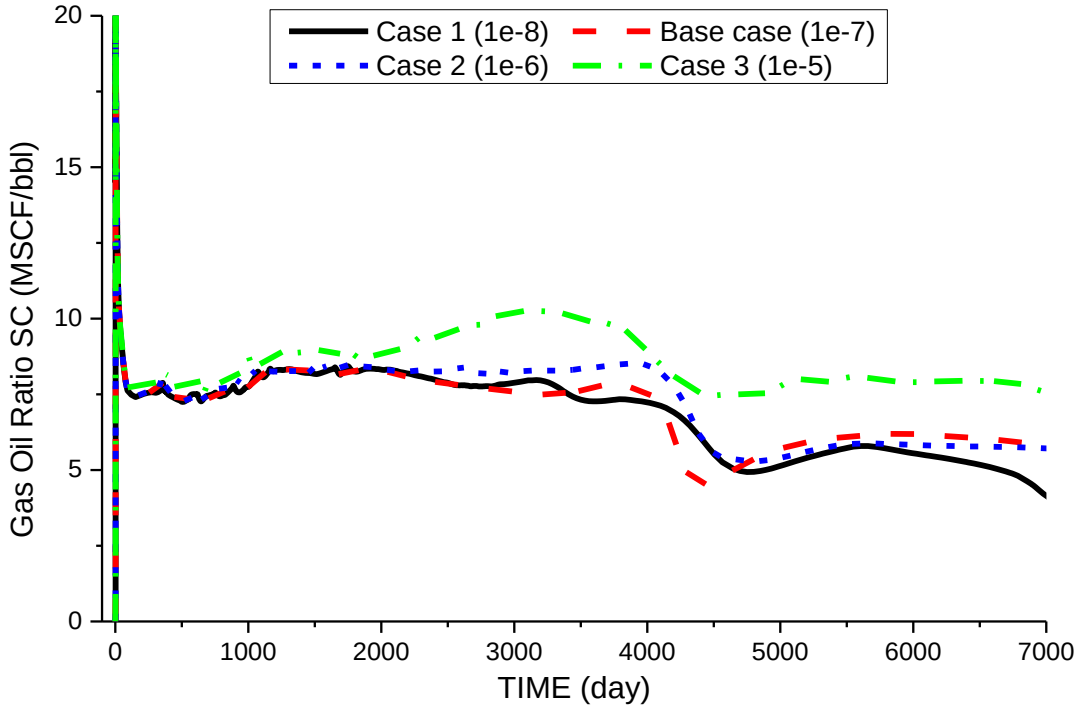

Figure 69. GOR with different matrix permeabilities

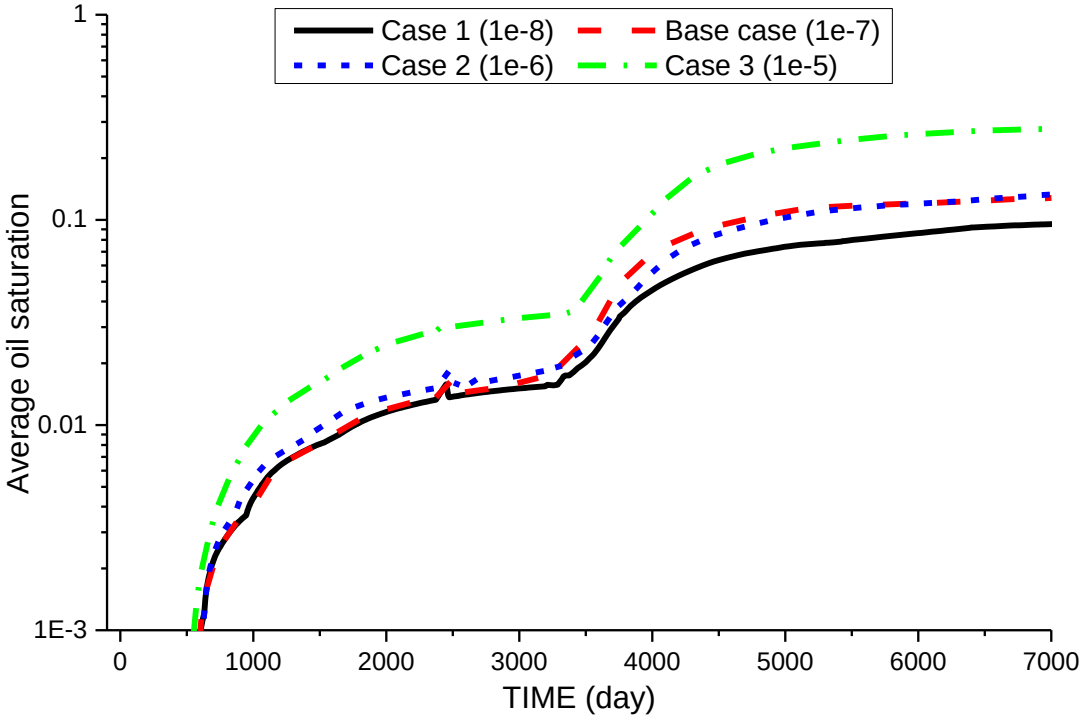

Figure 70. Average oil saturation in the matrix with different matrix permeabilities

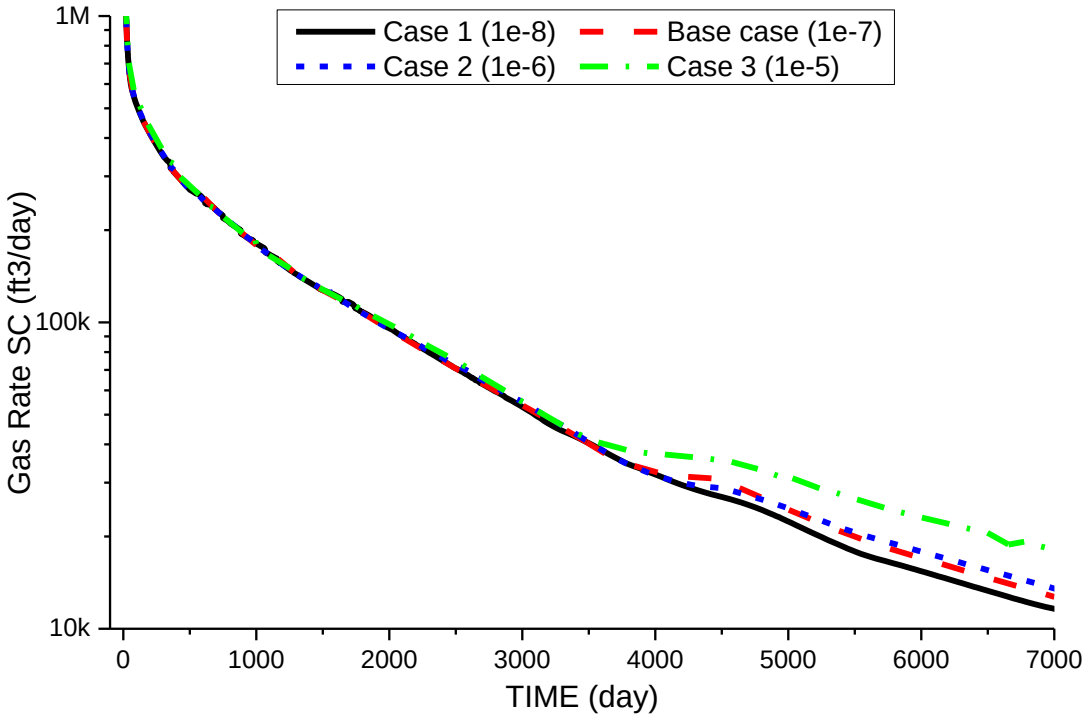

Figure 71. Gas production rates with different matrix permeabilities.

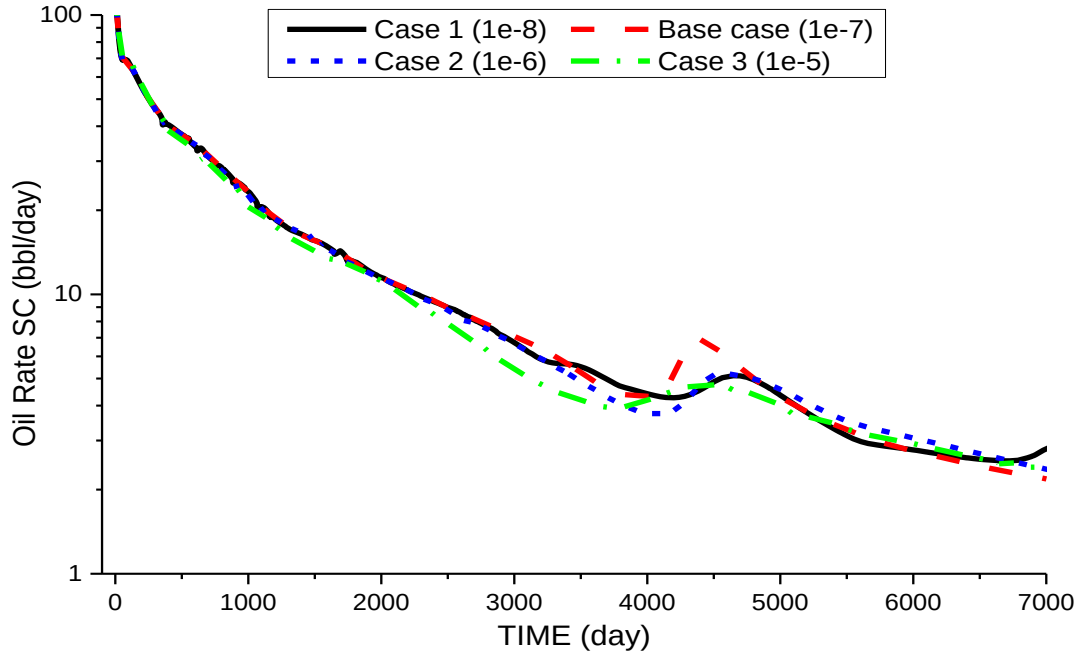

Figure 72. Oil production rates with different matrix permeabilities.

5.4. Effects of Adsorption

In all the case studies considered so far, adsorption was neglected. Because there is evidence of multicomponent adsorption in hydrophobic organic pores (Welch and Piri, 2015), I consider the impact of adsorption on the production trends. Table 17 provides a list of the adsorption parameters used in the extended Langmuir model specified in Equation 34. The rationale for the choice of the numerical values of these parameters is that heavier components are adsorbed more readily than the lighter components.

Table 17. Grouped components and adsorption coefficients

Group #	Components	*ADGMAXC (kg/lb)	*ADGCSTC (1/psi)
1	C1	0.084843	$1e^{-4}$
2	C2, C3	0.1	$2e^{-4}$
3	IC4, NC4, IC5, NC5, FC6	0.1	$3.\dot{3}e^{-4}$
4	FC7, FC8, FC9, FC10	0.1	$1e^{-3}$

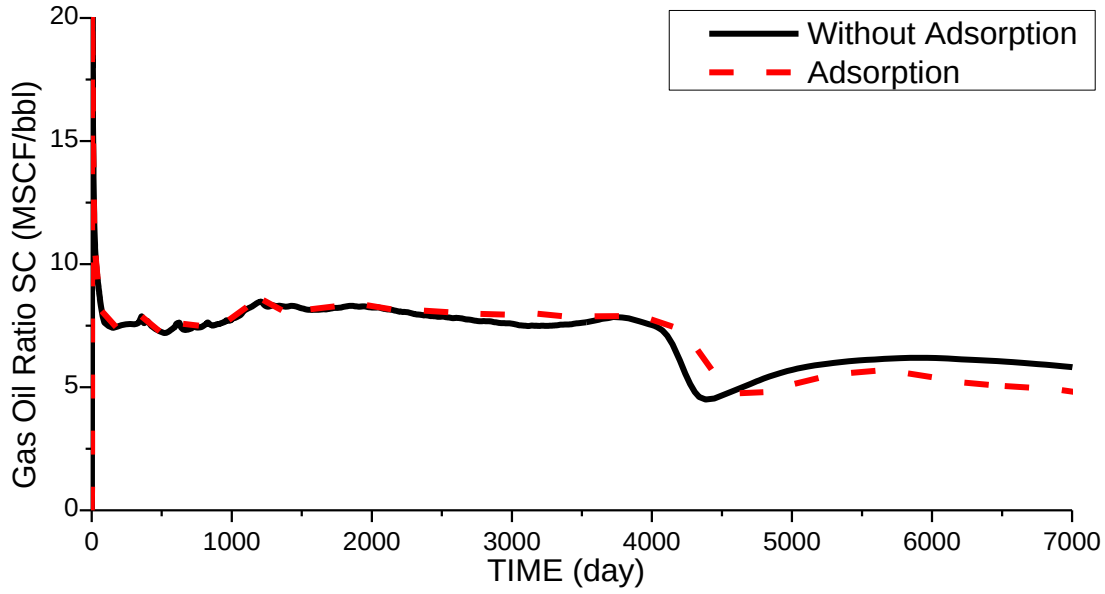

Figure 73. GOR with time (Adsorption and non-adsorption case)

Figure 73 shows the GOR trends comparing non-adsorbing pores with adsorbing pore surfaces and no appreciable difference is seen. This is because as discussed in Chapter 4, there is very limited pressure propagation in the matrix and as a consequence very limited pressure drops to create conditions favorable for substantial amounts of desorbed fluid migrating to the fracture systems. There are marginal changes late in the life of the well when the pressure transients reach the SRV boundary at which time there is an appreciable pressure drop in the unstimulated reservoir volume. Figure 74 to Figure 79 illustrate the produced fluid compositions as a function of time showing minimal differences with and without adsorption. There is however a small change in the compositions late in the life of the well when heavier components become desorbed and lead to production of a slightly richer gas condensate.

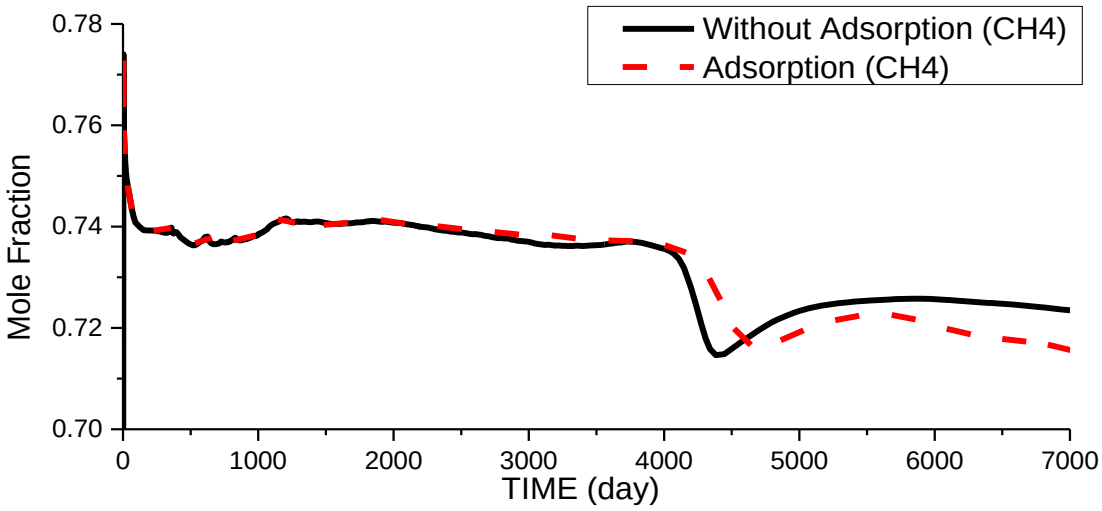

Figure 74. C1 mole fraction in the produced gas (Adsorption and non-adsorption case)

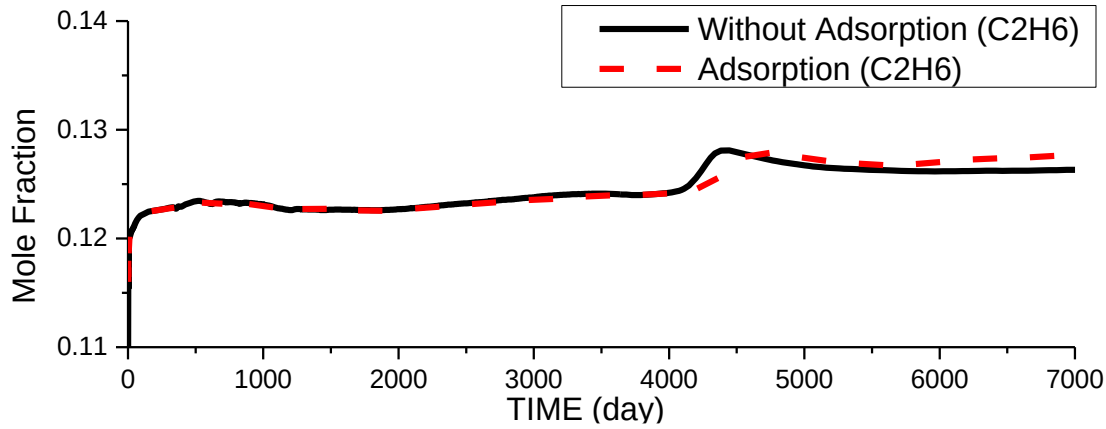

Figure 75. C2 mole fraction in the produced gas (Adsorption and non-adsorption case)

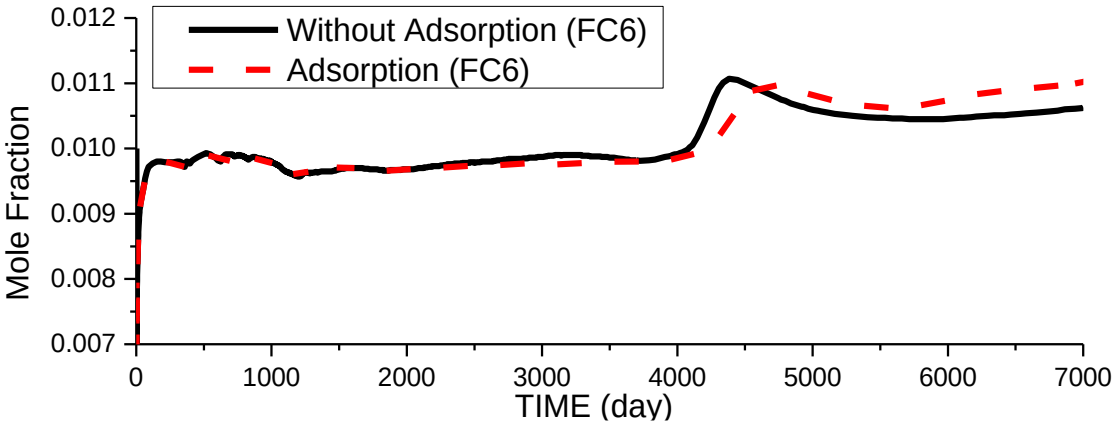

Figure 76. C6 mole fraction in the produced gas (Adsorption and non-adsorption case)

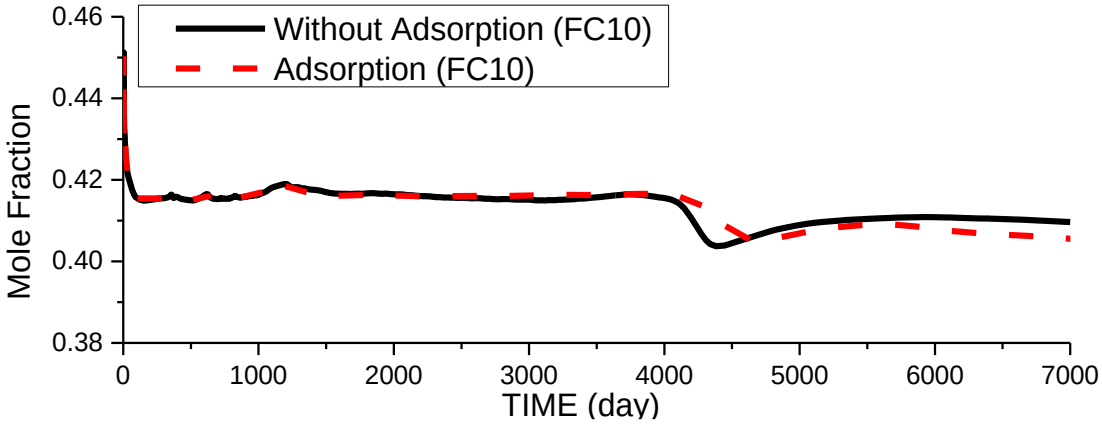

Figure 77. C10 mole fraction in the produced oil (Adsorption and non-adsorption case)

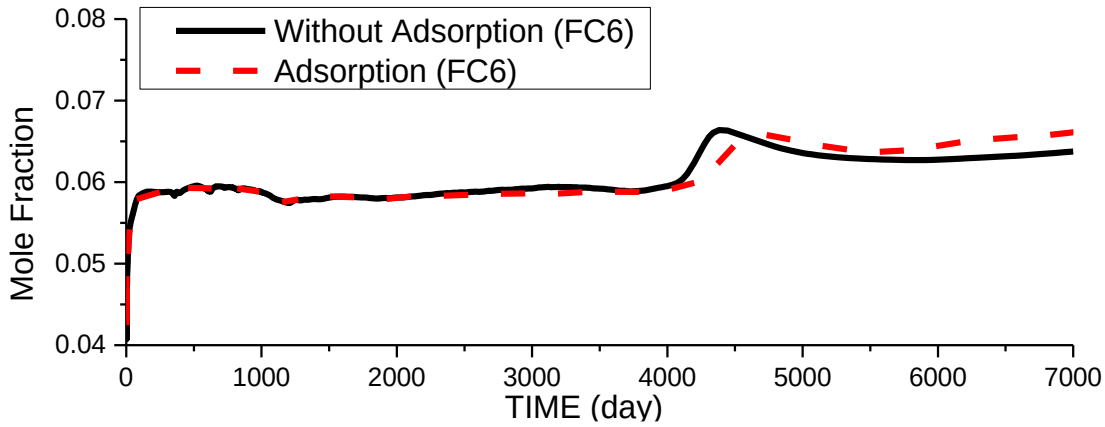

Figure 78. C6 mole fraction in the produced oil (Adsorption and non-adsorption case)

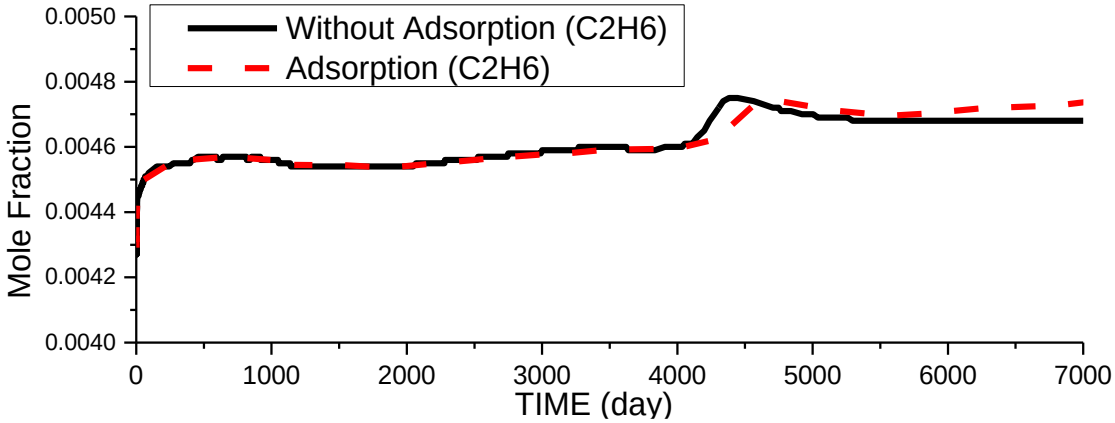

Figure 79. C2 mole fraction in the produced oil (Adsorption and non-adsorption case)

One of the assumptions made in this numerical sensitivity study is that the adsorption layer does not impact the Knudsen diffusion coefficients. In reality because of the smaller cross-sectional area available to flow, the slip flow effects should be enhanced with the presence of adsorption and this effect should be considerable for the smaller pores and pore throats within the shale matrix. This may create conditions where the GOR values are different based on the modified diffusion coefficients and the produced fluid compositions are also likely to be different especially when the matrix begins contributing to the overall transport in the reservoir.

Chapter 6. Conclusions and Recommendations

This study investigates the unique production trends of the liquids-rich shale reservoirs in terms of a stable GOR trend following an initial peak GOR with produced fluid compositions varying with time. The thesis is centered around the development of a multicomponent Knudsen diffusion model to explain some of these trends. A synthetic case study with a 1-D reservoir simulator built in-house as well as a more realistic field study were employed to illustrate the effects of multicomponent Knudsen diffusion on production GOR and produced fluid compositions.

The following conclusions can be drawn from this study:

1. A constant GOR or CGR profile is largely due to the competitive effects of Knudsen diffusion of lighter components over the heavier components which minimizes condensate dropout in the matrix.
2. With multicomponent diffusion, condensate dropout is only seen in the vicinity of the fracture and at the boundaries of the SRV. Largely, the matrix system is free of condensate build-up.
3. There is a strong link between the stimulated reservoir volume and the period of constant GOR production. As the SRV decreases in size, the contribution from the unstimulated reservoir volumes appears earlier and also accelerates condensate dropout.
4. Although this study does not provide a full treatment of multicomponent adsorption, the numerical case study illustrates that for extended periods of time, adsorption/desorption plays a limited role in governing GOR or CGR trends and produced fluid compositions.

Based on the results of this numerical simulation study, I also recommend that a core flow-through experiment at high pressures be conducted with multicomponent gas mixtures to assess GOR trends and produced fluid compositions. This experiment should be designed first with a 2-component non-adsorbing, non-condensing gas mixture at various pressures to see if multicomponent gas diffusion is valid across all pressures or restricted to specific pressure ranges. This should be followed by another flow through experiment with one of the components replaced by an adsorbing, non-condensing alternate and the set of experiments repeated. If multicomponent diffusion as discussed in this thesis is valid, then this set of experiments will allow us to distinguish the effects of adsorption and diffusion.

References

Arri, L. E., Yee, D., Morgan, W. D., and Jeansonne, M. W. (1992). Modeling coalbed methane production with binary gas sorption. In SPE Rocky Mountain Regional Meeting. Society of Petroleum Engineers.

Beskok, A., and Karniadakis, G. E. (1999). Report: a model for flows in channels, pipes, and ducts at micro and nano scales. Microscale Thermophysical Engineering, 3(1), 43-77.

Bosanquet, C. H. (1923). LV. On the flow of liquids into capillary tubes. The London, Edinburgh, and Dublin Philosophical Magazine and Journal of Science, 45(267), 525-531.

Carl, R, N., Mean Free Path. (1998). Retrieved from http://hydrogen.physik.uni-wuppertal.de/hyperphysics/hyperphysics/hbase/kinetic/menfre.html

Civan, F. (2010). Effective correlation of apparent gas permeability in tight porous media. Transport in porous media, 82(2), 375-384.

Cowling, T. G. (1970). Approximate theories of thermal diffusion. Journal of Physics A: General Physics, 3(6), 774.

Curtis, M. E., Ambrose, R. J., and Sondergeld, C. H. (2010). Structural Characterization of Gas Shales on the Micro- and Nano-Scales. Society of Petroleum Engineers. doi:10.2118/137693-MS

Devegowda, D., Sapmanee, K., Civan, F., and Sigal, R. F. (2012). Phase Behavior of Gas Condensates in Shales Due to Pore Proximity Effects: Implications for Transport, Reserves and Well Productivity. Society of Petroleum Engineers. doi:10.2118/160099-MS

Didar, B. and Akkutlu, I.Y. (2013). Pore-Size Dependence of Fluid Phase Behavior and Properties in Organic-Rich Shale Reservoirs. Presented at the SPE International Symposium on Oilfield Chemistry, The Woodlands Texas, 8-10 April. SPE-164099-MS. http://dx.doi.org/10.2118/164099-MS.

Do, H. D., Do, D. D., and Prasetyo, I. (2001). Surface diffusion and adsorption of hydrocarbons in activated carbon. American Institute of Chemical Engineers. AIChE Journal, 47(11), 2515.

Ertekin, T., King, G. A., and Schwerer, F. C. (1986). Dynamic gas slippage: a unique dual-mechanism approach to the flow of gas in tight formations. SPE formation evaluation, 1(01), 43-52.

Fathi, E., Tinni, A., and Akkutlu, I. Y. (2012). Shale gas correction to Klinkenberg slip theory. In SPE Americas Unconventional Resources Conference. Society of Petroleum Engineers.

Florence, F. A., Rushing, J., Newsham, K. E., and Blasingame, T. A. (2007). Improved permeability prediction relations for low permeability sands. In Rocky Mountain Oil & Gas Technology Symposium. Society of Petroleum Engineers.

Freeman, C. M. (2010). A Numerical Study of Microscale Flow Behavior in Tight Gas and Shale Gas. Society of Petroleum Engineers. doi:10.2118/141125-STU

Freeman, C. M., G. J., Michael, G. E., and Blasingame, T. A. (2012). Measurement, Modeling, and Diagnostics of Flowing Gas Composition Changes in Shale Wells. Society of Petroleum Engineers. doi:10.2118/153391-MS

Guo, Z. L., Shi, B. C., and Zheng, C. G. (2007). An extended Navier-Stokes formulation for gas flows in the Knudsen layer near a wall. EPL (Europhysics Letters), 80(2), 24001.

Hall, F. E., Chunhe, Z., Gasem, K. A. M., Robinson Jr, R. L., and Dan, Y. (1994). Adsorption of pure methane, nitrogen, and carbon dioxide and their binary mixtures on wet Fruitland coal. In SPE Eastern Regional Meeting. Society of Petroleum Engineers.

He, W., Lv, W., and Dickerson, J. (2014). Gas transport in solid oxide fuel cells (pp. 9-17). Springer.

Ho, C. K., and Webb, S. W. (Eds.). (2006). Gas transport in porous media (Vol. 20). Dordrecht: Springer.

Hoteit, H. (2013). Modeling diffusion and gas–oil mass transfer in fractured reservoirs. Journal of Petroleum Science and Engineering, 105, 1-17.

Jambhekar, V. A. (2011). Forchheimer Porous-Media Flow Models-Numerical Investigation and Comparison with Experimental Data. Published Master Thesis. Stuttgart: Universität Stuttgart-Institut für Wasserund Umweltsystem modellierung.

Javadpour, F., Fisher, D., and Unsworth, M. (2007). Nanoscale Gas Flow in Shale Sediments. Petroleum Society of Canada. doi:10.2118/07-10-06

Javadpour, F. (2009). Nanopores and apparent permeability of gas flow in mudrocks (shales and siltstone). Journal of Canadian Petroleum Technology, 48(08), 16-21.

Jin, L., Ma, Y., and Jamili, A. (2013). Investigating The Effect of Pore Proximity on Phase Behavior And Fluid Properties in Shale Formations. Society of Petroleum Engineers. doi:10.2118/166192-MS

Jones, F. O., and Owens, W. W. (1980). A laboratory study of low-permeability gas sands. Journal of Petroleum Technology, 32(09), 1-631.

Khoshghadam, M., Khanal, A., and Lee, W. J. (2015). Numerical Study of Production Mechanisms and Gas-Oil Ratio Behavior of Liquid-Rich Shale Oil Reservoirs. Society of Petroleum Engineers. doi:10.2118/175137-MS

Kim, C., Jang, H., Lee, Y., and Lee, J. (2016). Diffusion characteristics of nanoscale gas flow in shale matrix from Haenam basin, Korea. Environmental Earth Sciences, 75(4), 1-8.

Klinkenberg, L. J. (1941). The permeability of porous media to liquids and gases. In Drilling and production practice. American Petroleum Institute.

Knudsen, M. (1934). The Kinetic Theory of Gases, Methuen & Co. Ltd., London.

Lee, A. L., Gonzalez, M. H., and Eakin, B. E. (1966). The viscosity of natural gases. Journal of Petroleum Technology, 18(08), 997-1.

Li, J., and Sultan, A. (2015). Klinkenberg slippage effect in the permeability computations of shaleby the pore-scale simulations. arXiv preprint arXiv:1505.01781.

Litster, S., and Djilali, N. (2005). Two-phase transport in porous gas diffusion electrodes. Developments in Heat Transfer, 19, 175.

Mannarelli, M. (2013). Trapped phonons. arXiv preprint arXiv:1301.6074.

Mason, E. A., and Malinauskas, A. P. (1983). Gas transport in porous media: the dusty-gas model (Vol. 17). Elsevier Science Ltd.

Mathur, A. (2015). Experimental Investigation of Matrix Permeability of Shale.

Michel, G., Civan, F., Sigal, R., and Devegowda, D. (2011). Proper Modeling Of Nano-Scale Real-Gas Flow Through Extremely Low-Permeability Porous Media Under Elevated Pressure And Temperature Conditions. In 7th International conference on computational heat and mass transfer, Istanbul, Turkey (pp. 18-22).

Muskat, M. (1937). The flow of homogeneous fluids through porous media. MacGraw-Hill, New York.

Passey, Q. R., Bohacs, K., Esch, W. L., Klimentidis, R., and Sinha, S. (2010). From Oil-Prone Source Rock to Gas-Producing Shale Reservoir - Geologic and Petrophysical Characterization of Unconventional Shale Reservoirs. Society of Petroleum Engineers. doi:10.2118/131350-MS

Reif, F. (2009). Chapter 12/elementary kinetic theory of transport processes. In Fundamentals of Reinecke statistical and thermal physics. Waveland Press.

Reinecke, S. A., and Sleep, B. E. (2002). Knudsen diffusion, gas permeability, and water content in an unconsolidated porous medium. Water Resources Research, 38(12).

Sakhaee-Pour, A., and Bryant, S. (2012). Gas permeability of shale. SPE Reservoir Evaluation & Engineering, 15(04), 401-409.

Sampath, K., and Keighin, C. W. (1982). Factors affecting gas slippage in tight sandstones of cretaceous age in the Uinta basin. Journal of Petroleum Technology, 34(11), 2-715.

Schettler, P. D., and Parmely, C. R. (1989). Gas Composition Shifts in Devonian Shales. Society of Petroleum Engineers. doi:10.2118/17033-PA

Serway, R. A., Beichner, R. J., and Jewett, J. W. (2000). Physics for scientists and engineers with modern physics.

Shale in the United States., EIA. (2016). Retrieved April 26, 2016, from http://www.eia.gov/energy_in_brief/article/shale_in_the_united_states.cfm

Shi, J., Zhang, L., Li, Y., Yu, W., He, X., Liu, N., and Wang, T. (2013). Diffusion and Flow Mechanisms of Shale through Matrix Pores and Gas Production Forecasting. Society of Petroleum Engineers. doi:10.2118/167226-MS

Sigal, R. F. (2015). Pore-Size Distributions for Organic-Shale-Reservoir Rocks From Nuclear-Magnetic-Resonance Spectra Combined With Adsorption Measurements. SPE Journal.

Swami, V., Clarkson, C. R., and Settari, A. (2012). Non-Darcy Flow in Shale Nanopores: Do We Have a Final Answer? Society of Petroleum Engineers. doi:10.2118/162665-MS

Gupta, D. K., Bhan, U., Krishna, K.V., and Alluka, D. (2015). Study of Apparent Permeability in Shale Reservoirs. International Journal of Engineering Research & Technology, Vol.4(Issue 03),. Doi: http://dx.doi.org/10.17577/IJERTV4IS030846

Wang, C. (2014). Organic and Inorganic Pore Structure Analysis in Shale Matrix with Superposition Method. Unconventional Resources Technology Conference (URTEC).

Wang, J., Luo, H., Liu, H., Ji, Y., Cao, F., Li, Z., and Sepehrnoori, K. (2015). Variations of Gas Flow Regimes and Petro-Physical Properties During Gas Production Considering Volume Consumed by Adsorbed Gas and Stress Dependence Effect in Shale Reservoirs. Society of Petroleum Engineers. doi:10.2118/174996-MS

Warburg, E., Poggendorfs Ann. Physik159, 399 (1876)

Webb, S. W. (1996). Gas-phase diffusion in porous media: Evaluation of an advective-dispersive formulation and the dusty-gas model including comparison to data for binary mixtures. Sandia National Laboratories.

Welch, W. R., and Piri, M. (2015). Molecular Dynamics Simulations of Retrograde Condensation in Narrow Oil-Wet Nanopores. The Journal of Physical Chemistry C, 119(18), 10040-10047.

Welty, J. R., Wicks, C. E., Rorrer, G., and Wilson, R. E. (2009). Fundamentals of momentum, heat, and mass transfer. John Wiley & Sons.

Wu, Q. (2014). Investigation of fluids flow behavior in nanoscale channels by using optic imaging system.

Wu, Y. S., and Pruess, K. (1998). Gas flow in porous media with Klinkenberg effects. Transport in porous Media, 32(1), 117-137.

Zalc, J. M., Reyes, S. C., and Iglesia, E. (2004). The effects of diffusion mechanism and void structure on transport rates and tortuosity factors in complex porous structures. Chemical Engineering Science, 59(14), 2947-2960.

Zhang, P., and Hu, L. (2014). A numerical study of shale gas flow considering pore scale effect.

Appendix A. Derivation of Klinkenberg Gas Permeability (Equation 14)

1. Velocity near the Wall

Let w0 is the velocity near the wall under constant velocity gradient dw/dr, the velocity at a distance z from the wall can defined as below Equation A1.

$$w_a = w_0 + z\frac{dw}{dz} \tag{A1}$$

Replace z, distance from the wall with mean free path λ of the gas molecules gives:

$$\bar{z} = c\lambda$$

Where c : proportional factor

Therefore the average velocity of the molecule is:

$$\bar{w} = w_0 + c\lambda\frac{dw}{dz}$$

When the collision with the wall is defined as perfectly inelastic collision, half of the molecules located in the tube move towards to wall will lose its velocity but not for another half at time t. So the average molecular velocity is:

$$\bar{w} = \frac{1}{2}\left(w_0 + c\lambda\frac{dw}{dz}\right)$$

$$\bar{w} = c\lambda\frac{dw}{dz} \tag{A2}$$

2. Derive Flow of Gas through a Straight Capillary

A flow in a capillary tube with radius r and r+dr between cross-section x and x+dx under constant velocity gradient dw/dr which is comparable the difference of pressure defined as below Equation A3 by Warburg (1876).

$$-\frac{d}{dr}\left(\mu\frac{dw}{dr}\cdot 2\pi r dx\right)dr = -\frac{dP}{dx}\cdot 2\pi r dx \tag{A3}$$

Re-arrange above Equation A3 gives Equation A4 as below:

$$\frac{d}{dr}\left(r\frac{dw}{dr}\right) = \frac{dP}{dx}\cdot\frac{r}{\mu} \tag{A4}$$

Integration of Equation A4 gives:

$$r\frac{dw}{dr} = \frac{1}{2\mu}\cdot\frac{dP}{dx}r^2 + A \tag{A5}$$

Another integration of Equation A5 gives:

$$w = \frac{1}{4\mu}\cdot\frac{dP}{dx}r^2 + A\ln r + B \tag{A6}$$

When the r=0 from the Equation A6, A=0

And when the r=r0 with the Equation A2 gives:

$$\bar{w} = c\lambda\frac{dw}{dz} = -\left(c\lambda\frac{dw}{dr}\right)_{r=r_0} \tag{A7}$$

Combine Equation A5 and Equation A7 gives:

$$-\left(c\lambda\frac{dw}{dr}\right)_{r=r_0} = \frac{1}{4\mu}\cdot\frac{dP}{dx}{r_0}^2 + B$$

$$B = -\left(c\lambda \frac{dw}{dr}\right)_{r=r_0} - \frac{1}{4\mu} \cdot \frac{dP}{dx} {r_0}^2 \tag{A8}$$

Re-arrange Equation A5 gives:

$$\left(\frac{dw}{dr}\right)_{r=r_0} = \frac{r_0}{2\mu} \cdot \frac{dP}{dx} \tag{A9}$$

Apply Equation A9 to Equation A8:

$$B = -c\lambda \cdot \frac{r_0}{2\mu} \cdot \frac{dP}{dx} - \frac{1}{4\mu} \cdot \frac{dP}{dx} {r_0}^2 \tag{A10}$$

Combine Equation A10 and Equation A6:

$$\begin{aligned} w &= \frac{1}{4\mu} \cdot \frac{dP}{dx} r^2 - c\lambda \cdot \frac{r_0}{2\mu} \cdot \frac{dP}{dx} - \frac{1}{4\mu} \cdot \frac{dP}{dx} {r_0}^2 \\ &= -\frac{1}{4\mu} \cdot \frac{dP}{dx} ({r_0}^2 - r^2 + 2c\lambda r_0) \end{aligned} \tag{A11}$$

When the gas flows between two cylindrical area with radius r and r+dr during time t, total volume passing through the area is:

$$dV = -\frac{\pi}{2\mu} \cdot \frac{dP}{dx} \cdot t({r_0}^2 - r^2 + 2c\lambda r_0) r dr$$

And when the flow occurs through entire tube:

$$V = -\frac{\pi}{2\mu} \cdot \frac{dP}{dx} \cdot t \int_0^{r_0} ({r_0}^2 - r^2 + 2c\lambda r_0) r dr$$

$$V = -\frac{\pi {r_0}^4}{8\mu} \cdot \frac{dP}{dx} \cdot t\left(1 + \frac{4c\lambda}{r_0}\right) \tag{A12}$$

If n gram mole is pass through the capillary per unit time t,

$$\frac{PV}{t} = nRT$$

$$V = \frac{tnRT}{P} \tag{A13}$$

Substitute above Equation A13 to Equation A12 and re-arrange:

$$nRTdx = -\frac{\pi {r_0}^4}{8\mu}\left(PdP + \frac{4c\lambda P}{r_0}dP\right) \tag{A14}$$

With the mean free path definition,

$$4c\lambda = \frac{b}{P}$$

And integrate Equation A14 to capillary tube of length 'l' gives:

$$nRTl = -\frac{\pi {r_0}^4}{8\mu}\int_{P_1}^{P_2}\left(PdP + \frac{b}{r_0}dP\right)$$

$$nRTl = \frac{\pi {r_0}^4}{8\mu}\left(\frac{{P_1}^2 - {P_2}^2}{2} + \frac{b}{r_0}(P_1 - P_2)\right) = \frac{PVl}{t}$$

Therefore:

$$\frac{PV}{t} = Q = \frac{\pi {r_0}^4}{8\mu l}(P_1 - P_2)\left(\frac{P_1 + P_2}{2}\right)\left(1 + \frac{b}{\frac{1}{2}(P_1 + P_2)r_0}\right)$$

If $\bar{\lambda}$ is the mean free path at the mean pressure, $\overline{P} = \frac{1}{2}(P_1 + P_2)$,

$$Q = \frac{\pi {r_0}^4}{8\mu l}(P_1 - P_2)\cdot\overline{P}\cdot\left(1 + \frac{b}{\frac{1}{2}(P_1 + P_2)r_0}\right)$$

$$Q = \frac{\pi {r_0}^4}{8\mu l}(P_1 - P_2)\cdot\overline{P}\cdot\left(1 + \frac{4c\bar{\lambda}}{r_0}\right) \tag{A15}$$

3. Derive Flow of Gas through an Idealized Porous Medium

When assume all the pores in the porous medium have same diameter for ideal condition, flow of gas can be quantified.

Assume n of the capillaries of the porous medium with an edge of 1cm which is perpendicular with flow direction with radius r. Then the amount of fluid flowing can estimated by using Poiseuille's law as below Equation A16 and Equation A17 by using Darcy's law.

$$\frac{V}{t} = \frac{n\pi r^4}{8\mu} \cdot (P_1 - P_2) \tag{A16}$$

$$\frac{V}{t} = \frac{K}{\mu} \cdot (P_1 - P_2) \tag{A17}$$

Therefore, the permeability K is defined as below Equation A18:

$$K = \frac{n\pi r^4}{8} \tag{A18}$$

Take consideration of the gas phase flow which were defined as above Equation A15 with Equation A18 gives:

$$Q = \frac{K}{\mu} \cdot (P_1 - P_2) \cdot \overline{P}\left(1 + \frac{4c\bar{\lambda}}{r}\right) \tag{A19}$$

Again, from the Darcy's law, the gas flow is defined as:

$$Q = \frac{K_a}{\mu} \cdot (P_1 - P_2) \cdot \overline{P} \tag{A20}$$

Combine Equation A19 and Equation A20 gives the apparent gas permeability as below Equation A21.

$$K_a = K\left(1 + \frac{4c\bar{\lambda}}{r}\right) \tag{A21}$$

Where applying average mean free path definition with above Equation A21 gives apparent and true gas permeability relation in ideal porous medium as Equation A22 which is the Equation 14 in this paper.

$$\frac{4c\bar{\lambda}}{r} = \frac{b}{\bar{P}}$$

$$K_a = K\left(1 + \frac{b}{\bar{P}}\right) \tag{A22}$$

Appendix B. Normalized Composition Trends

This appendix provides the normalized composition plots for the synthetic case study presented in Chapter 3 as well as the field scale case study of Chapter 4. The normalized composition is defined as the ratio of the instantaneous composition to the original composition.

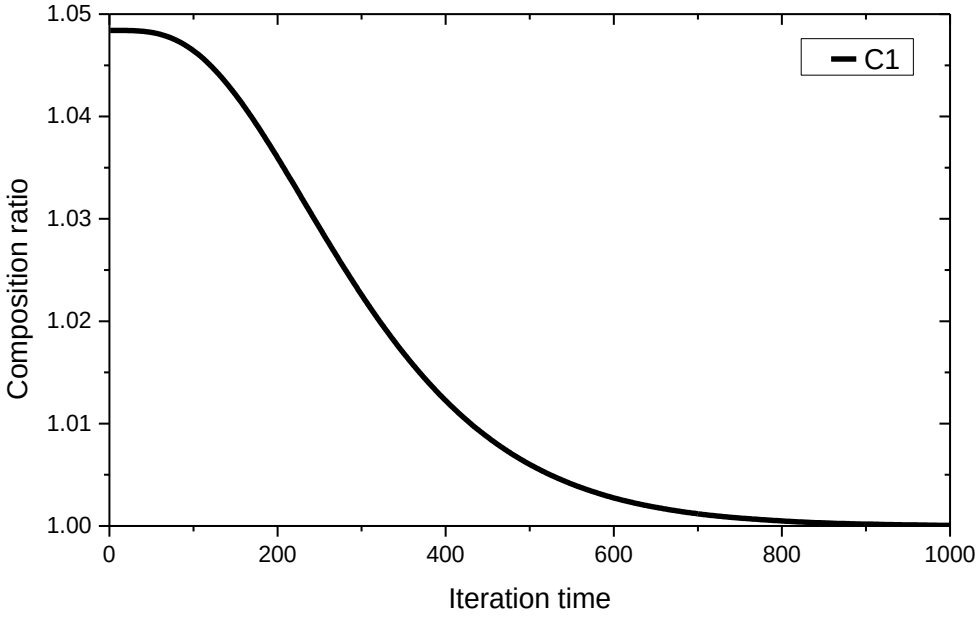

Figure 80. C1 mole fraction ratio (Equivalent to Figure 24)

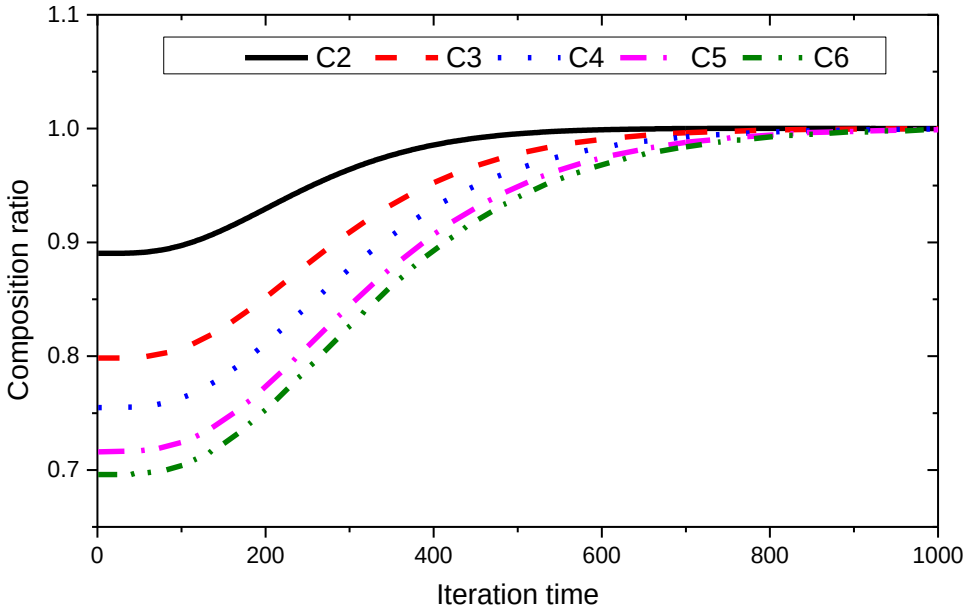

Figure 81. C2-C6 mole fraction ratio (Equivalent to Figure 25)

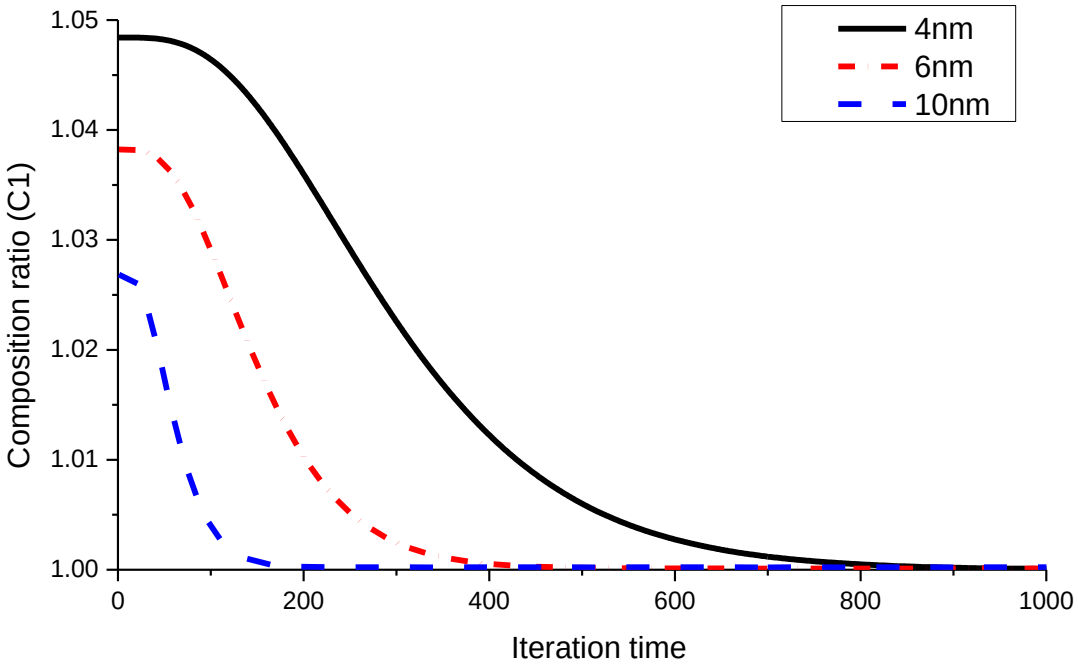

Figure 82. C1 mole ratio in the produced fluid as a function of time in 4nm, 6nm, 10nm diameter pores (Equivalent to Figure 26)

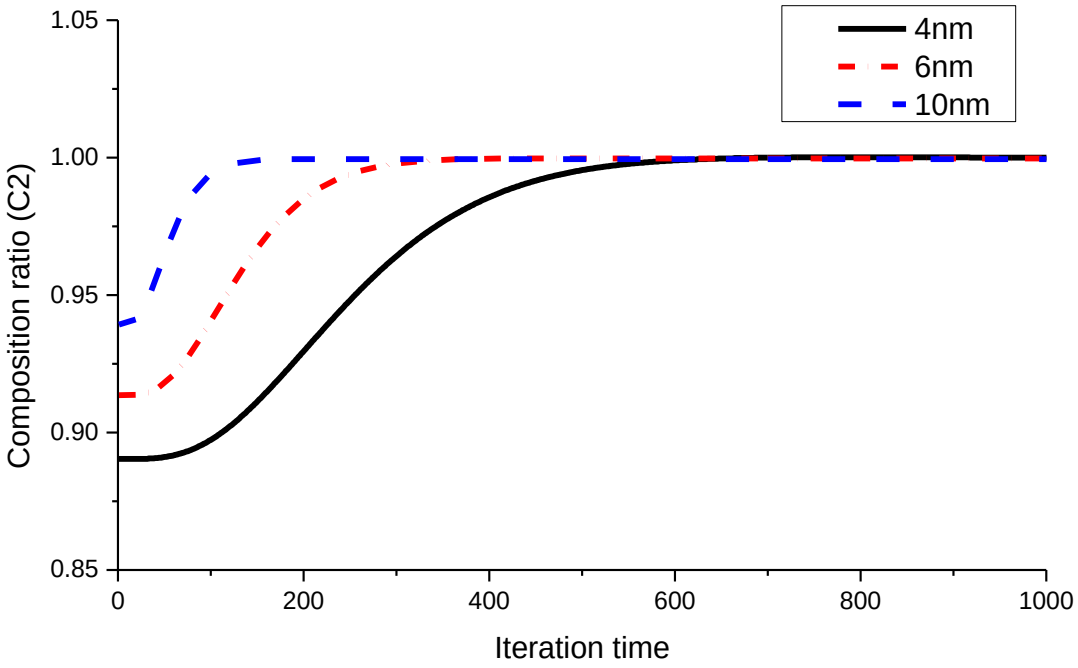

Figure 83. C2 mole ratio in the produced fluid as a function of time in 4nm, 6nm, 10nm diameter pores (Equivalent to Figure 27)

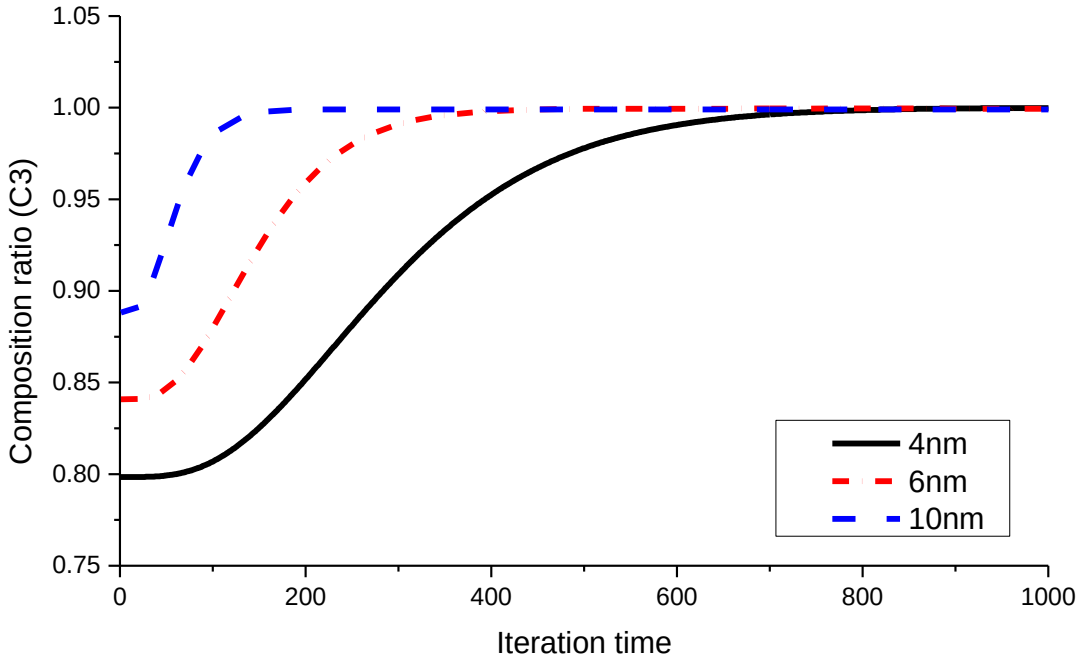

Figure 84. C3 mole ratio in the produced fluid as a function of time in 4nm, 6nm, 10nm diameter pores (Equivalent to Figure 28)

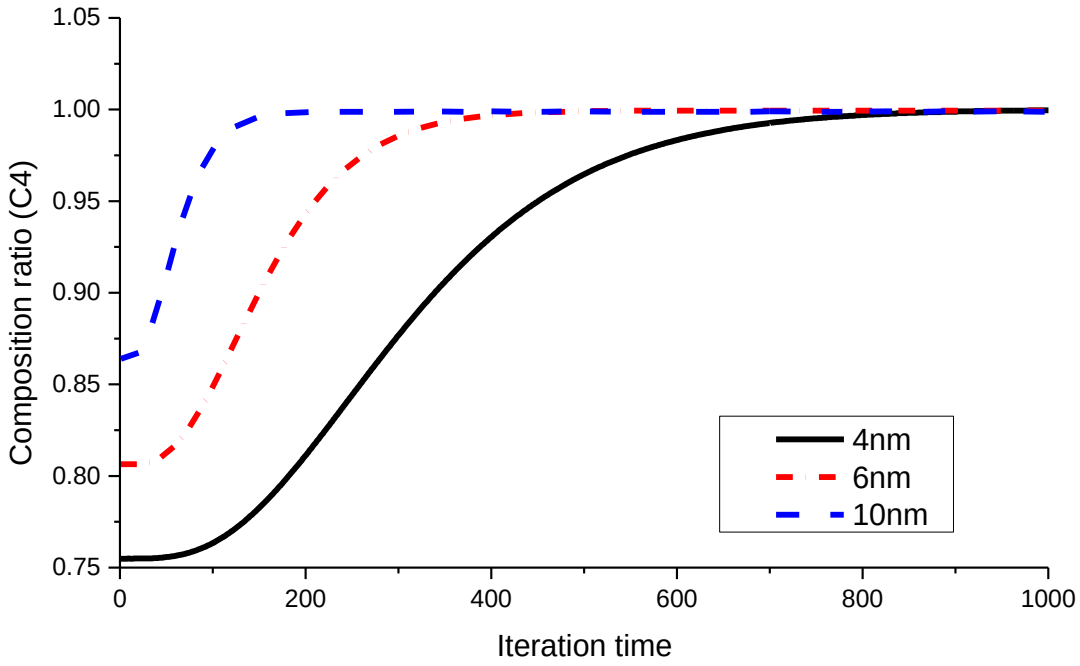

Figure 85. C4 mole ratio in the produced fluid as a function of time in 4nm, 6nm, 10nm diameter pores (Equivalent to Figure 29)

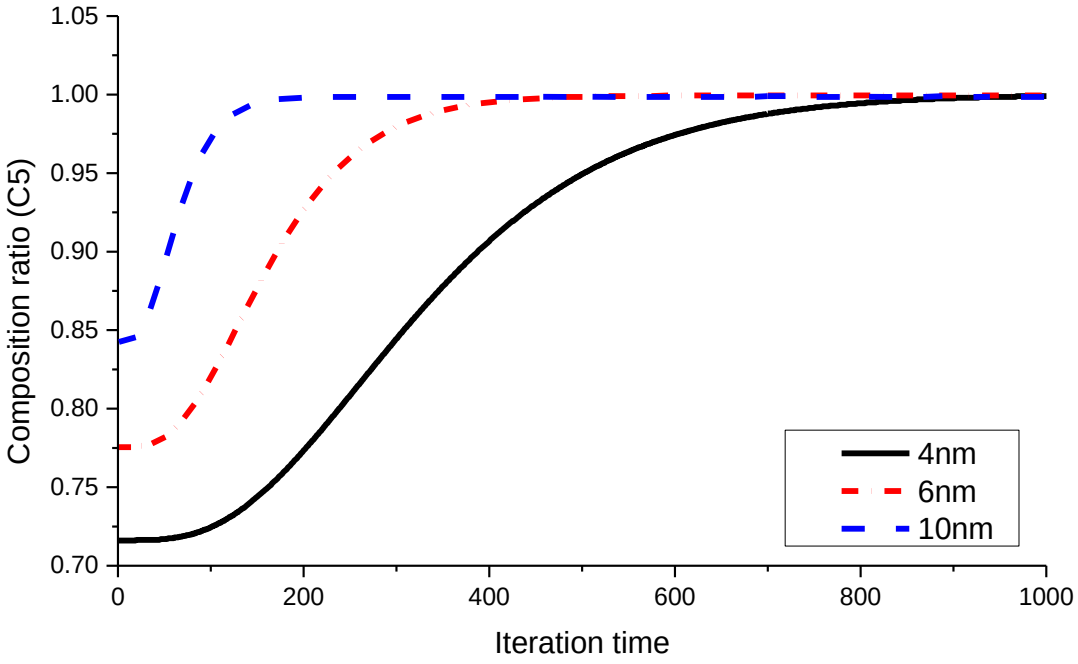

Figure 86. C5 mole ratio in the produced fluid as a function of time in 4nm, 6nm, 10nm diameter pores (Equivalent to Figure 30)

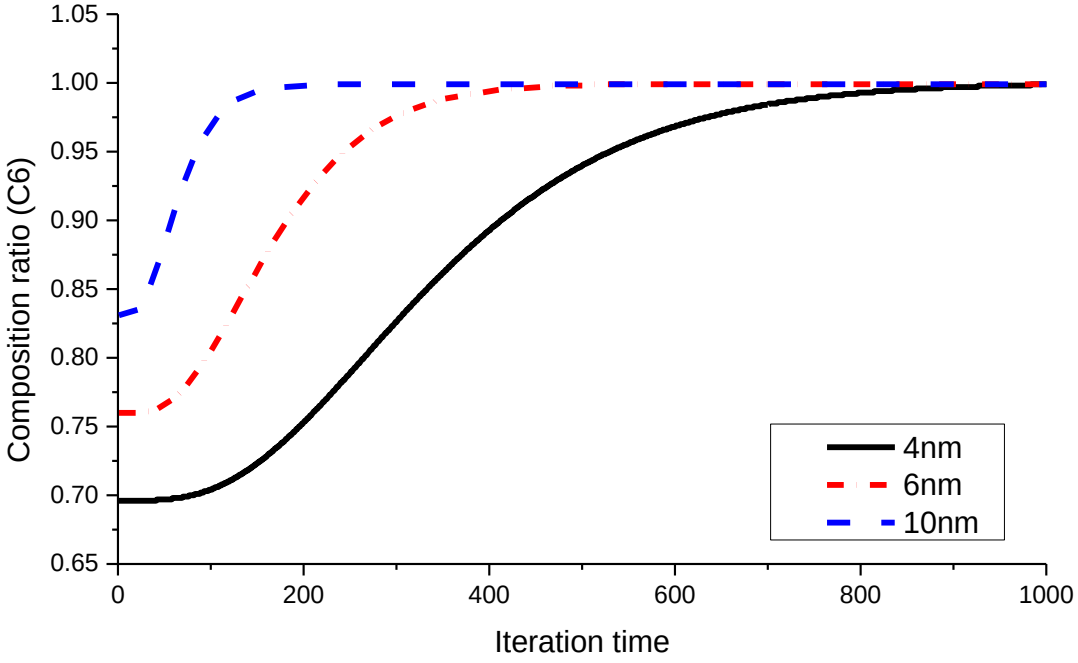

Figure 87. C6 mole ratio in the produced fluid as a function of time in 4nm, 6nm, 10nm diameter pores (Equivalent to Figure 31)

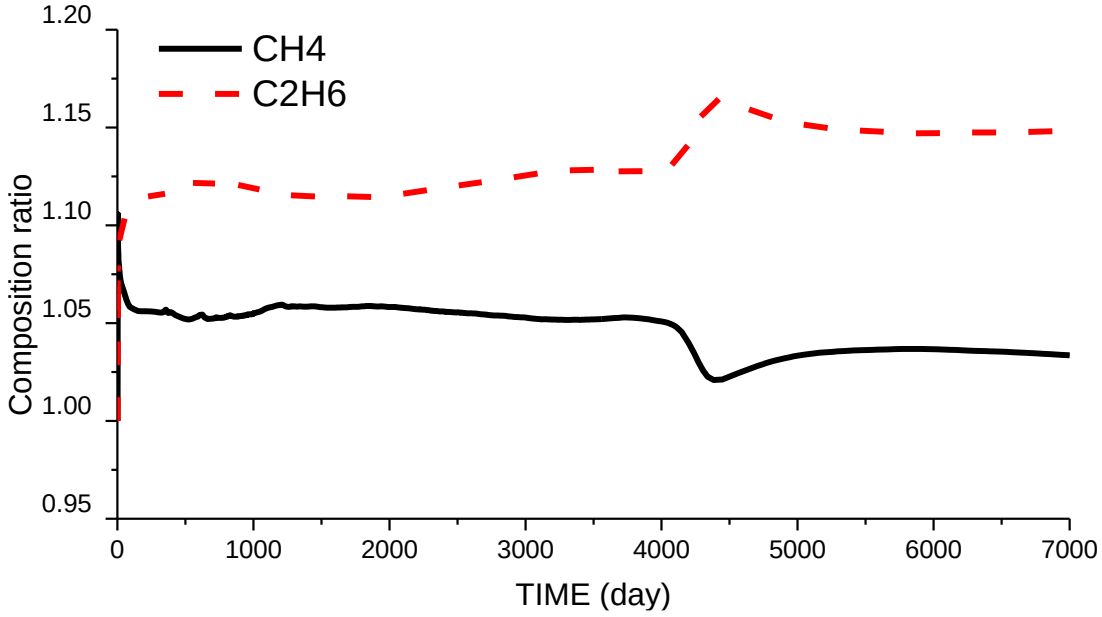

Figure 88. Produced gas composition ratio of C1 and C2 (Equivalent to Figure 52)

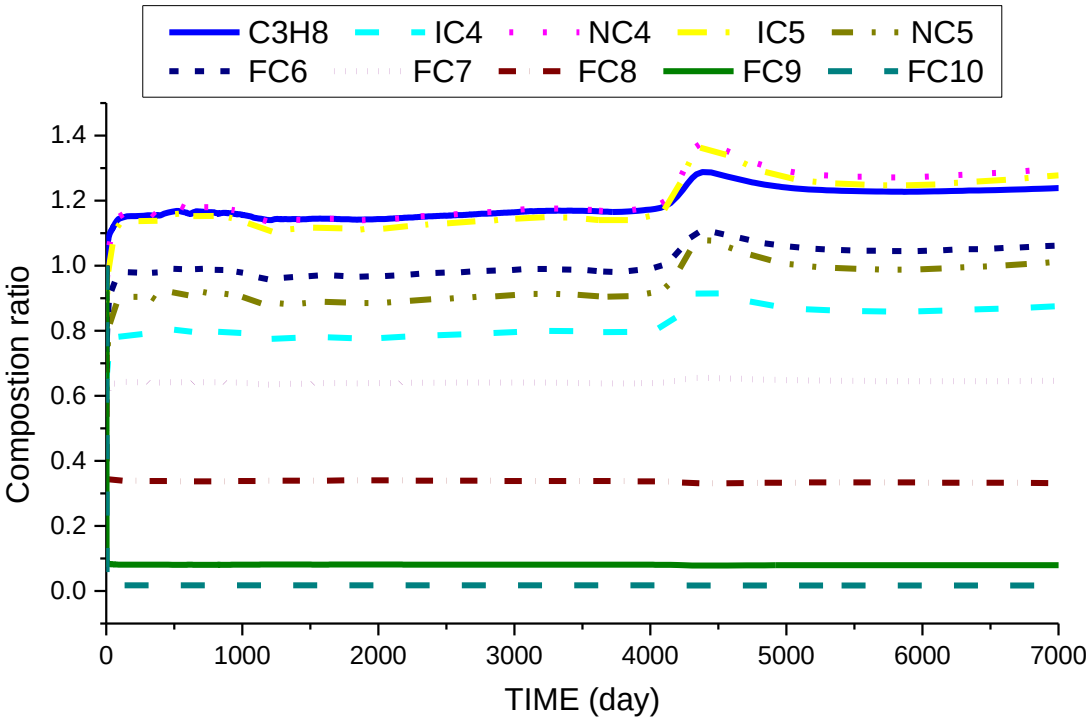

Figure 89. Produced gas composition ratio of C3 to FC10 (Equivalent to Figure 53)

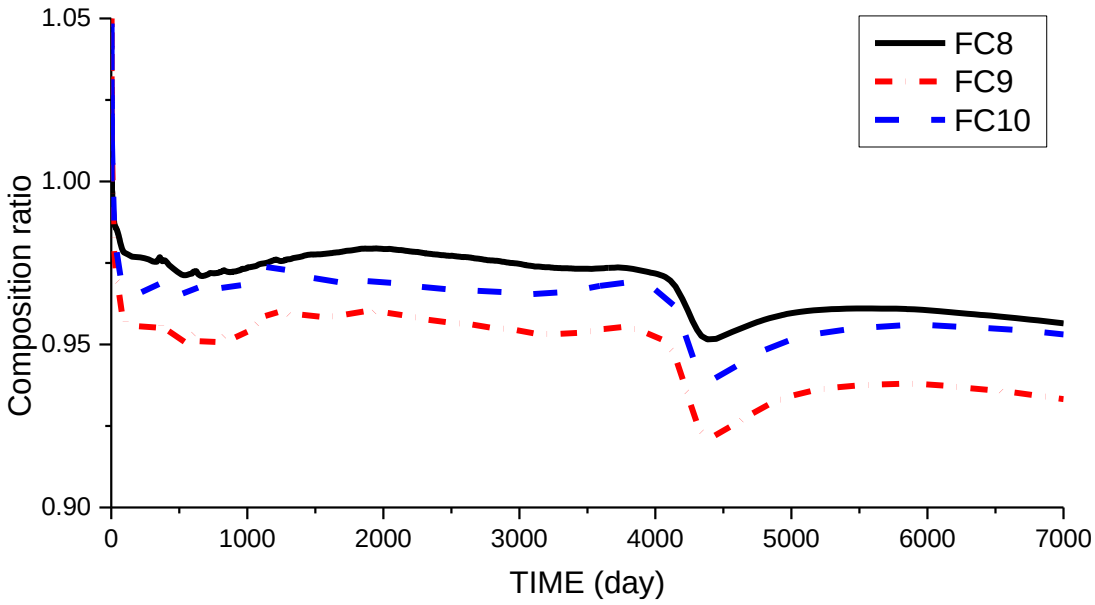

Figure 90. Produced oil composition ratio of FC8, FC9 and FC10 (Equivalent to Figure 54)

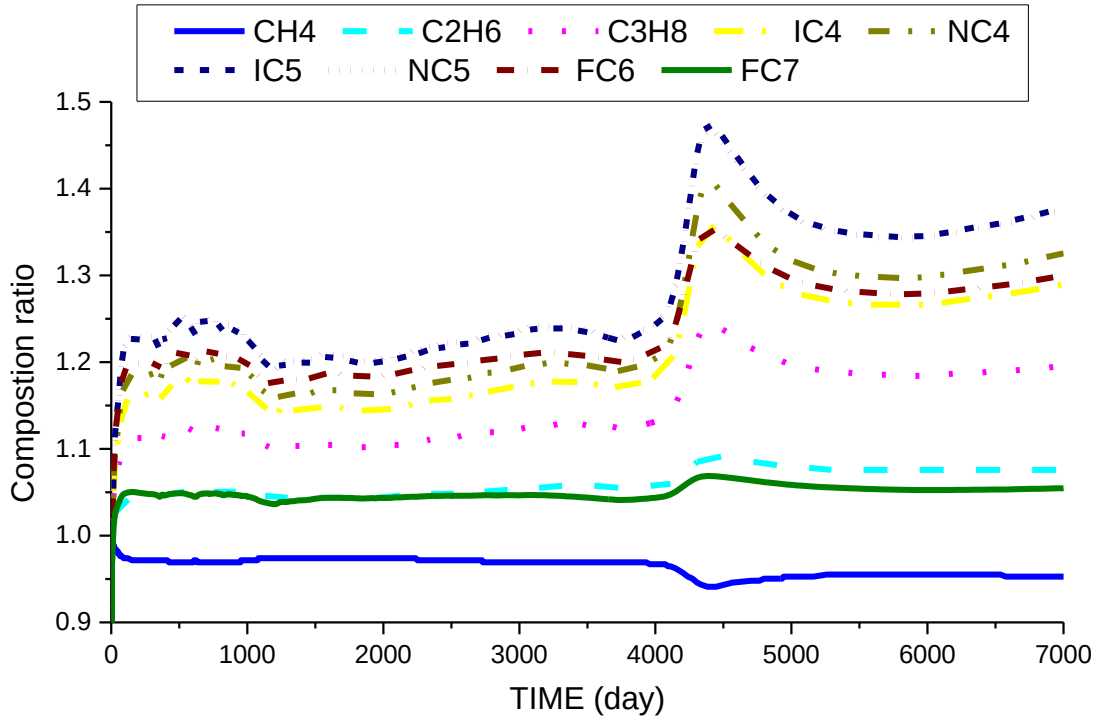

Figure 91. Produced oil composition ratio of C1 to FC7 (Equivalent to Figure 55)

Appendix C. Volatile Oil Case Study

The discussion in the thesis is centered around gas condensate reservoirs. In this appendix, I demonstrate the influence of Knudsen diffusion on volatile oil reservoirs.

1. Fluid Composition used for Volatile Oil Case

Table 18 shows the fluid composition used for this volatile oil case study and Figure 92 is the corresponding phase diagram.

Table 18. Volatile oil composition (4 components)

C1	FC6	FC7	FC8
60%	15%	15%	10%

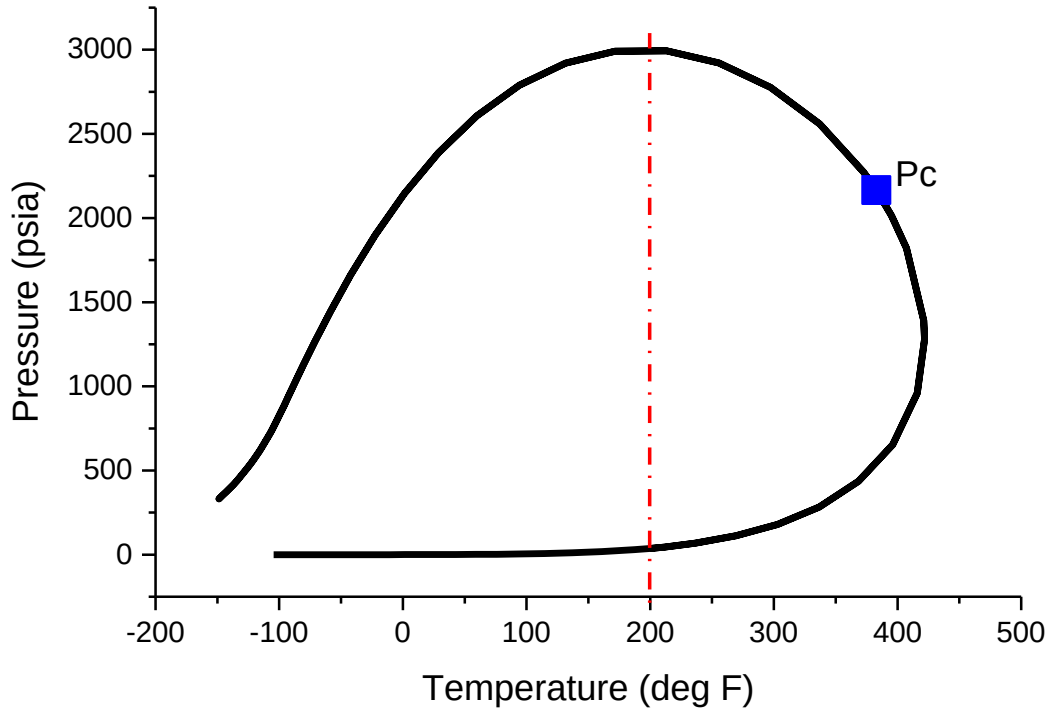

Figure 92. Volatile oil phase diagram.

2. Volatile Oil Case Study with Diffusion

Figure 93 to Figure 96 shows production trends of the volatile oil case study with diffusion in the oil and gas phase. The reader is referred to Chapter 4 for an overview of the model. In this case study, the well is producing at a constant BHP of 1000 psia which is below the saturation pressure of the oil at reservoir temperature. Figure 93 shows the GOR, gas saturation in the hydraulic fracture and in the SRV. As with the gas-condensate fluid case of Chapter 4, 2-phase flow occurs in the fracture systems.

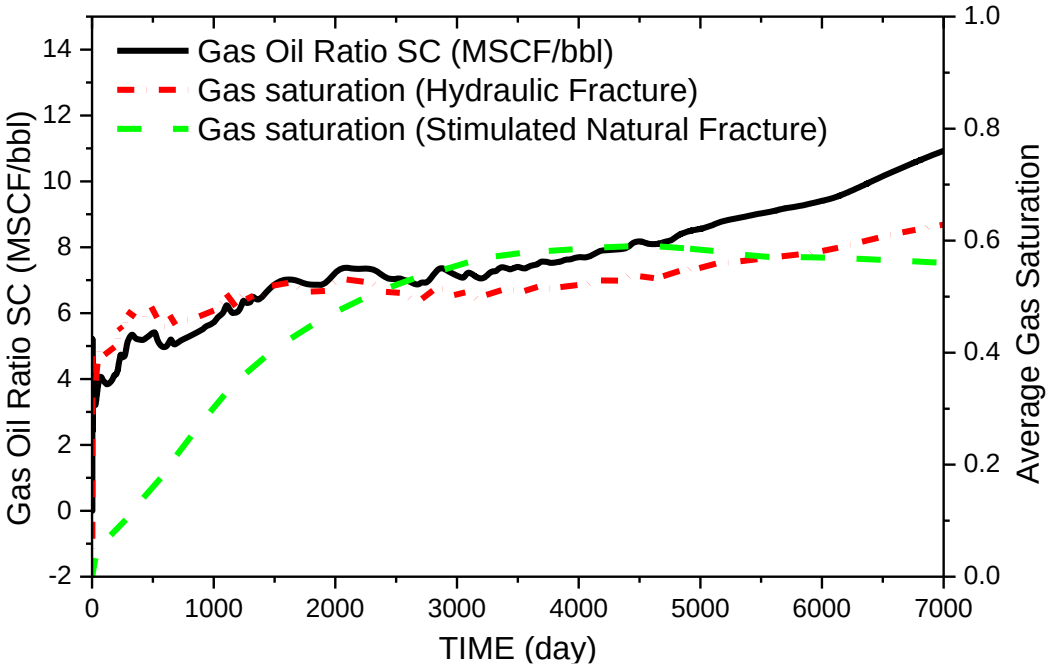

Figure 93. GOR and gas saturation with diffusion included.

Figure 94 shows the oil and gas production rates with time. Figure 95 and Figure 96 plots the produced fluid composition changes with time indicating the produced oil progressively becomes heavier while the produced gas becomes lighter as time goes by.

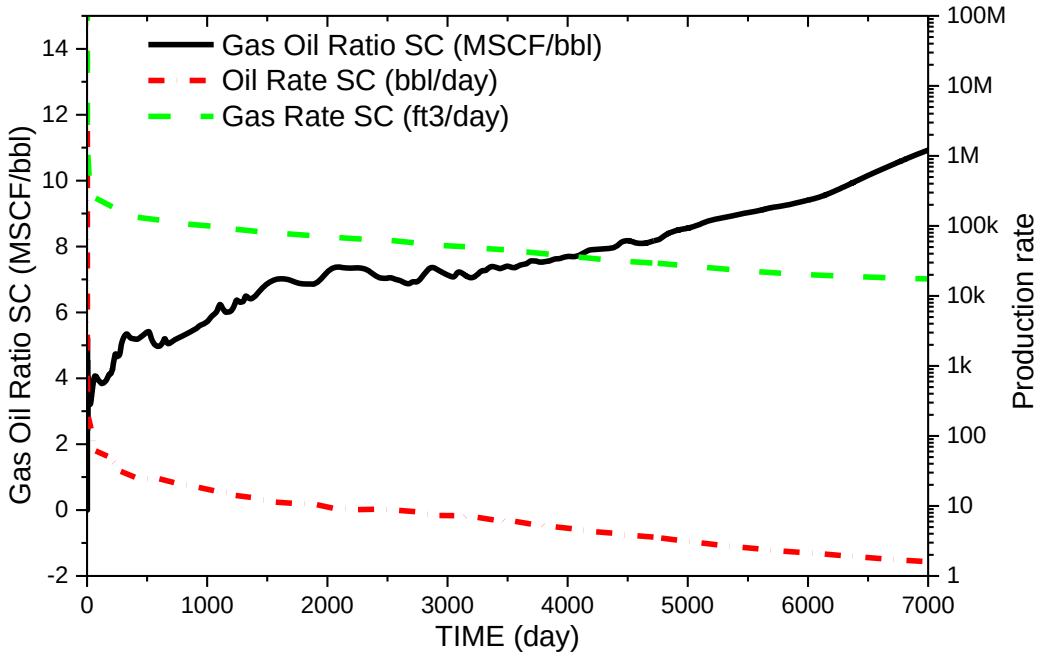

Figure 94. GOR, gas and oil production rate with diffusion included.

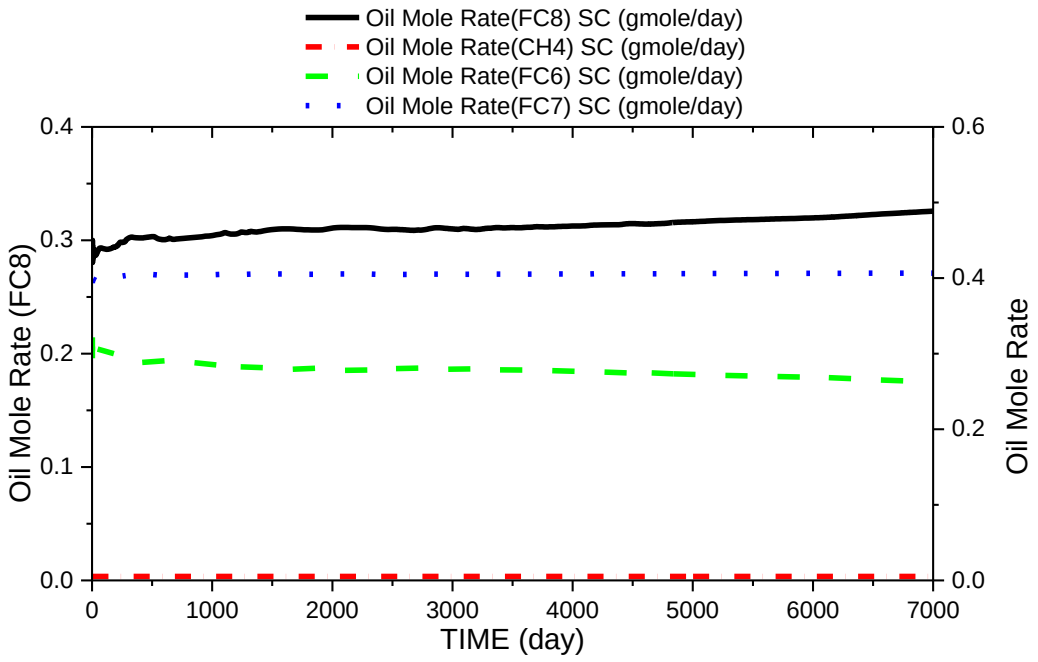

Figure 95. Produced oil composition change with diffusion included.

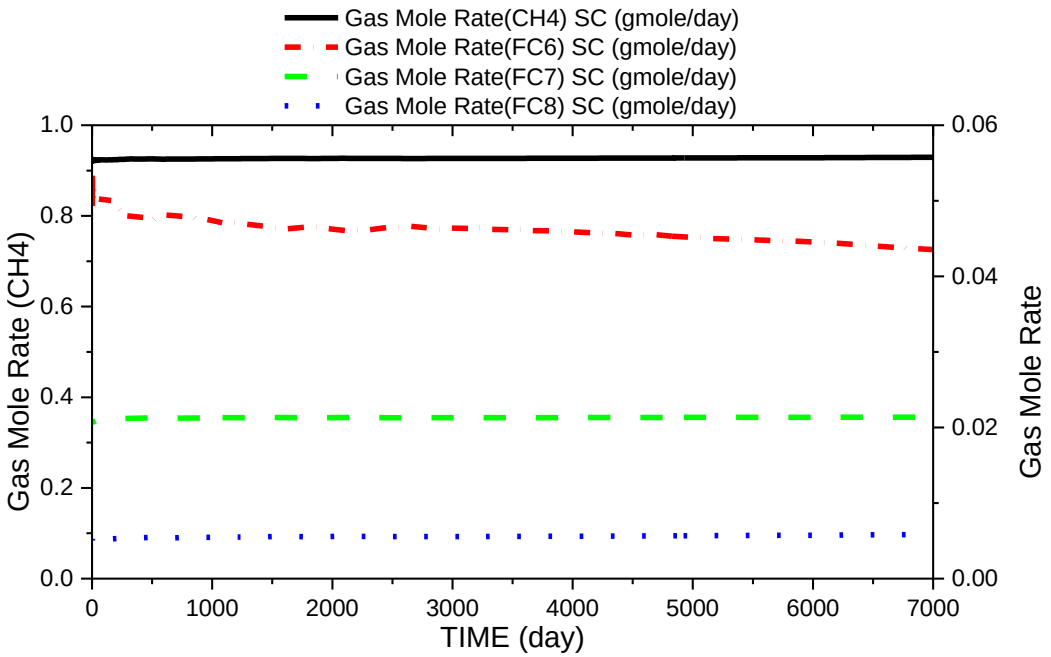

Figure 96. Produced gas composition change with diffusion included.

Comparison of Fluid Flow Trends with and without Diffusion

In this section, I show a comparison of production trends (Figure 97), gas saturation distribution (Figure 98 and Figure 99) and pressure distribution (Figure 100 and Figure 101) for two case studies: One with diffusion activated and one without. Activation of the diffusion allows the pressure communication and mass transport for both the fracture and matrix system. Due to the gas slippage effect, we observe a higher gas production rate, higher gas saturation in hydraulic fracture area and GOR values.

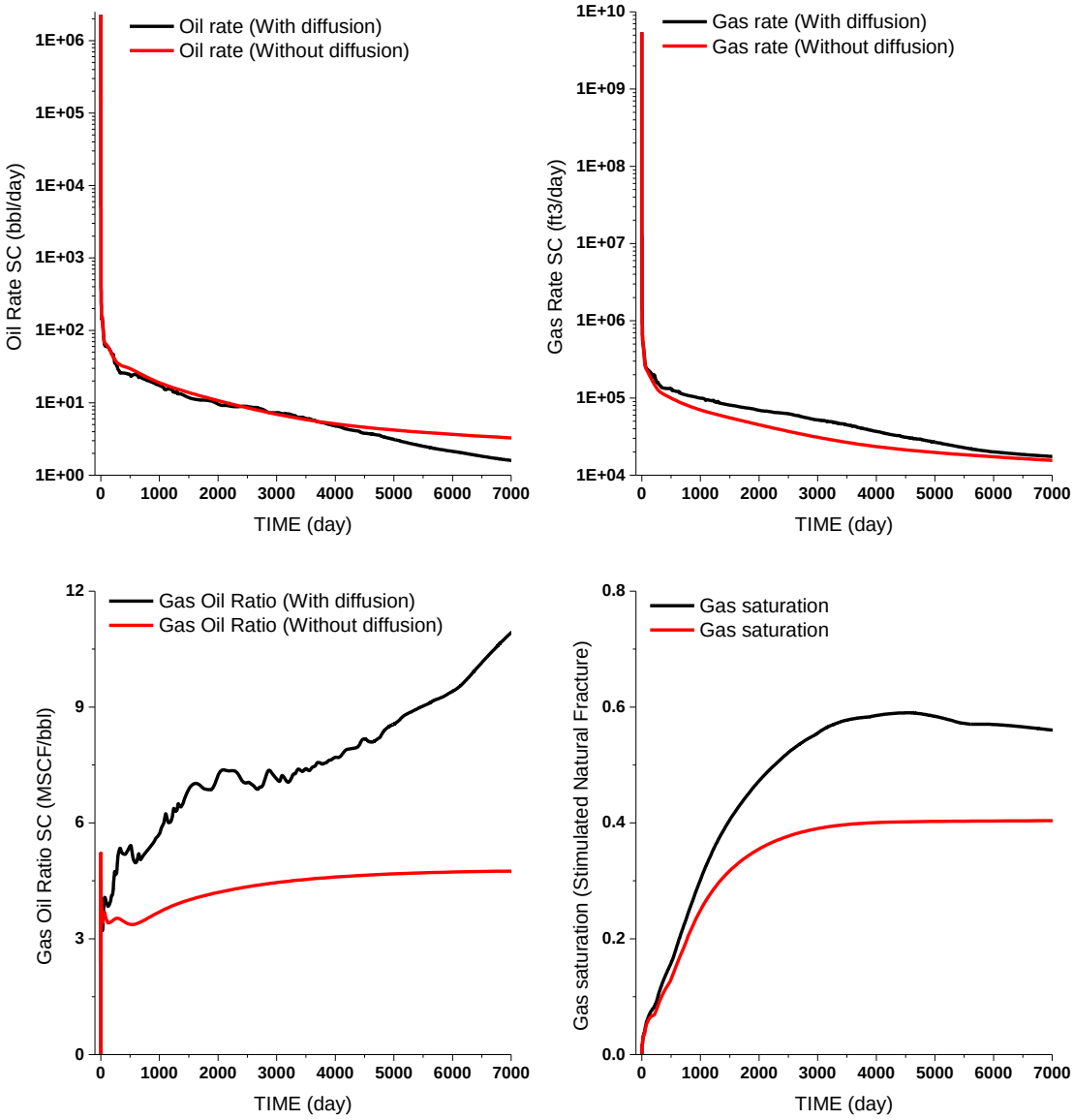

Figure 97. Comparison of production trends with and without diffusion.

Figure 98 shows the gas saturation in the matrix and fracture systems following 1 year and 20 years of production with the diffusion option activated. Figure 99 shows the corresponding plots when the diffusion option is not included. Both figures indicate that a free gas phase predominantly exists in the fractured SRV volume. The pressure transients shown in Figure 100 and 101 do not show any appreciable differences in the drainage areas; however there is a difference in the absolute pressures.

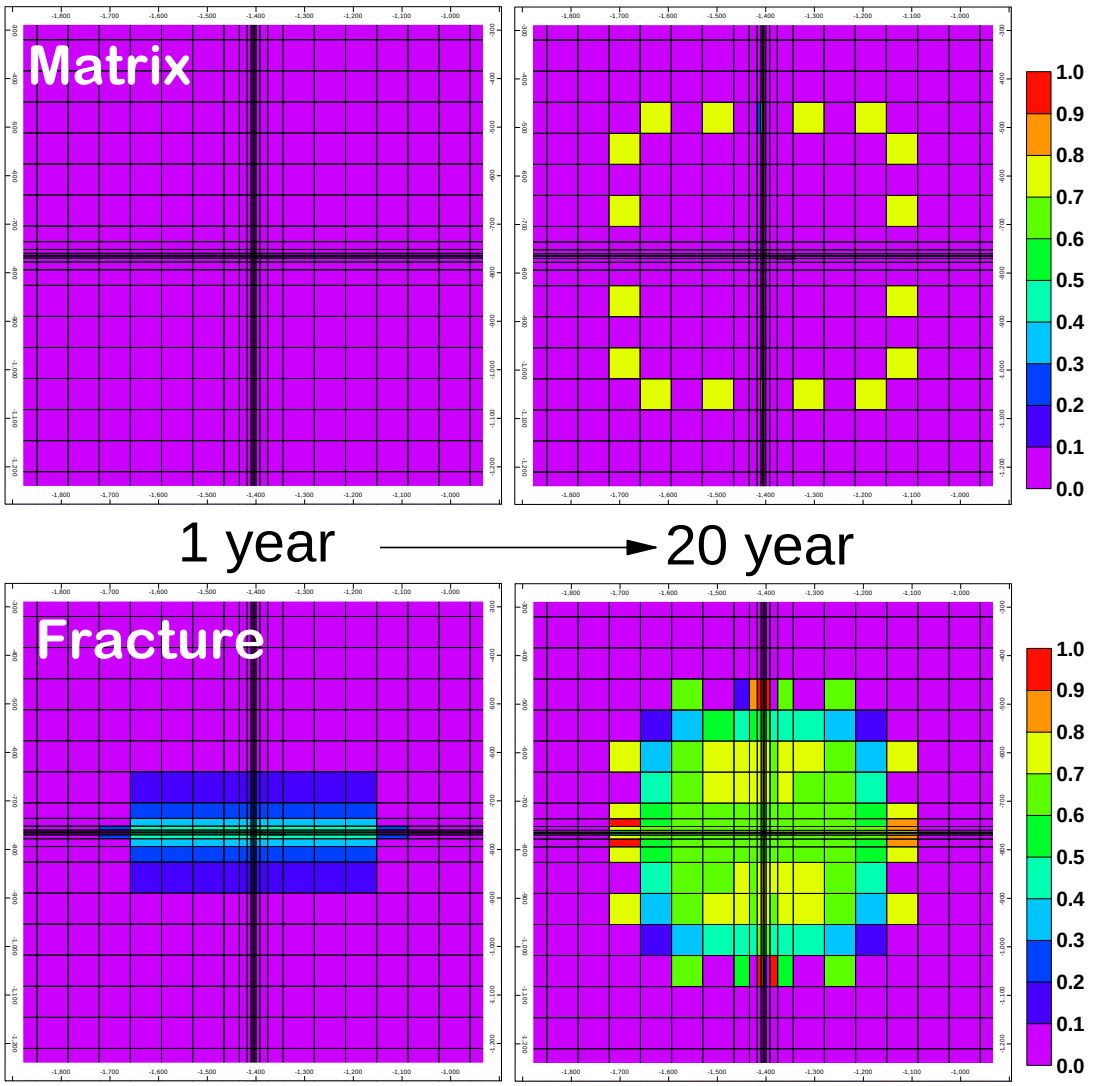

Figure 98. Gas saturation distribution with diffusion included.

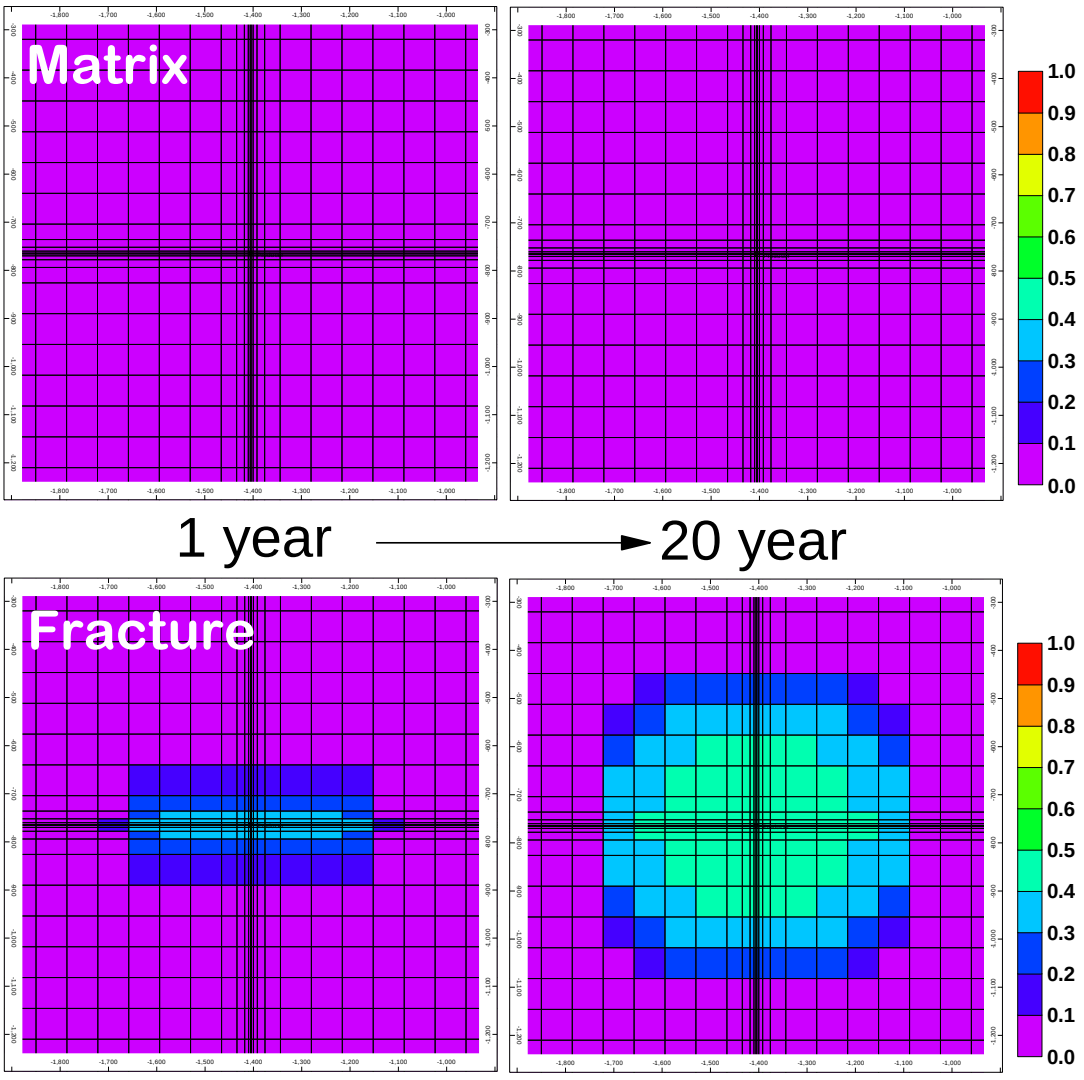

Figure 99. Gas saturation distribution with no diffusion included.

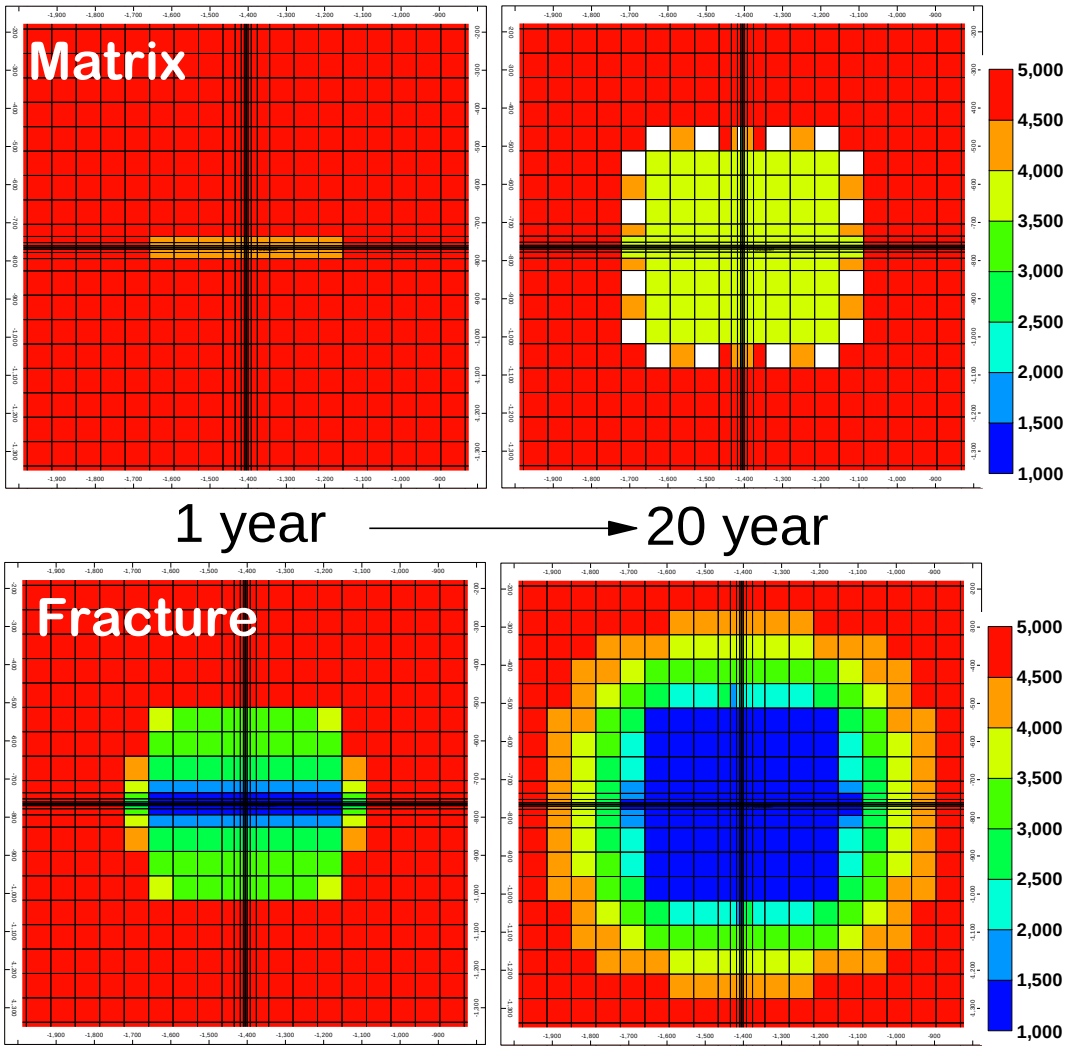

Figure 100. Pressure distribution with diffusion included.

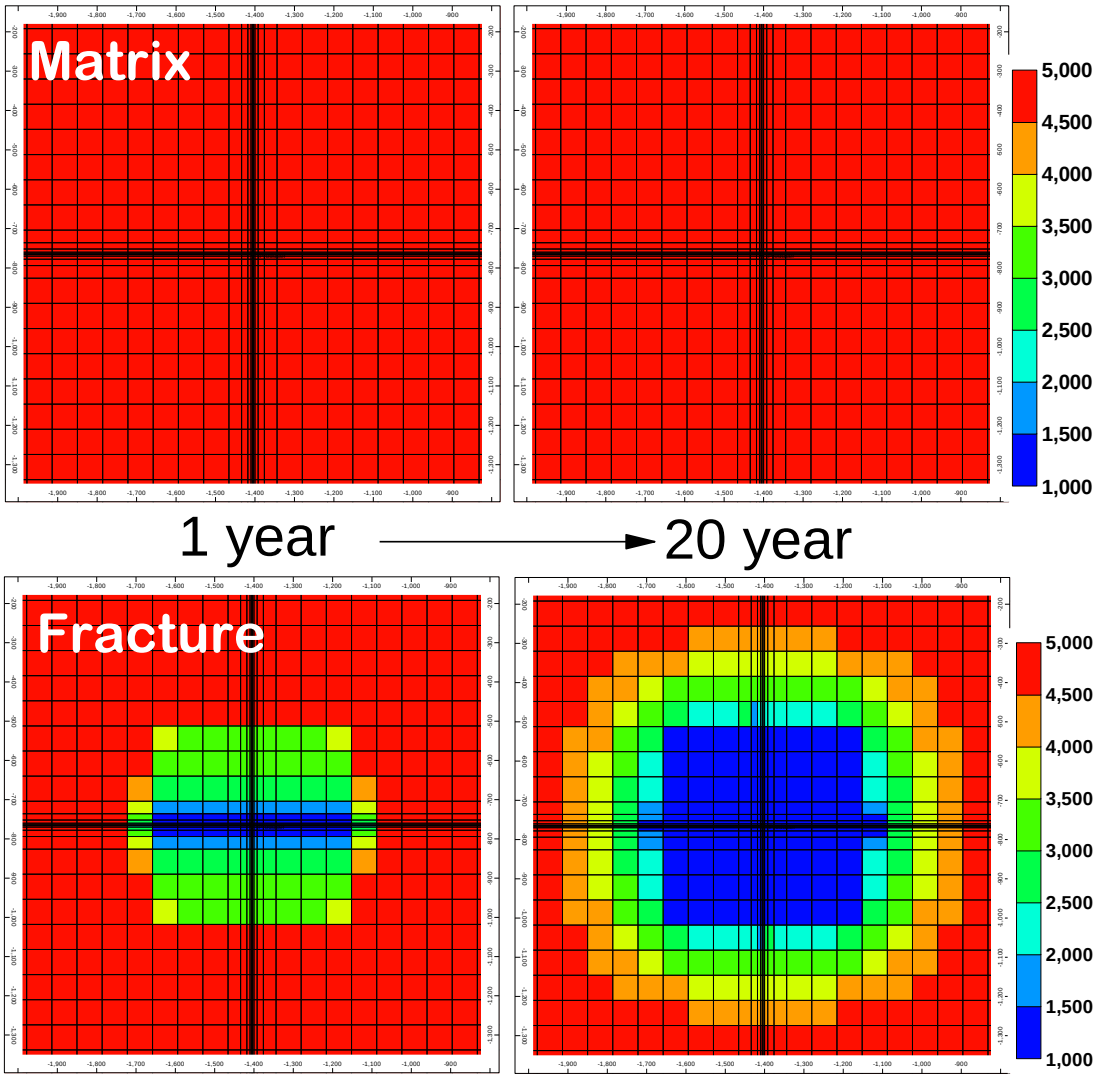

Figure 101. Pressure distribution with no diffusion included.